Single and Multiphase Simulations of Non-Newtonian Blood Flow

MSc Thesis

Delft University of Technology
Faculty of Applied Sciences
Department of Chemical Engineering
Section of Transport Phenomena

Author:
H.J. Doolaard

Supervisor:
Dr. ing. S. Kenjereš

Reviewers:
Prof. Dr. Ir. C.R. Kleijn
Dr. Ir. F.J. Gijsen
Ir. B.W. Righolt

February 1, 2013

Abstract

This study contributes to the development of a CFD (Computational Fluid Dynamics) model of blood flow through the human vascular system. The first objective is to extend the set of steady state simulations of single-phase Newtonian blood flow through a real patient's Carotid Artery, which contains a bifurcation, using several meshing methods. The Wall Shear Stress (WSS) profiles are compared for meshes consisting of hexahedral, tetrahedral or polyhedral cells where all meshes contain just one cell-type. Meshes with and without a boundary layer are created for those three cell types. The polyhedral mesh with boundary layer is found to outperform the other meshes on computational time. The meshing procedure could be automated which is a great advantage since each patient has a unique artery. The hexahedral grids result in the smallest discretization error but the highly user-intensive meshing method rejects this cell type for medical usage.

A more realistic model of blood is obtained by implementing a non-Newtonian Carreau-Yasuda viscosity model (Bird et al., 1987) with the model parameters proposed by Jung et al. (2006). This model prescribes an increasing viscosity for a decreasing strain rate. It is also applied to a two-phase model of Red Blood Cells (RBCs), which cause the non-Newtonian behaviour, suspended in Newtonian plasma, where the viscosity increases for increasing RBC volume fraction.

The two non-Newtonian models are tested in two simplified arterial geometries starting with a transient flow through a 180 ° bended tube. This geometry is based on the right coronary artery and so is the pulsating inlet velocity. The Newtonian and non-Newtonian model induce a difference in WSS up to 30% in the high-velocity part of the cardiac cycle. Although the RBC volume fraction differs a few percentage points in the multiphase simulation from the fixed 45% in the single-phase flow, there is only minor difference observed between both non-Newtonian models.

The second geometry that is used to examine the influence of the Carreau-Yasuda viscosity model is a straight tube suddenly expanding from 150 μm diameter to 504 μm. The steady state flow results are compared beneficially to experiments (Karino and Goldsmith, 1977) and CFD computations (Jung and Hassanein, 2008) for Reynolds numbers between 4.1 and 41.2. The WSS and the flow properties in the recirculation zones right after the expansion are different for all three flow models. The centres of the vortices contain less RBCs in the multiphase flows which leads to a significantly smaller viscosity in the vortex. The increased computational effort of the multiphase approach provides more accurate information on the blood composition in a recirculation zone.

Finally these models are applied in CFD simulations of steady state flows through a healthy Carotid Artery (Re = 195 and Re = 98) and a diseased Carotid Artery (Re = 120). These Re are large in comparison to the suddenly expanding tube. The absence of recirculation zones and large curvatures explain the minor differences in flow parameters like the velocity profile and the WSS between the three models. Recirculation is actually observed in a previous study (Righolt, 2010) with a transient flow through the same diseased artery. It is concluded that the Newtonian model is sufficiently accurate for the main arteries when a steady state solution provides sufficient information. If the effect of the heart-pulse has to be taken into account it is recommended to use the non-Newtonian single-phase model.

Samenvatting

Dit onderzoek draagt bij aan de ontwikkeling van een CFD model (Computational Fluid Dynamics, Numerieke Stromingsleer) van de menselijke bloedsomloop. In het eerste deel zijn stationaire simulaties gedaan van de bloedstroming waarbij het bloed gemodelleerd is als één Newtonse vloeistof. Het doel van dit deel is om de set van simulaties van de bloedstroom in de halsslagader van een echte patiënt, die is gediscretiseerd op verscheidene manieren, uit te breiden. De resultaten zijn vergeleken door profielen van de schuifspanning te vergelijken voor verschillende roosters die enkel zesvlakken, piramides of veelvlakken bevatten. Er zijn roosters ontworpen met en zonder grenslaag, welke uit kleinere cellen van dezelfde soort bestaat. De simulaties met de roosters die bestaan uit veelvlakken en een grenslaag bevatten, hebben de kortste rekentijd. Het gegeven dat het genereren van een rooster geautomatiseerd kan worden voor de piramides en de veelvlakken is een groot voordeel omdat iedere patiënt een uniek bloedvatenstelsel heeft. De fout die is veroorzaakt door de discretisatie is het kleinst voor de zesvlakken, maar deze vorm wordt verworpen wegens het arbeidsintensieve proces om het rooster te maken.

Een realistischer model van bloed is verkregen door het niet-Newtonse Carreau-Yasuda viscositeitmodel toe te passen (Bird et al., 1987) met de parameters van Jung et al. (2006). Dit model beschrijft een toenemende viscositeit wanneer de reksnelheid (Engels: strain rate) afneemt. Hetzelfde model is toegepast in een tweefasemodel waarin niet-Newtonse rode bloedcellen (RBCs) opgelost zijn in Newtons bloedplasma. De viscositeit neemt toe wanneer de volumefractie van RBCs toeneemt.

De twee niet-Newtonse modellen zijn getest in twee vereenvoudigde geometriën. De eerste is een 180° gebogen buis die gebaseerd is op de kransslagader, waarop het profiel van de inlaatsnelheid ook aan is gepast. De Newtonse en niet-Newtonse modellen leiden tot een verschil in schuifspanning van maximaal 30% in het deel van de hartcyclus met hoge stroomsnelheid. De volumefractie van RBCs in de tweefasestroming verschilt een paar procentpunt ten opzichte van 0.45 in de eenfasestroming. Ondanks dit verschil is het onderscheid tussen de resultaten van beide niet-Newtonse modellen te verwaarlozen.

De tweede vereenvoudigde geometrie waarin de invloed van het Carreau-Yasuda model is getest is een rechte buis waarvan de diameter abrupt toeneemt van 150 μm naar 504 μm. De resultaten van de stationaire stroming zijn met goed gevolg vergeleken met experimenten (Karino and Goldsmith, 1977) en andere CFD simulaties (Jung and Hassanein, 2008) voor Reynolds getallen tussen de 4.1 en de 42.1. De schuifspanning aan de wand en de stromingspatronen in de werveling net na de verwijding verschillen voor alle drie de modellen. In het tweefasemodel is de concentratie RBCs in de werveling lager, wat een substantieel kleinere viscositeit veroorzaakt. De hogere rekenkosten die nodig zijn voor de tweefasestroming verschaffen nauwkeurigere informatie over de samenstelling van het bloed in een werveling.

De drie modellen zijn ten slotte toegepast in CFD simulaties van stationaire stromingen door een gezonde (Re = 195 and Re = 98) en een zwaar aangetaste (Re = 120) halsslagader. Dit zijn hoge Re vergeleken met die van de stroom door de buis met abrupt toenemende diameter. De afwezigheid van wervelingen en grote krommingen verklaart de minieme verschillen tussen de drie modellen in ondermeer de snelheidsprofielen en de schuifspanning aan de wand. Er zijn echter wervelingen waargenomen in een eerder onderzoek (Righolt, 2010) naar een tijdsafhankelijke stroming door dezelfde aangetaste halsslagader. Uit de analyses van het de simulaties van bloedstroming door een gezonde en aangetaste halsslagader blijkt dat een Newtons model nauwkeurig genoeg is voor bloedstromen in hoofdaders wanneer de resultaten van een stationaire stroming voldoende informatie bieden. Het niet-Newtonse eenfasemodel wordt geadviseerd wanneer het effect van de hartslag van belang is.

Contents

CHAPTER 1

Introduction

A healthy circulatory system is essential for living. However, there is a high incidence of vascular disease in the Western world. It would be wonderful if one could reduce the number of deaths due to vascular diseases by locating the weak points in an artery and predicting the development of diseases like atherosclerosis. The development of a computer model that provides accurate predictions of the blood flow at reasonable expenses is the aim of the coordinating project. Another application of such a computer model could be the prediction of the trajectories of medicines to optimize drug targeting.

An accurate model of the blood flow through the vascular system starts with a good discretization of the geometry, also known as a good mesh or grid. Liu et al. (2004) compared the influence of a structured hexahedral mesh and an unstructured tetrahedral mesh on the velocity flow field, labour intensiveness of the meshing procedure and computational time. It is advised to use structured meshes for laminar flows with a clear flow direction while unstructured meshes give more accurate results for turbulent flows. The structured mesh resolves more vortices in the laminar flow through a crossing of four arteries.

The influence of the mesh on the velocity field and the particle deposition in a bifurcating airway is examined by Longest and Vinchurkar (2007). In addition to the meshes examined by Liu et al. (2004) they tested flow adaptive tetrahedral grids and a hybrid grid that consists of a boundary layer of five-sided pyramids surrounding a tetrahedral inner mesh. The hexahedral grid outperforms the other ones in computational time and in resemblance to the particle deposition observed in experimental results. The regularity of this mesh and the alignment with the predominant flow direction probably cause the fast convergence and the good results. The standard and flow adaptive tetrahedral meshes contain much more cells and more time is required to obtain a reasonably accurate solution. Although the accuracy is improved by using an adaptive mesh it is too expensive to use in transient simulations due to the large computational time. The hybrid grid leads to the least accurate results due to the sudden transition from the boundary layer to the inner grid. Its performance could be improved by a smoother transition from the boundary layer to the inner mesh and a prevention of element transition in regions with large gradients. Despite the differences just mentioned, all grid types show reasonable agreements with the experimental results.

The use of boundary layers and polyhedral cells is discussed in Spiegel et al. (2011). The results from tetrahedral and polyhedral meshes are compared to hybrid meshes that consist of a tetrahedral or polyhedral core enclosed by a hexahedral boundary layer. All meshes are of the same quality regarding the aspect ratio and the skewness for both the mesh and the surface. The Wall Shear Stress (WSS) is accurately resolved in the least computational time with the smallest amount control volumes in case of polyhedral meshes. Slightly more details are resolved with boundary layers, but its design requires more user interaction so polyhedral meshes without a boundary layer are advised for clinical purpose.

To quantify the influence of spatial discretization an estimation of the numerical uncertainty caused by the mesh is required. Roache (1994) proposed the Grid Convergence Index (GCI) for uniform reporting on grid quality. Solutions on at least three refined meshes per mesh type are required to compute the discretization error. As long as the same refinement factor is applied in each direction, it does not have to be refined with exactly a factor two as is required for Richardson extrapolation. It is advised from experience to apply a refinement factor of at least 1.3. The order of the computational method is also taken into account in the GCI calculation and it is computed on the basis of a local variable like the velocity or WSS. However, the computed order of the officially second

order computational schemes often deviates with a factor five or even becomes negative. The computation of the uncertainty is coupled to the resemblance of the apparent order to the formal order by Eça and Hoekstra (2009) and Zou et al. (2010) and an extrapolation method is proposed to obtain a solution with a higher order of accuracy.

When the optimal mesh is chosen one can focus on mimicking the blood rheology. A crude approximation of the blood rheology is a Newtonian fluid, which is used in the mesh accuracy analysis. The first improvement is to change the constant viscosity model into a shear-thinning model where the viscosity increases at low shear rate. Yilmaz and Gundogdu (2008) created an overview of viscosity models and commented on the agreement between these models and the biological properties of blood. The main components of blood are Newtonian plasma and Red Blood Cells (RBCs), which are held responsible for the shear-thinning effect. The major properties of RBCs that cause the shear thinning effect are that these can form aggregates, they align with the blood flow and they can change shape to allow entering the smallest blood vessels. Several authors like Ballyk et al. (1994), Johnston et al. (2004), Soulis et al. (2008), Gijsen et al. (1999) and Liu and Dalin (2011) tested viscosity models. The Carreau-Yasuda model and the General Power Law (GPL) are among the favourites. The composition of blood and its properties are discussed in more depth in Chapter 2.

Most non-Newtonian viscosity models that are designed for blood simulations depend on the shear rate which varies strongly during the cardiac cycle. Therefore the next step in mimicking the blood rheology is to go from steady state to transient simulations with a heart-pulse as inlet boundary condition. Since each artery is part of the closed circulatory system at least one cycle is discarded to be sure that the results of a fully developed flow are examined.

In order to account for the actual composition of blood it is treated as a suspension instead of a single fluid. The simplest multiphase approach is to treat blood as non-Newtonian RBCs dispersed in Newtonian plasma. A two-phase blood model is introduced by Jung et al. (2006) in which the viscosity depends on the RBC volume fraction (also known as hematocrit) and the shear rate. Four viscosity models are examined by Kim et al. (2008)in the same computational setup as Jung et al. (2006) using a different heart pulse as inlet boundary condition. Two viscosity models depend on the hematocrit and the strain rate, while the others solely depend on the strain rate. The hematocrit dependence is found to be essential to describe the blood rheology.

1.1 Present research

The current developments in CFD modelling of blood flow through a human artery described above lead to the formulation of two major objectives. First of all several numerical mesh topologies are examined to select the most appropriate one for medical usage. These topologies are compared on the effort that is expended on obtaining a suitable mesh, the computational time that is required to get a fully convergent solution and the discretization error.

Secondly the significance of taking into account the non-Newtonian properties of blood is investigated. The shear-thinning Carreau-Yasuda viscosity model is therefore implemented in a single-phase and a multiphase blood model. The flow patterns, WSS and viscosity are parameters of interest which are compared for these models and the single-phase Newtonian model in several geometries for various flow velocities.

This report starts with more on the biological background and viscosity models in Chapter 2, followed by a brief overview of fluid dynamics for laminar single-phase and multiphase flows in Chapter 3. This theory is translated into computational models in Chapter 4, which also expounds on the intricacies of calculating the discretization uncertainty due to the mesh. The results for the three flow models in simplified geometries are presented in Chapter 5 for a 180 ° bended tube and Chaper 6 for a tube with a suddenly increasing diameter. Then the process of obtaining the geometry of a healthy carotid artery, the meshing procedure and a mesh quality analysis are discussed in Chapter 7 followed by the results of the Newtonian flow and the discretization uncertainty in that carotid artery in Chapter 8. The influence of non-Newtonian viscosity models in this artery is examined in Chapter 9 and the

research is concluded with the flow through a severely diseased artery in Chapter 10. Finally the conclusions and recommendations are offered in Chapters 11 and 12 respectively.

CHAPTER 2

Biological background

Computational models of the blood flow through a bifurcation in a human carotid artery are examined. This bifurcation is located in the human neck where the common carotid artery (CCA) splits into the internal carotid artery (ICA) and the external carotid artery (ECA), as can be seen in the centre of Figure 2.1. The ICA is the main artery for the blood supply for the brains and the ECA provides the face and the neck with blood. Humans have a carotid artery at each side of the neck and the left carotid artery is taken for this research. Next to the geometry the properties of the complex suspension that is called blood and the models that are developed to imitate its behaviour are examined in more depth.

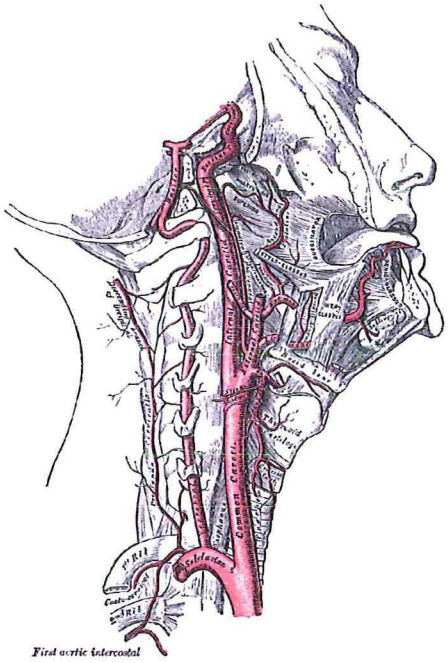

Figure 2.1: An illustration of the arteries in the neck (Gray (1918)).

2.1 Hemorheology

The study of blood flow properties is called hemorheology, which is a compound of hemo: blood; and rheology: the study of the flow properties of a non-Newtonian fluid or fluidized flow of solids. About 55 vol% of human blood is Newtonian fluid plasma existing for over 90% of water. The particulate elements (see Figure 2.2) of the blood that are responsible for the non-Newtonian behaviour are Red Blood Cells (RBC, 45 vol%), leukocytes, also known as White Blood Cells (WBC, 1 vol%), AND platelets and fibrinogen (each < 1 vol%) which are both involved in blood clotting. The volume fraction of the RBCs is also known as the Hematocrit, which is 0.47 ± 0.07

for adult men and 0.42 ± 0.05 for adult women (Yilmaz and Gundogdu, 2008). The main non-Newtonian properties of blood are thixotropy (shear thinning) and viscoelasticity (Yilmaz and Gundogdu, 2008) .

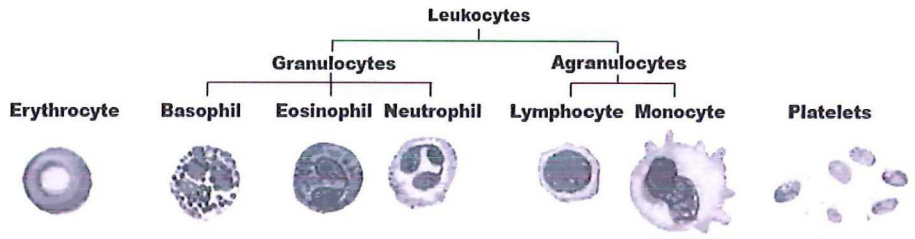

Figure 2.2: RBCs and some examples of WBCs (Yilmaz and Gundogdu, 2008)

An RBC consists of a Newtonian hemoglobin solution bounded by a thin elastic membrane. This allows RBCs to deform in order to pass through capillaries and it allows for aggregation at low shear rate. This aggregating is the main reason for the thixotropic behaviour. At a very low shear rate the RBCs become one big aggregate which makes the blood solidify. This aggregate falls apart into clusters of RBCs called rouleaux when the shear rate increases. Above a certain shear rate of about 50 s^{-1} all rouleaux have fallen apart and the single RBCs tend to align with the flow. This is why blood could be modelled as a Newtonian fluid in the shear rate regime above this threshold.

The second element of the non-Newtonian behaviour of blood can be described by a viscoelasticity model. Viscoelasticity is a compound of viscosity and elasticity and blood is indeed observed to possess both viscous and elastic properties. The concept of viscosity results in energy dissipation, which is caused by cell deformation and sliding. The elasticity expresses elastic storage of energy, mainly due to kinetic deformability in the RBC aggregates that act like solids. Both effects are just significant at very low shear rates (below $1s^{-1}$), so it is ignored in most models.

One may notice that the non-Newtonian properties are mainly caused by the RBCs, so it would be logical that the viscosity model is a function of the hematocrit (RBC volume fraction). This implies that a multiphase model should be used to imitate the blood behaviour. So the distribution of the RBCs due to particle-particle interaction, particle-fluid interaction, and external forces could be calculated and the resulting viscosity could be determined.

Apart from the blood composition, one has to be aware of the complexity of the flow environment, for example the pulsatile flow, the enormous length of the complete circulatory system with all kinds of damping or resonance effects and the complexity and elasticity of the blood vessels. It is necessary to simplify these conditions to be able to create a model. However, the assumptions have to be mentioned and argued when setting up the model and they should be kept in mind the results are discussed.

2.2 Viscosity models

The properties of an appropriate non-Newtonian viscosity model for modelling human blood are discussed in the former section, but what is viscosity and what does a viscosity model look like?

Viscosity is the "constant" of proportionality between the shear stress (τ) and the shear rate ($\dot{\gamma}$ in equation 2.1). The viscosity is a constant in the simplest model. This Newtonian model is described by:

$$\tau = \mu\dot{\gamma} \tag{2.1}$$

where τ is the shear stress, μ is the viscosity, and $\dot{\gamma}$ is the shear rate magnitude defined as

$$\dot{\gamma} = \sqrt{S_{ij}S_{ji}}, \tag{2.2}$$

with S_{ij} the shear rate tensor, which is given by

$$S_{ij} = \frac{1}{2}\left(\frac{\partial u_i}{\partial x_j} + \frac{\partial u_j}{\partial x_i}\right) \tag{2.3}$$

Next to the constant viscosity three viscosity models that describe the behaviour of blood more accurately will be discussed. . These models are the Generalized Power Law (GPL), the Quemada model and the Carreau-Yasuda model. For large *Re* all velocity profiles collapse to the profile obtained with constant viscosity. However, for flows with low *Re* the maximum velocity is reduced due to the non-Newtonian properties.

2.2.1 Generalized Power Law

The Generalized Power Law is based on the Power Law (equation 2.4) that is designed to describe shear-thinning or shear-thickening behaviour of non-Newtonian fluids. Combining this equation with 2.1 leads to an expression for the apparent viscosity for the GPL model (equation 2.5).

$$\tau = \lambda|\dot{\gamma}|^{n-1}\dot{\gamma}, \tag{2.4}$$

$$\mu(\dot{\gamma}) = \lambda|\dot{\gamma}|^{n-1} \tag{2.5}$$

The Power Law describes the shear-thinning or shear-thickening behaviour of a fluid for a fixed region of strain rates. This constraint of the fixed region of the strain rate is removed in the Generalized Power Law by allowing the time-"constant" λ and the power law index n to depend on the strain rate as follows:

$$\lambda(\dot{\gamma}) = \mu_\infty + \Delta\mu\, exp\left[-\left(1+\frac{|\dot{\gamma}|}{a}\right)e^{-\frac{b}{|\dot{\gamma}|}}\right], \tag{2.6}$$

$$n(\dot{\gamma}) = n_\infty - \Delta n\, exp\left[-\left(1+\frac{|\dot{\gamma}|}{c}\right)e^{-\frac{d}{|\dot{\gamma}|}}\right], \tag{2.7}$$

The numerical values of the parameters were gathered from experimental data obtained from various sources by Ballyk et al. (1994): $\mu_\infty = 0.0035$ Pa· s, $\Delta\mu$ =0.025 Pa · s, $n_\infty = 1$, $\Delta n = 0.45$, $a = 50\text{s}^{-1}$, $b = 3\ \text{s}^{-1}$, $c = 50\ \text{s}^{-1}$, $d = 4\ \text{s}^{-1}$. The GPL encompasses the Power Law at low strain rates and the Newtonian model at high strain rates. The velocity profiles obtained with the GPL model and the Newtonian model match when $\mu_\infty(GPL) = \mu$(Newton).

2.2.2 Carreau-Yasuda model

The second non-Newtonian viscosity model is a function of the strain rate and the hematocrit (volume fraction of RBCs, ε_{RBC}). The Carreau model is originally designed to describe pseudo-plastics that consist of polymers. The Carreau-Yasuda is a modification of the Carreau model and its parameters for blood modelling are determined by Bird et al. (1987) by fitting the model with experimental data from Wojnarowski (2001) for $\varepsilon_{RBC} = 0.45$.

$$\mu = \mu_0 m\left(1+(\lambda\dot{\gamma})^2\right)^{\frac{n-1}{2}} \tag{2.8}$$

$$n = 0.8092\varepsilon_{RBC}^3 - 0.8246\varepsilon_{RBC}^2 - 0.3503\varepsilon_{RBC} + 1 \tag{2.9}$$

$$m = 122.28\varepsilon_{RBC}^3 - 51.213\varepsilon_{RBC}^2 + 16.305\varepsilon_{RBC} + 1 \tag{2.10}$$

n and m are fitting parameters, μ_0 is the viscosity of the blood plasma which is 0.001 kg/m ·s and the time constant $\lambda = 0.110$ s. The influence of the hematocrit is visualised in Figure 2.3a where the Carreau-Yasuda viscosity is plotted as a function of the strain rate for several values of the hematocrit. The minimum and maximum hematocrit for human beings is 0.35 and 0.55 respectively. The ratio of the viscosities with these hematocrits is 2.6 for small strain rates and 1.1 for large strain rates (about $10^4\ \text{s}^{-1}$). This indicates that a fluctuation in hematocrit level has a large impact on the viscosity, which affects the flow pattern and the wall shear stress (WSS) pattern too.

2.2.3 Quemada model

The last viscosity model that will be discussed is the Quemada model. Quemada (1978*a*) based his viscosity model on the concentrated dispersion of particles (red and white blood cells and blood platelets) in a fluid (plasma). The viscosity for a two-phase model with plasma and RBCs is a function of the hematocrit and the strain rate:

$$\mu(\dot{\gamma}) = \mu_F \left(1 - \frac{k_0 + k_\infty \dot{\gamma}_r^{1/2}}{1 + \dot{\gamma}_r^{1/2}} \frac{\varepsilon_{RBC}}{2}\right)^{-2}, \tag{2.11}$$

where μ_F is the viscosity of the suspending fluid, which is $1.2 \times 10^{-3} Pa \cdot s$ for blood plasma. k_0 and k_∞ are the intrinsic viscosities at low and high strain rate respectively. $\dot{\gamma}_r = \dot{\gamma}/\dot{\gamma}_c$ is the reduced strain rate, with $\dot{\gamma}_c$ a critical strain rate that is based on the relaxation time of very dilute suspensions with rigid spheres. The model parameters for blood are $k_0 = 4.33$, $k_\infty = 2.07$ and $\dot{\gamma}_c = 1.88\ s^{-1}$ for $\varepsilon_{RBC} = 0.45$ (Quemada, 1978*b*).

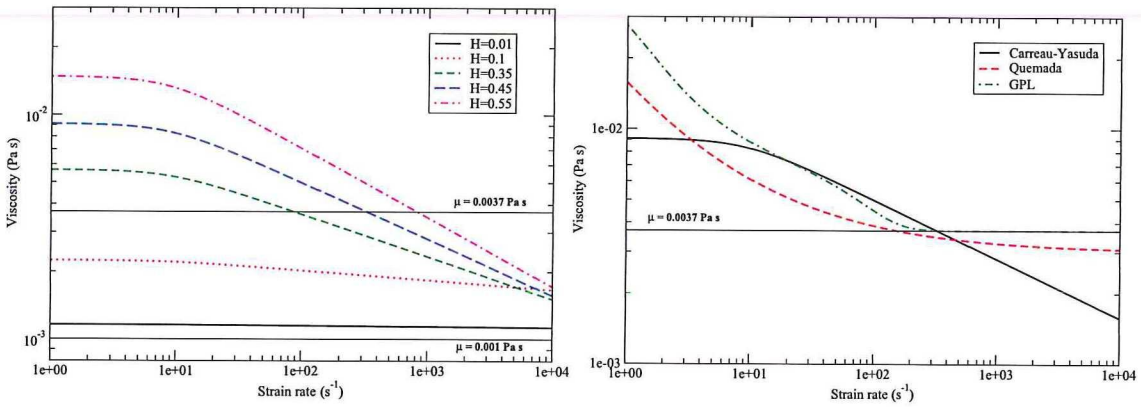

(a) Carreau-Yasuda

(b) Constant hematocrit of 0.45

Figure 2.3: Figure (a) displays the molecular viscosity according to the Carreau-Yasuda model, plotted as a function of the strain rate for several values of the hematocrit. The mean viscosity of human blood is 0.0037 Pa·s and this value is used in the Newtonian simulations. Figure (b) shows the viscosity for the three models for $\varepsilon_{RBC} = 0.45$

A plot of the three non-Newtonian viscosity models with the hematocrit fixed at 0.45 is shown in Figure 2.3b. The Carreau-Yasuda model has an asymptotic value for the viscosity when the strain rate approaches 0 s^{-1}. The GPL model and the Carreau-Yasuda model conform to each other for strain rates between 10 and 400 s^{-1}, while the Quemada model predicts a smaller viscosity. Since the GPL and the Carreau-Yasuda model parameters are fit for this strain rate range, their viscosities are expected to be reliable. The GPL and Quemada models are approaching the mean blood viscosity for large strain rates as is observed for blood flows. Just like most non-Newtonian fluids, blood acts like a Newtonian fluid for large strain rates. So these two models are more appropriate for blood vessels where the blood flow has a large Reynolds Number.

CHAPTER 3

Single-phase and multiphase fluid dynamics

3.1 Basic fluid dynamics

Two principles are valid for all fluid and gas flows: the conservation of mass and the conservation of momentum. The general form of the conservation of mass is

$$\frac{\partial \rho}{\partial t} + \nabla \cdot (\rho \mathbf{u}) = 0 \tag{3.1}$$

ρ is the density, $\mathbf{u}$ is the velocity vector and ∇ is a vector that contains spatial derivatives, in 3D Cartesian coordinates represented by

$$[\frac{\partial}{\partial x}, \frac{\partial}{\partial y}, \frac{\partial}{\partial z}] \tag{3.2}$$

The conservation of mass for incompressible flows it is reduced to

$$\nabla \cdot \mathbf{u} = 0 \tag{3.3}$$

The momentum equations for fluids are also known as the Navier-Stokes equations and state for compressible flows

$$\frac{\partial(\rho \mathbf{u})}{\partial t} + (\rho \mathbf{u} \cdot \nabla)\,\mathbf{u} = -\nabla p + \nabla \cdot \left[\mu\left(\nabla \mathbf{u} + (\nabla \mathbf{u})^T - \frac{2}{3}\nabla \cdot \mathbf{u}\mathbf{I}\right)\right] + \mathbf{F} \tag{3.4}$$

p is the pressure in the above expression, μ is the dynamic viscosity, $\mathbf{I}$ is the unity matrix and $\mathbf{F}$ represents all body forces that act on the fluid. The Navier-Stokes equations are reduced for incompressible flows to

$$\rho\left(\frac{\partial \mathbf{u}}{\partial t} + (\mathbf{u} \cdot \nabla)\,\mathbf{u}\right) = -\nabla p + \nabla \cdot \mu(\nabla \mathbf{u}) + \mathbf{F} \tag{3.5}$$

The left hand side represents the momentum change in two terms: the local acceleration and the advection due to the flow field. The right hand side contains the causes of the momentum change: pressure gradient, viscous diffusion and body forces.
Another flow describing parameter is the dimensionless Reynolds number which is the ratio between the inertial forces and the viscous forces. Its definition is

$$Re = \frac{\rho u D}{\mu} \tag{3.6}$$

A flow is in the laminar regime for $Re < 2000$. D is a characteristic length for the geometry, for example the width of a channel or the diameter of a tube.
A quantity of interest is the Wall Shear Stress (WSS) which is the stress exerted on the artery by the blood. Extremes in WSS magnitude or rapid fluctuations could lead to the development of cardiovascular diseases.

$$\tau = \mu \frac{\partial u_{\parallel}}{\partial n} \tag{3.7}$$

with $u_{\parallel}$ the velocity component parallel to the wall and n the direction normal to the wall.

3.2 Multiphase flow

Most flows in real life are multiphase flows. Blood is also a multiphase flow with plasma as main fluid and red blood cells (RBCs), white blood cells, blood platelets and several proteins suspended in it. Since plasma contains millions of blood cells, it is computationally seen impossible with the current techniques to model all blood cells separately. One method to model RBCs in plasma is to use the granular theory, where the flow of a mixture of fluids is calculated while taking into account that one of the fluids actually consists of solid particles in the closure equations.

The granular theory can be applied in the Euler-Euler approach of multiphase flows. In that approach the different phases are treated as interpenetrating continua. Since a position in space can be occupied by exactly one phase, the volume fraction of each phase is introduced and the sum of the volume fractions equals one. The volume fraction is calculated by solving its continuity equation (Ansys, 2011*a*):

$$\left[\frac{\partial}{\partial t}(\varepsilon_k \rho_k) + \nabla \cdot (\varepsilon_k \rho_k \mathbf{u}_k)\right] = \left[S_k + \sum_{l=1}^{n} (\dot{m}_{lk} - \dot{m}_{kl})\right] \tag{3.8}$$

$$\sum_{k=1}^{n} \varepsilon_k = 1.0 \tag{3.9}$$

where n is the number of phases, k and l are phase indices, ε is the volume fraction, S is a source term and $\dot{m}$ is the mass transfer between two phases. The volume fraction is not solved for the primary phase (plasma), but it is calculated using the constraint from Equation 3.9.

The conservation equations for compressible fluids (Equation 3.1 and 3.4) are solved for each phase separately. In case of plasma and RBCs there is no mass source or mass exchange between the faces, so the continuity equation reduces to:

$$\frac{\partial \rho_k \varepsilon_k}{\partial t} + \nabla \cdot (\rho_k \varepsilon_k \mathbf{u}_k) = 0 \tag{3.10}$$

The conservation of momentum equations without mass transfer read as follows:

$$\frac{\partial \rho_k \varepsilon_k \mathbf{u}_k}{\partial t} + \nabla \cdot (\rho_k \varepsilon_k \mathbf{u}_k \mathbf{u}_k) = -\varepsilon_k \nabla p + \varepsilon_k \rho_k \mathbf{g} + \nabla \cdot \left[\varepsilon_k \left(\mu_k \left(\nabla \mathbf{u}_k + (\nabla \mathbf{u}_k)^T\right) - \left(\lambda_k - \frac{2}{3}\mu_k\right) \nabla \cdot \mathbf{u}_k \mathbf{I}\right)\right] + \mathbf{F}_k \tag{3.11}$$

The equations for compressible flows are solved because the mixture density and the density of plasma are fixed in a part of the simulations. The RBC density is then computed from the mixture density and the volume fractions. Since the RBC density is variable in space and time for these settings, the momentum equations for compressible flow have to be solved.

Comparing this equation to Equation 3.4 it is observed that the viscosity μ is replaced by the shear and the bulk viscosity, μ_k and λ_k. The shear viscosity equals the molecular viscosity of a non-granular fluid. The bulk viscosity accounts for the resistance of the granular particles to deform. The RBCs are modelled as rigid spheres, so the bulk viscosity is set to zero. The shear viscosity is defined according to the Carreau-Yasuda viscosity model (Equation 2.8) using a User Defined Function (see Appendix B.1).

The external forces $\mathbf{F}_k$ that are taken into account are the interaction force between the phases $\mathbf{R}_{pk}$, the virtual mass force $\mathbf{F}_{vm,k}$ and the lift force $\mathbf{F}_{lift,k}$. The interaction force is the drag force that is encountered by a particle when moving through a fluid. The third law of motion implies that the same force is exerted by the particles on the fluid. The drag depends on the velocity difference between the phases, the diameter and the shape of the particle and the densities of both phases. It is modelled according to Schiller and Naumann (1935), whose model is generally applicable for all two-fluid systems. The general form for the interphase force $\mathbf{R}_{sp}$ and the interphase momentum

exchange coefficient β_{sp} are:

$$\mathbf{R}_{sp} = \sum_{s=1}^{n} \beta_{sp}(\mathbf{u}_s - \mathbf{u}_p) \tag{3.12}$$

$$\beta_{sp} = \frac{\varepsilon_p \varepsilon_s \rho_s f}{(\tau_{part})} \tag{3.13}$$

$$\tau_{part} = \frac{\rho_s d_s^2}{18\mu_p} \tag{3.14}$$

$$\tag{3.15}$$

where subscript p stands for the primary phase (plasma) and subscript s for the secondary particulate phase. τ_{part} is the particle relaxation time and f is the friction factor. The drag coefficient C_d and the expression for f from the model of Schiller and Naumann (1935) are given by

$$f = \frac{C_d Re_{part}}{24} \tag{3.16}$$

$$Re_{part} = \frac{\rho_p \left|\mathbf{u}_s - \mathbf{u}_p\right| d_s}{\mu_p} \tag{3.17}$$

$$\beta_{sp} = \frac{3}{4} C_d \frac{\rho_p \varepsilon_p \varepsilon_s \left|\mathbf{u}_p - \mathbf{u}_s\right|}{d_s} \tag{3.18}$$

$$C_d = \frac{24\left(1 + 0.15 Re_{part}^{0.687}\right)}{Re_{part}} \text{ for } Re_{part} \leq 1000 \tag{3.19}$$

$$C_d = 0.44 \text{ for } Re_{part} > 1000 \tag{3.20}$$

with the particle Reynolds number Re_{part}.

The virtual mass force arises because the fluid is deflected due to an accelerating or decelerating particle since the particle and the fluid can not occupy the same space. The force that is required to displace this fluid is called extra or virtual mass and can be described by

$$\mathbf{F}_{vm} = 0.5 \varepsilon_s \rho_p \left(\frac{D_p \mathbf{u_p}}{Dt} - \frac{D_s \mathbf{u_s}}{Dt} \right) \tag{3.21}$$

The material derivative $D\mathbf{x}/Dt$ of vector $\mathbf{x}$ is defined as:

$$\frac{D\mathbf{x}}{Dt} = \frac{\partial \mathbf{x}}{\partial t} + (\mathbf{x} \cdot \nabla)\,\mathbf{x} \tag{3.22}$$

The third external force that is taken into account is the lift force, which is the force exerted on a particle due to a velocity gradient in the primary phase. This velocity gradient causes the particle to rotate which leads to a force in the upward direction: the lift force.

$$\mathbf{F}_{lift} = -0.5 \rho_p \varepsilon_s (\mathbf{u}_p - \mathbf{u}_s) \times (\nabla \times \mathbf{u}_p) \tag{3.23}$$

CHAPTER 4

Discretization

In order to calculate the blood flow through a part of the vascular system, the domain is divided into small segments: control volumes or cells, ten thousands to a few million cells. The equations that determine the flow (see Chapter 3) are solved for each control volume. The weighting of the solutions from the adjacent cells in computing the values at the cell face is determined in the spatial discretization scheme. To come to a solution for a transient problem, the weighting of the former and current time step is described in the temporal discretization scheme. These schemes and a method for estimating the error due to the spatial discretization are described in this chapter.

4.1 Finite volume method

The integral from of the governing equations is solved for each control volume. The values of the variables are calculated at the centre of each control volume using volume integrals and surface integrals. These values at the cell centres are also known as the node values. In case of surface integrals one integrates over the fluxes through each face. The calculation of the node values using volume and surface integrals is called the Finite Volume Method (FVM).

Since the density of the RBCs is variable in the multiphase flow case, the compressible Navier-Stokes equations (Equations 3.4 and 4.1) are used and their discretization is described below.

$$\frac{\partial(\rho\mathbf{u})}{\partial t} + (\rho\mathbf{u}\cdot\nabla)\,\mathbf{u} = -\nabla p + \nabla\cdot\left[\mu\left(\nabla\mathbf{u} + (\nabla\mathbf{u})^T - \frac{2}{3}\nabla\cdot\mathbf{u}\mathbf{I}\right)\right] + \mathbf{F} \tag{4.1}$$

Integrating this equation over a cell with volume V and boundary S, combined with Gauss theorem

$$\int_V \nabla\cdot\mathbf{u}dV = \oint_S \mathbf{u}\cdot\hat{\mathbf{n}}dS \tag{4.2}$$

results in

$$\int_V \frac{\partial(\rho\mathbf{u})}{\partial t}dV + \oint_S \rho\mathbf{u}\,(\mathbf{u}\cdot\hat{\mathbf{n}})dS = -\int_V \nabla p dV + \oint_S \mu\left(\nabla\mathbf{u} + (\nabla\mathbf{u})^T - \frac{2}{3}\nabla\cdot\mathbf{u}\mathbf{I}\right)\cdot\hat{\mathbf{n}}dS + \int_V \mathbf{F}dV \tag{4.3}$$

The volume integrals result in one value per volume. Each control volume has a finite number of faces: six for the hexahedrals, four for the tetrahedrals and about five or six for the polyhedrals. The line integrals can be rewritten as the sum over all faces and Equation 4.3 changes into

$$\Delta V\frac{\partial(\rho\mathbf{u})}{\partial t} + \sum_{faces}\rho\mathbf{u}_\mathbf{f}\,(\mathbf{u}_\mathbf{f}\cdot\hat{\mathbf{n}})\,A_f = -\nabla p\Delta V + \sum_{faces}\left[\mu_f\left(\nabla\mathbf{u}_\mathbf{f} + (\nabla\mathbf{u}_\mathbf{f})^T - \frac{2}{3}\nabla\cdot\mathbf{u}_\mathbf{f}\mathbf{I}\right)\cdot\hat{\mathbf{n}}\right]A_f + \mathbf{F}\Delta V \tag{4.4}$$

The subscript f indicates that the face value is taken. The fluid variables are calculated at the cell centres. The face values are calculated according to a discretization scheme that determines the weighting factor of the adjacent cell centres. These schemes are discussed in the next Section.

4.1.1 Spatial discretization schemes

Central Differencing Scheme

The most straightforward discretization scheme is the Central Differencing Scheme (CDS). A cell face is a boundary between two cells and its position is defined at the centre of the line through two cell centres. The face value is calculated by arithmetic averaging the adjacent cell centre values. Three one-dimensional control volumes are shown in Figure 4.1: the west (W), central (P) and east (E) cell. The nodal values are indicated with a capital letter and the face values with a lower case letter. S is the distance between two cell faces and Δx denotes the distance between two nodes.

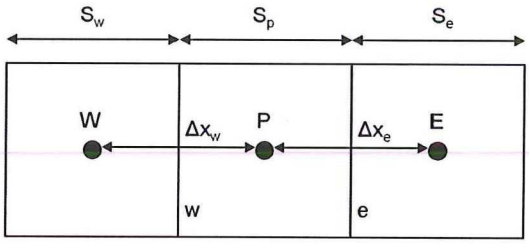

Figure 4.1: Schematic drawing of three one dimensional control volumes.

The value of ϕ for the west face in between W and P according to the CDS is computed as follows:

$$\phi_w = \frac{1}{2}(\phi_W + \phi_P) \tag{4.5}$$

Upwind Differencing Scheme

The CDS assumes that all adjacent cells are of equal importance in computing the face value. A different approach is the upwind differencing scheme (UDS) where the upwind node value is projected on the cell face. The western cell face value is now calculated as

$$\phi_w = \begin{cases} \phi_W & \text{if } u_w > 0 \\ \phi_P & \text{if } u_w < 0 \end{cases} \tag{4.6}$$

where u_w is the velocity at the western face, which is defined positively for a flow from west to east.

Second order schemes

Higher accuracy can be achieved by using more information from the adjacent cells in the calculation of the cell face value. In second order schemes node values and gradients are used to compute the face values. The general description of a second order scheme is (Ansys, 2011*b*)

$$\phi_e = \theta\left[\frac{S_e}{S_p + S_e}\phi_P + \frac{S_p}{S_p + S_e}\phi_E\right] + (1-\theta)\left[\frac{S_w + 2S_p}{S_w + S_p}\phi_P - \frac{S_p}{S_w + S_p}\phi_W\right] \tag{4.7}$$

The ratios that contain distances between cell faces (S) are weighting factors for the adjacent node values based on the cell size. θ determines to what extend the upwind and the downwind node values are taken into account. $\theta = 0$ results in the second order upwind scheme for which Equation 4.7 reduces to

$$\phi_e = \frac{S_w + 2S_p}{S_w + S_p}\phi_P - \frac{S_p}{S_w + S_p}\phi_W \tag{4.8}$$

$$= \phi_P + \frac{S_p}{S_w + S_p}(\phi_P - \phi_W) \tag{4.9}$$

$$\phi_{e,3D} = \phi_P + (\nabla\phi)_u \cdot \mathbf{r} \tag{4.10}$$

Equation 4.10 is the 3D version of the second order upwind scheme where **r** is the displacement vector between the upwind cell centre and the cell face centroid. The algorithm that is used to calculate the gradient is discussed later on in this section.

Another second order discretization scheme is QUICK (Quadratic Upstream Interpolation for Convective Kinetics). The most common value for θ is $1/8$, which roughly implies that the weighting factor for the downwind cells is $1/8$ and it is $7/8$ for the upwind values.

In the Fluent software a solution dependent value for θ is used to avoid introducing new solution extrema that could lead to numerical instability. The QUICK scheme is available for all mesh types, but θ is set to zero for non-hexahedral cells so the QUICK scheme is reduced to the second order upwind scheme.

Gradient algorithm

The gradient that is required for the second order schemes is calculated according to the Green-Gauss cell-based gradient algorithm. The gradient at the cell centre of the central cell is calculated as follows:

$$(\nabla\phi)_P = \frac{1}{V_P}\sum_{faces}\bar{\phi}_f\mathbf{A_f} \tag{4.11}$$

The averaged face value $\bar{\phi}_f$ is the arithmetic average of the cell centre values of the adjacent cells, that is why this method is called cell-based. V_P is the volume of the central cell and $\mathbf{A_f}$ is the normal vector of face f with the area A_f as magnitude.

4.1.2 Temporal discretization

Next to location dependent terms the Navier-Stokes equations (Equation 4.1) contain a time dependent term, the first one on the left hand side. This term is a function of the current time step and one or more preceding time steps. The generic expression for the time dependent term is

$$\frac{\partial\phi}{\partial t} = f(\phi) \tag{4.12}$$

$f(\phi)$ represents the spatial part of the Navier-Stokes equations. This section elaborates on the implicit and explicit formulations of the temporal discretization and the first order and second order schemes for the temporal discretization are described.

Implicit and explicit formulation

The temporal part of the Navier-Stokes equations could be calculated using values that are computed in the former time step or in the current time step. An explicit formulation is completely based on the previous time step, so it could be calculated directly, but this calculation method could lead to non-physical results. A first order example of the explicit formulation is

$$\frac{\phi^{n+1}-\phi^n}{\Delta t} = f(\phi^n) \tag{4.13}$$

$$\phi^{n+1} = \phi^n + \Delta t f(\phi^n) \tag{4.14}$$

$n+1$ indicates the current time step and n the former time step. f is solely based on the former solution, so there is no iterating between the former and current solution. This could lead to unboundedness for large Δt due to large changes between the former and current time step.

An implicit scheme is obtained by replacing $f(\phi^n)$ in Equations 4.13 and 4.14 by $f(\phi^{n+1})$. It can be solved iteratively before moving to the next time step, which makes it unconditionally stable at the expenses of a longer computational time. For this stability reason there is chosen to use an implicit time scheme. The first order and the second order implicit time schemes are described hereafter.

First order temporal implicit discretization

The value for ϕ in the current time step according to the first order implicit scheme is calculated as follows:

$$\frac{\phi^{n+1} - \phi^n}{\Delta t} = f(\phi^{n+1}) \tag{4.15}$$

$$\phi^{n+1} = \phi^n + \Delta t f(\phi^{n+1}) \tag{4.16}$$

ϕ^{n+1} is calculated iteratively.

Second order temporal implicit discretization

Just like with spatial discretization, the temporal discretization can be computed according to a second order scheme. In this case the second-last time step is taken into account next to the current and preceding time step. From physical perspective the second order derivative with respect to time is taken into account. A formulation of the second order temporal discretization can be as follows:

$$\frac{3\phi^{n+1} - 4\phi^n + \phi^{n-1}}{2\Delta t} = f(\phi^{n+1}) \tag{4.17}$$

This implicit time integration is solved iteratively for each time step according to

$$\phi^{n+1} = \frac{4}{3}\phi^n - \frac{1}{3}\phi^{n-1} + \frac{2}{3}\Delta t f\left(\phi^{n+1}\right) \tag{4.18}$$

4.1.3 Pressure-velocity coupling

The Navier-Stokes equations and the continuity equation are solved iteratively. The continuity equation (Equation 3.1) is discretized as follows:

$$\sum_{faces} J_{face} A_{face} = 0 \tag{4.19}$$

$$\sum_{faces} \rho u_n A_{face} = 0 \tag{4.20}$$

where $J = \rho u_n$ the mass flux is: the density multiplied with the velocity normal to face with area A. The iterative process starts with the computation of the velocity field from the Navier-Stokes equations with an estimated pressure field. Then the sum of the mass fluxes is calculated and a pressure correction factor is calculated to satisfy the continuity equation. The SIMPLE algorithm (Semi-Implicit Method for Pressure-Linked Equations) is used to calculate this corrected pressure from the momentum equations. The corrected pressure field is used to compute a new velocity field from the Navier-Stokes equations. This iterative process is repeated till the conservation equations are considered to be converged (See Section 4.1.5 on convergence).

4.1.4 Under-relaxation factors

The change that is allowed between two succeeding iterations is limited in order to enhance the convergence. The new value of a variable is a linear combination of the values calculated at the former and the current iteration. The under-relaxation factor (*URF*) specifies the allowed change and it has a value between 0 and 1:

$$\phi_{new} = \phi_{old} + URF \cdot (\phi_{new} - \phi_{old}) \tag{4.21}$$

For example *URFs* are specified for the calculation of the pressure, the velocity and the volume fraction. An *URF* is also used to limit the magnitude of the pressure correction in the pressure-velocity coupling.

4.1.5 Convergence and residuals

A computation is finished when the difference between two succeeding iterations is small enough, so the solution will not change up to a predefined precision when an extra iteration is performed. A measure for the change between two iterations is the imbalance in a conservation equation. A discretized form of a conservation equation can be written as:

$$a_P \phi_P = \sum_{nb} a_{nb} \phi_{nb} + b \tag{4.22}$$

where nb denotes all neighbour cells, a represents the coefficients belonging to the conservation equation and b is a constant source term. The residual R^ϕ is defined as the sum of the imbalance in the conservation equation over all cells:

$$R^\phi = \sum_{cells\ P} \left[\sum_{nb} a_{nb} \phi_{nb} + b - a_P \phi_P \right] \tag{4.23}$$

However, it is difficult to judge convergence based on the magnitude of the residual. Therefore scaling is employed based on the conserved property summed over the whole domain:

$$R^\phi = \frac{\sum_{cells\ P} \left| \sum_{nb} a_{nb} \phi_{nb} + b - a_P \phi_P \right|}{\sum_{cells\ P} |a_P \phi_P|} \tag{4.24}$$

A simulation is usually considered to be convergent when all scaled residuals have dropped at least three orders of magnitude compared to the first iteration.

4.2 Discretization error

All kinds of simulations are an approximation of reality. The error of a CFD simulation can be split in several categories like inaccurate approximation of the geometry, inappropriate simplification of the problem, unphysical boundary conditions and inaccurate discretization. This section focuses on the discretization error. This error for instance can be caused by using a too coarse mesh, highly squeezed cells or large volume differences between adjacent cells.

The computation of the discretization uncertainty is based on results of simulations using meshes with the one cell type and a range of densities. At least three systematically refined grids are required for this method. Systematic refinement is carried out if the refinement factors are identical in all directions. The method is based on Richardson Extrapolation where the mesh is refined with a factor 2 in each direction. A measure for uniform reporting on grid refinement studies is developed by Roache (1994). These guidelines are extended for non-uniform grid refinement by Roy (2010) and some practical problems are sorted out. Handles to determine the uncertainty based on the apparent order of accuracy are developed by Zou et al. (2010). These guidelines for reporting on discretization error are summarized in this section.

4.2.1 Uncertainty estimation and solution extrapolation

The discretization uncertainty is the difference between the solution to the discretized equations that are solved in numerical simulations and the solution to the mathematical model. The solution to the discrete equations f_h can be expressed as a Taylor series about the exact solution to the mathematical model $\tilde{f}$

$$f_h = \tilde{f} + \frac{\partial \tilde{f}}{\partial h} h + \frac{\partial^2 \tilde{f}}{\partial h^2} \frac{h^2}{2} + \frac{\partial^3 \tilde{f}}{\partial h^3} \frac{h^3}{6} + \cdots \tag{4.25}$$

$$f_h = \tilde{f} + g_1 h + g_2 h^2 + g_3 h^3 + \cdots \tag{4.26}$$

where h is a characteristic value for the mesh size defined as $h = \left(\frac{\text{geometry volume}}{\text{number of control volumes}} \right)^{1/3}$ for a 3D mesh. The derivatives in Equation 4.25 are replaced by coefficients g to obtain the power series of Equation 4.26.

When the mesh is systematically refined the characteristic lengths of both meshes are coupled via the refinement factor r:

$$r = \frac{h_{coarse}}{h_{fine}} \tag{4.27}$$

It turned out from experience that r should be at least 1.3 for proper uncertainty analysis (ASME, 2008). The Taylor series for the solution on the coarse mesh expressed in $h = h_{fine}$ is then

$$f_{rh} = \tilde{f} + \frac{\partial \tilde{f}}{\partial h} rh + \frac{\partial^2 \tilde{f}}{\partial h^2} \frac{(rh)^2}{2} + \frac{\partial^3 \tilde{f}}{\partial h^3} \frac{(rh)^3}{6} + \cdots \tag{4.28}$$

$$f_{rh} = \tilde{f} + g_1 rh + g_2 (rh)^2 + g_3 (rh)^3 + \cdots \tag{4.29}$$

For a mesh dependency analysis there are at least three systematically refined meshes required per cell type. The discretization uncertainty to quantify the accuracy of a solution is defined as the difference between the exact solution to the mathematical model and the exact solution to the discrete equation:

$$\varepsilon_h = f_h - \tilde{f} \tag{4.30}$$

If the numerical scheme is accurate to p^{th} order (see Section 4.1), all orders lower than p cancel out and Equation 4.30 becomes

$$\varepsilon_h = f_h - \tilde{f} = g_p h^p + g_{p+1} h^{p+1} + g_{p+2} h^{p+2} + \cdots \tag{4.31}$$

This equation is used to find new expressions for f_h and f_{rh}:

$$f_h = \tilde{f} + g_p h^p + g_{p+1} h^{p+1} + g_{p+2} h^{p+2} + \cdots \tag{4.32}$$

$$f_{rh} = \tilde{f} + g_p (rh)^p + g_{p+1} (rh)^{p+1} + g_{p+2} (rh)^{p+2} + \cdots \tag{4.33}$$

These equations are combined to generate a new expression for $\tilde{f}$ in which g_p is eliminated:

$$\tilde{f} = f_h + \frac{f_h - f_{rh}}{r^p - 1} + g_{p+1} h^{p+1} \frac{r^p (r-1)}{r^p - 1} + \cdots \tag{4.34}$$

A better estimation of the exact solution could be achieved by subtracting all terms with order $p + 1$ or a higher order from $\tilde{f}$. Substituting $\tilde{f}$ from Equation 4.34 into this new expression leads to the generalized Richardson extrapolation estimate $\bar{f}$ in Equation 4.36 which is $p + 1$ order accurate.

$$\bar{f} = \tilde{f} - \left(g_{p+1} h^{p+1} \frac{r^p (r-1)}{r^p - 1} + \cdots \right) \tag{4.35}$$

$$\bar{f} = f_h + \frac{f_h - f_{rh}}{r^p - 1} \tag{4.36}$$

The exact error from Equation 4.31 can be estimated by replacing $\tilde{f}$ by $\bar{f}$. The estimated discretization uncertainty for the fine mesh with spacing h is then defined as

$$\bar{\varepsilon_h} = f_h - \bar{f} = -\frac{f_h - f_{rh}}{r^p - 1} \tag{4.37}$$

4.2.2 Observed order and Grid Convergence Index

It is assumed for the exact error (Equation 4.37) that all higher order terms cancel out and that no other error terms are present. the Grid Convergence Index (GCI) is proposed by Roache (1994) as a non-dimensional version of the exact error. A safety factor is included to account for the presence of other error types. The GCI is defined as

$$GCI = \frac{F_s}{r^p - 1} \left| \frac{f_{rh} - f_h}{f_h} \right| \tag{4.38}$$

The safety factor F_s is chosen to achieve a 95% certainty that the true solution is within the uncertainty band defined by the GCI, although there is discussion in the literature whether this certainty is reached in all cases (Roy,

2010). Roache (1998) provides guidelines for choosing the factor of safety F_s based on the number of available systematically refined grids and the observed order of accuracy $\hat{p}$.

If the values of variable f are close to zero the fraction $\frac{f_{rh}-f_h}{f_h}$ can basically achieve every value. Therefore the normalization is often omitted and the GCI is implemented as

$$GCI = \frac{F_s}{r^p - 1} |f_{rh} - f_h| \tag{4.39}$$

This implementation of the GCI has the same units as f.

The observed order of accuracy is the order p that can be computed from the solutions on systematically refined grids. For a grid that is refined twice with the same factor, the observed order $\hat{p}$ can be computed from Equations 4.32 and 4.33 according to:

$$\frac{f_{r^2h} - f_{rh}}{f_{rh} - f_h} = r^{\hat{p}} \tag{4.40}$$

where f_{r^2h} is the solution on the coarsest grid. For non-constant grid refinement factors $\hat{p}$ could be calculated iteratively according to (see Appendix A for derivation):

$$\hat{p}^{k+1} = \frac{\ln\left[\left(r_{12}^{\hat{p}^k} - 1\right)\left(\frac{f_3-f_2}{f_2-f_1}\right) + r_{12}^{\hat{p}^k}\right]}{\ln(r_{12}r_{23})} \tag{4.41}$$

with the formal order as initial estimation. f_1, f_2 and f_3 are the solution on a fine, middle and coarse grid respectively. r_{12}andr_{23} are the refinement factors r_{ab} used to obtain grid a from grid b.

F_s = 1.25 if solutions on three systematically refined grids are available and the observed order of accuracy matches the formal order of accuracy within 10%. If there are only two meshes available or the observed order doesn't match the formal order of accuracy, F_s = 3.0 should be used.

It has been observed in practice that the observed order of accuracy (Equation 4.41) becomes negative or up to ten times larger than the formal order of accuracy (Roy (2010) and Zou et al. (2010)). This could be due to non-uniform mesh refinement, meshing difficulties due to a complex geometry or the choice of the variable that is used for the uncertainty analysis. Extreme values for the ratio $\frac{f_3-f_2}{f_2-f_1}$ could be observed for f close to zero which results in extreme values for $\hat{p}$. Zou et al. (2010) proposed a method to adapt the GCI based on $\hat{p}$, see Table 4.1.

f_i is the solution on grid i and $\overline{f}$ is the extrapolated solution from Equation 4.36. A solution is called monotonic convergent when the exact solution or the reference solution is approached from either above or below at mesh refinement. When the solution is smaller than the reference solution on some coarse meshes and larger on others, the solution is called non-monotonic convergent. One could recognize the safety factors 1.25 and 3 from the *GCI* in Table 4.1. The denominator $r^p - 1$ from the GCI is not taken into account in these criteria, so this uncertainty is larger than the GCI.

Table 4.1: Definitions of the uncertainty due to the discretization of the geometry, depending on the observed order of accuracy.

		Definitions
Monotonic convergence: $\hat{p} > 0$		$\delta_{RE} = f_i - f$
$0 < \hat{p} < 0.95$	$U = \min(1.25\delta_{RE}, 1.25\Delta_M)$	$\Delta_M = \max(\lvert f_i - f_j \rvert)$
$0.95 \leq \hat{p} < 2.05$	$U = 1.25\delta_{RE}$	
$\hat{p} \geq 2.05$	$U = \max(1.25\delta_{RE}, 1.25\Delta_M)$	
Non-monotonic convergence: $\hat{p} < 0$		
$\hat{p} < 0$	$U = 3\Delta_M$	

CHAPTER 5

Flow in a 180° bended tube

It is mentioned in Chapter 2 that blood actually is multiphase fluid of Red Blood Cells (RBCs) and other particles suspended in plasma. Single-phase and multiphase models of blood flow through a 180° bended tube that is based on the coronary artery (Figure 5.1a) are carried out by Jung et al. (2006) in Fluent. Although the geometry is very different from the carotid bifurcation, this case is used to validate the settings for transient simulations using a multiphase and single-phase model with the Carreau-Yasuda viscosity model. Subsequently the same settings are used in a real patient's bifurcating carotid artery (Chapter 8). In this chapter the present results of the blood flow through the 180° bended tube are discussed and compared to the results of Jung et al. (2006).

5.1 Case description

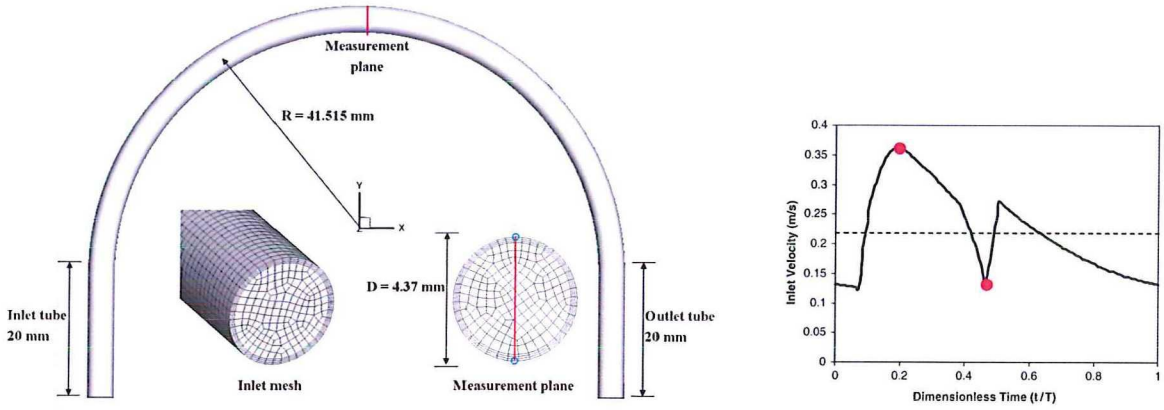

(a) Geometry

(b) Inlet velocity with $T = 0.73$s

Figure 5.1: Geometry, mesh and inlet velocity magnitude used in Jung et al. (2006). The mesh at the inlet and the mesh at the measurement plane at the top of the bend are shown as insets. Profiles are extracted along the red vertical line in the measurement plane and values are extracted at the top and the bottom of this line. The top is called the outer curve and the bottom the inner curve. The minimum, maximum and mean inlet velocities are $u_{min} = 12$ m/s, $u_{max} = 0.36$ m/s and $u_{mean} = 0.22$ m/s and u_{mean} is indicated by the dashed line.

The geometry which is displayed in Figure 5.1a is an idealized human coronary artery. It is modelled with rigid walls, a constant diameter $D = 4.37$ mm and a radius of curvature $R = 4.1515$. The results are extracted at the measurement plane which is located at the top of the geometry as indicated in Figure 5.1a. Velocity profiles and viscosity profiles are extracted along the vertical line that passes through the centre of the measurement plane. The WSS, strain rate and viscosity are extracted for each time-step at both ends of that vertical line, indicated by blue circles in measurement plane. These time sequences provide insight into the development of these variables over time.

Transient multiphase and single-phase blood flows through this tube are modelled in Fluent 14. The hematocrit (volume fraction of RBCs) is set to 0.45 for the single-phase simulation. The heart pulse that is used as inlet

boundary condition is displayed in Figure 5.1b and its period T is 0.73 s. The suspension of RBCs in plasma is modelled using the granular Euler-Euler approach described in Section 3.2. The drag force model of Schiller and Naumann (1935), the virtual mass force and the gravity in the negative y-direction, all described in Section 3.2, are included but the lift force is not. The Carreau-Yasuda model (Section 2.2.2) is employed as viscosity model. This model, the settings for the initialization and the properties of the RBCs and the plasma are summarized in Table 5.1. The mixture density and the density of plasma are fixed, so the density of the RBC-phase is variable. The Carreau-Yasuda model, the varying density and the inlet velocity pare programmed in User Defined Functions (UDFs, see Appendix B).

Table 5.1: Settings for the transient multiphase flow in a 180° bended tube.

Models	
Carreau-Yasuda viscosity model	$\mu_{mix} = \mu_{plasma} m\left(1 + (\lambda\dot{\gamma})^2\right)^{\frac{n-1}{2}}$ $n = 0.8092\varepsilon_{RBC}^3 - 0.8246\varepsilon_{RBC}^2 - 0.3503\varepsilon_{RBC} + 1$ $m = 122.28\varepsilon_{RBC}^3 - 51.213\varepsilon_{RBC}^2 + 16.305\varepsilon_{RBC} + 1$ $\mu_{plasma} = 0.001$ Pa·s $\lambda = 0.110$ s
	$\mu_{mix} = \varepsilon_{RBC}\mu_{RBC} + \varepsilon_{plasma}\mu_{plasma}$
Density	$\rho_{mix} = \varepsilon_{RBC}\rho_{RBC} + \varepsilon_{plasma}\rho_{plasma}$ $\rho_{mix} = 1080$ kg/m^3 $\rho_{plasma} = 1000$ kg/m^3
RBC diameter	$d_p = 8\mu$m
Boundary conditions	
Inlet volume fraction Uniform inlet velocity magnitude Wall velocity	$\varepsilon_{RBC} = 0.45$ heart pulse via UDF zero slip velocity for all phases
Initialization	
Volume fraction Velocities Exit reference pressure	$\varepsilon_{RBC} = 0.45$ $\mathbf{u} = \mathbf{0}$ m/s $p = 1.02 \cdot 10^4$ Pa

5.2 Dimensionless numbers

The characteristics of a pulsating flow in a curved geometry can be described by three dimensionless numbers. The characteristic values for the transient flow through the 180° tube are summarized in Table 5.2. The first dimensionless number is the Reynolds number, which is already introduced in the theory (Equation 3.6). *Re* is the ratio between the viscous forces and the inertial forces and a large *Re* indicates dominating inertial forces. For the multiphase flow *Re* is defined as

$$Re = \frac{\rho_{mix} u D}{\bar{\mu}_{mix}} \tag{5.1}$$

$\bar{\mu}_{mix}$ is the volume-fraction averaged viscosity averaged over the whole domain over one period, u is the velocity and D the tube diameter. $\bar{\mu}_{mix}$ is 0.0044 Pa·s and ρ_{mix} is fixed at 1080 kg/m^3.

The Dean number De describes the ratio of the centrifugal forces over the viscous forces. It is Re scaled with a measure for the curvature:

$$De = Re\sqrt{\frac{D}{2R}} \tag{5.2}$$

where R is the radius of curvature indicated in Figure 5.1a.

The third dimensionless number is the Womersley number in which the time-dependence is taken into account. It represents the ratio between the transient inertial forces and the viscous forces.

$$Wo = \sqrt{\frac{\rho_{mix}\omega u}{\mu_{mix}uR^{-2}}} = \frac{D}{2}\sqrt{\frac{\pi}{T}\frac{\bar{\rho}_{mix}}{\bar{\mu}_{mix}}} \tag{5.3}$$

T is the period of the transient flow which could be defined in several ways. The heart pulse shown in Figure 5.1b has a period of 0.73s so this is the maximum value for T. However, one could also argue that the semi-sinusoid in the interval $t/T = 0.12 - 0.47$ describes one period which would result in $T = 0.26$s. The two peaks in the cardiac cycle could also be seen as one period each, so then $T = 0.365$s

Table 5.2: Characteristic values for the dimensionless numbers that describe the flow through a 180° bended tube. The average mixture viscosity $\bar{\mu}_{mix} = 0.0044$Pa·s is used. The minimum velocity, maximum velocity and mean velocity are taken to obtain the three values for Re and De. Three frequencies could be specified from the heart-pulse (Figure 5.1b) and these are taken to calculate Wo.

Dimensionless number	Minimum	Maximum	Average
	$u = 0.13$m/s	$u = 0.36$m/s	$u = 0.22$
Re	134	382	232
De	31	75	53
	$T = 0.73$s	$T = 0.26$s	$T = 0.365$s
Wo	3.12	5.32	4.49

5.3 Results single-phase flow

Two single-phase simulations are carried out. In the most straightforward model blood is modelled as a Newtonian fluid with $\mu = 0.0037$ Pa·s which is the mean viscosity of human blood. The other single-phase model has a variable viscosity according to the Carreau-Yasuda model. Figures 5.2 to 5.5 show the Tangential Velocity, Molecular Viscosity and the Wall Shear Stress (WSS) results extracted in the measurement plane shown in Figure 5.2. Tangential velocity profiles are extracted along the vertical line in the measurement plane. The profiles at the peak inlet velocity and at the minimum inlet velocity are displayed in Figure 5.2. The systole (peak velocity due to contraction of the heart) velocity matches very well with Jung et al. (2006) although it is slightly larger near the outer wall. However, the velocity gradient at the outer wall corresponds well.

The viscosity development in time shown in Figure 5.3 is discussed in view of the inlet velocity pulse. It is extracted at the top and the bottom of the measurement plane as indicated by the blue circles. The flow acceleration at $t/T = 0.08$ results in a large velocity gradient at the wall, so $\dot{\gamma}$ increases. The shear-thinning viscosity decreases with increasing $\dot{\gamma}$ (see Figure 2.3a) as is indeed observed in Figure 5.2. As the acceleration starts to decrease at $t/T = 0.15$, $\dot{\gamma}$ decreases too so the viscosity increases. The large deceleration followed by a sudden acceleration between $t/T = 0.4$ and 0.5 induces a sharp peak in the viscosity. The viscosity gradually increases at the remaining part of the cardiac cycle where the flow rate smoothly increases.

The main discrepancies with Jung et al. (2006) occur at $t/T = 1.45$ where the flow rate suddenly decreases and then sharply increases. This could have been caused by the usage of too large time-steps that result in large changes in

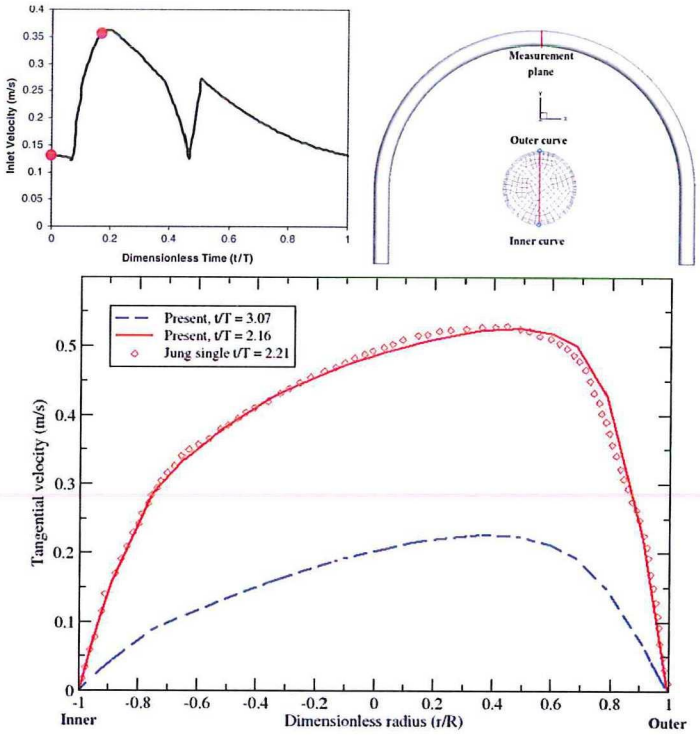

Figure 5.2: Tangential velocity profiles of the non-Newtonian single-phase flow extracted at the vertical line through the measurement plane for the smallest and largest inlet velocity.

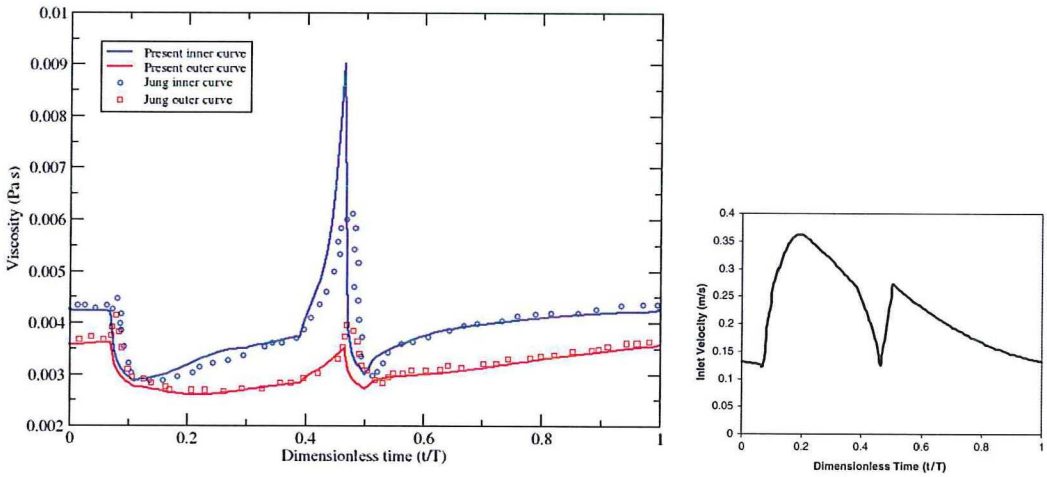

Figure 5.3: Time development of the viscosity of the single-phase flow with the Carreau-Yasuda viscosity model. The viscosity is extracted at the top and the bottom of the measurement plane.

the inlet velocity between succeeding time steps. However, an additional simulation is performed where the time-step is decreased from 10^{-2}s to 10^{-3}s. The results were not change so the time-step is not causing this mismatch.

Contour plots of the tangential velocity and the viscosity at the measurement plane are displayed in Figure 5.4. These plots are extracted at the same moments as the velocity profiles displayed in Figure 5.2. The secondary motions are indicated by vectors which show that the secondary velocities are about ten times smaller than the tan-

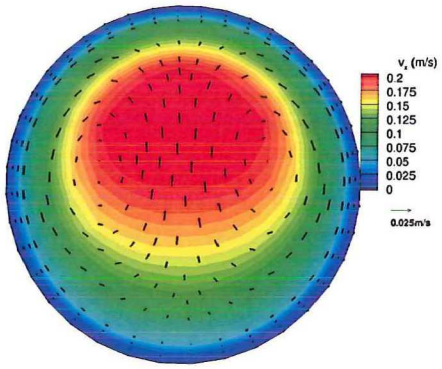

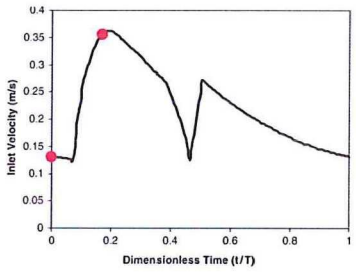

(a) Tangential velocity and secondary motions at t/T = 3.07

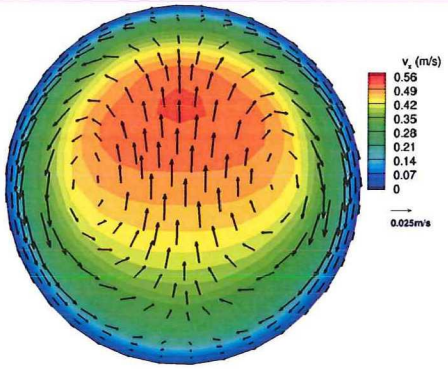

(b) Tangential velocity and secondary motions at t/T = 2.16

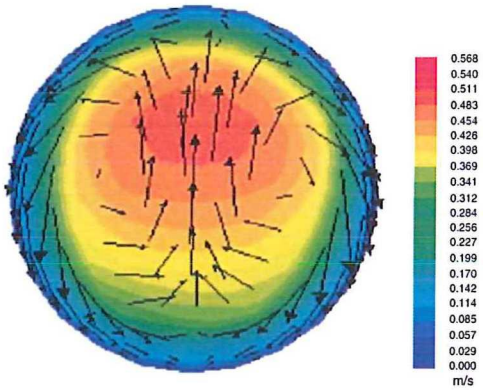

(c) Tangential velocity and secondary motions Jung et al. (2006) at t/T = 2.21

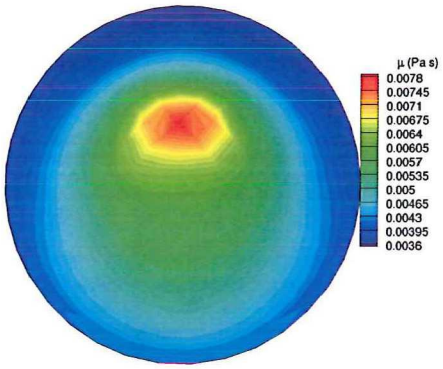

(d) Viscosity contours at t/T = 3.07

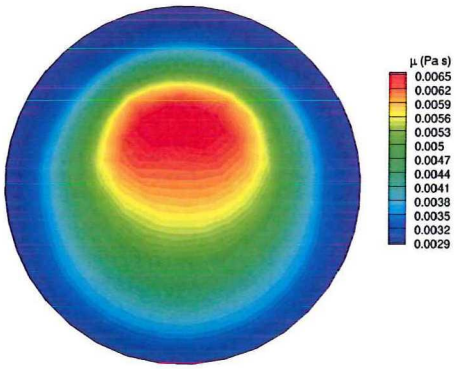

(e) Viscosity contours at t/T = 2.16

Figure 5.4: Velocity contours including the secondary motion and viscosity contours for the smallest and largest inlet velocity.

gential velocity for the smallest inlet velocity and about twenty times smaller for the peak velocity. The velocity contours and the pattern of the secondary motion at t/T = 2.16 resemble with Jung et al. (2006) although the scale of their vectors is unknown.

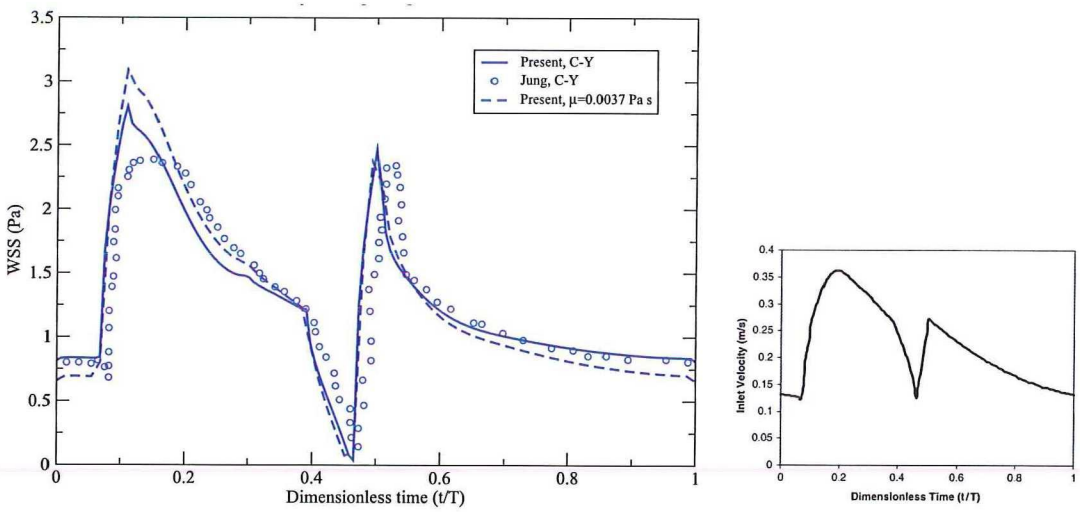

(a) WSS extracted at the top of the inner curve

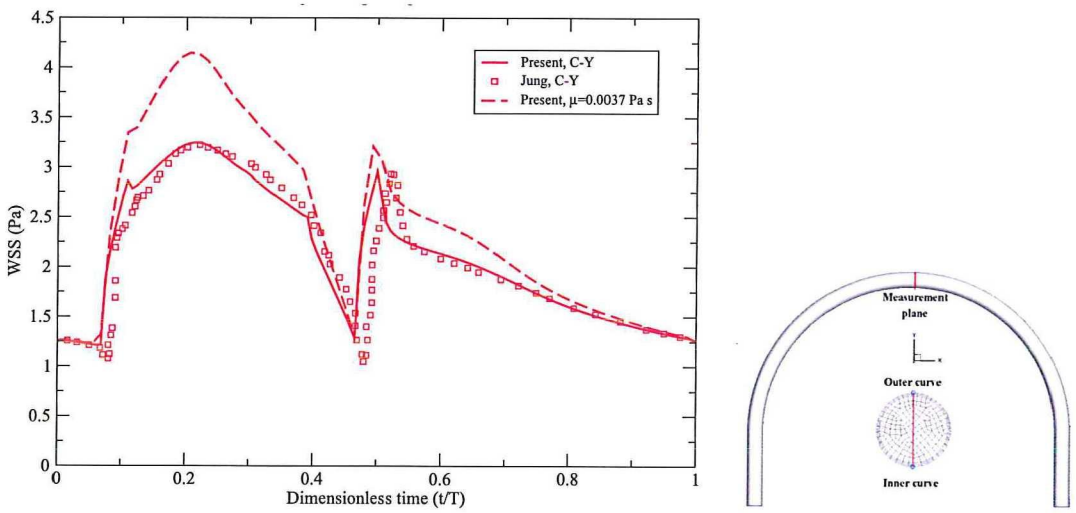

(b) WSS extracted at the top of the outer curve

Figure 5.5: WSS time-sequences of single-phase flow simulations.

It is observed from the viscosity contours (Figures 5.4d and 5.4e) that the location of the maximum viscosity coincides with that of the maximum tangential velocity. The spatial velocity gradient is smallest at the top of the velocity profile(Figure 5.2), so $\dot{\gamma}$ is small resulting in a large viscosity. $\dot{\gamma}$ is smallest for small velocities which explains the larger viscosity for $t/T = 3.07$.

The WSS time-sequences extracted at the top and bottom of the measurement plane for both single-phase flows are shown in Figure 5.5. The WSS is proportional to the gradient of the tangential velocity in the direction normal to the wall and it is proportional to the molecular viscosity (see Equation 2.1). First of all the WSS due to the non-Newtonian single-phase flow is discussed followed by a consideration on the differences between the WSS due to the two single-phase flows. The sudden acceleration at the beginning of the cardiac cycle ($t/T = 0.08$) results in a fast increase in the velocity gradient, especially at the wall. This increase is much larger than the decrease

of the viscosity due to the increased $\dot{\gamma}$ so the WSS increases. When the acceleration reduces at $t/T = 0.15$ and subsequently the peak velocity is reached, the WSS decreases due to a decreasing velocity gradient and a barely increasing viscosity. The sudden acceleration of the flow at $t/T = 0.45$ induces another peak in the WSS profile. The cycle ends with a gradually decelerating fluid which results in a gradually decreasing WSS.

The WSS at the inner curve overshoots Jung's results with $15 - 30\%$ at the beginning of the systole ($t/T = 0.08$) while the viscosity is underestimated at that time (See Figure 5.3) compared to Jung et al. (2006). This smaller viscosity could lead to a larger velocity gradient which causes the larger WSS.

The WSS development due to the Newtonian flow at the inner curve shows that the Carreau-Yasuda model has a damping effect on the WSS, since the Newtonian peaks are slightly larger and the lower values slightly lower. This corresponds to the expectations from the biological point of view that the forces at the blood vessels are as small as possible. Physically seen the viscosity is reduced in regions of large strain rate due to the shear-thinning viscosity model. $\dot{\gamma}$ is largest for large velocities like those at the interval $t/T = 0.1 - 0.35$. The viscosity of the non-Newtonian fluid in this time-period is about 30% smaller at the outer curve than the Newtonian viscosity of 0.0037 Pa·s (See Figure 5.3) and the WSS is also about 30% smaller.

5.3.1 Conclusion on single-phase flow

The difference in WSS between the Newtonian and non-Newtonian single-phase flow indicates that it is necessary to use a non-Newtonian viscosity model to mimic human blood in a large bended artery. The largest difference is observed for high velocities where $\dot{\gamma}$ is large at the wall. The non-Newtonian viscosity is reduced with about 30 % compared to μ_{Newton} =0.0037 Pa·s. The results of the simulations with the single-phase Carreau-Yasuda viscosity model agree with Jung et al. (2006)e. This implies that the settings in Fluent 14 are similar and that the user defined functions (UDFs) that describes the transient inlet velocity magnitude and the RBC density are implemented correctly.

5.4 Two-phase flow

To have a better approach of the composition of blood it is modelled as a two-phase flow of Red blood Cells (RBCs) suspended in plasma. The results are compared to Jung et al. (2006) and to the present single-phase results. First of all the velocity profiles and the viscosity profiles along the vertical line in the measurement plane are extracted at the peak velocity and the lowest velocity, at the same times as for the single-phase flow. Figure 5.6 shows that the velocity profile at the peak velocity is more similar to the single-phase results from Jung et al. (2006) than to their multiphase results. The more asymmetric velocity profiles result in viscosity profiles that have the same trends as Jung et al. (2006). The peak of the viscosity profile is shifted toward the outer curve just like the peak of the velocity profile. The values at the wall are quite consistent with Jung et al. (2006).

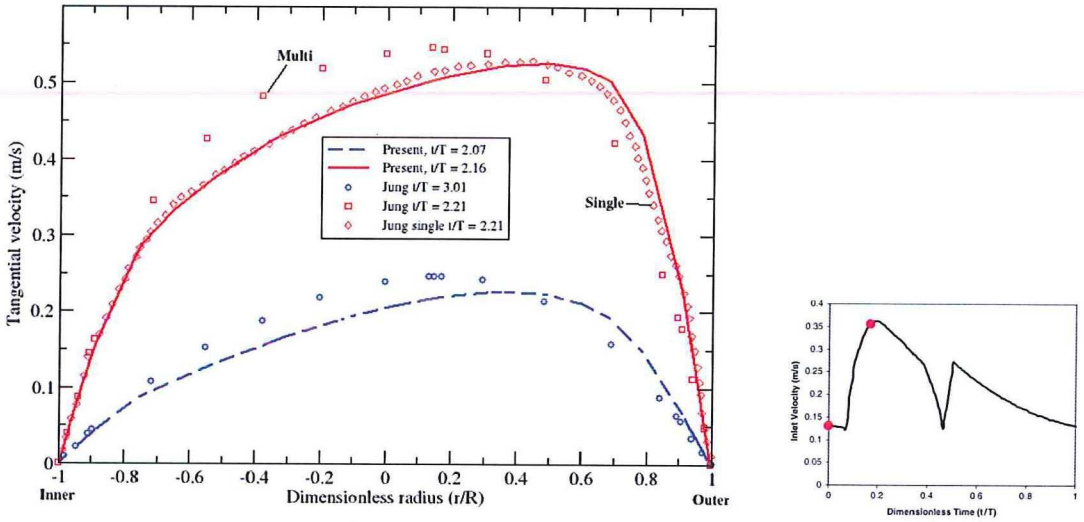

(a) Tangential velocity

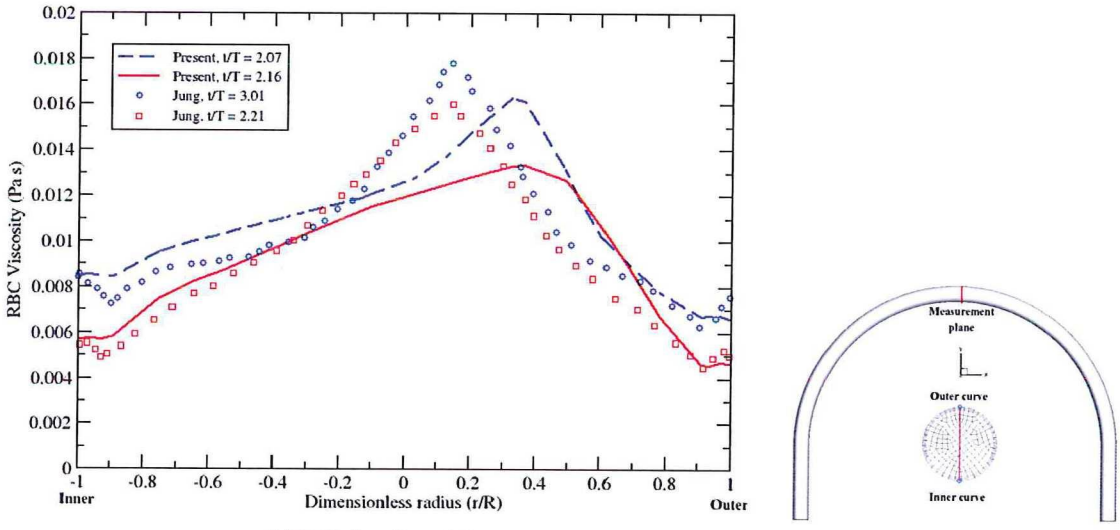

(b) RBC viscosity scaled

Figure 5.6: Viscosity and tangential velocity for multiphase flow.

Contours are extracted at the measurement plane for the tangential velocity, the RBC viscosity and the mixture

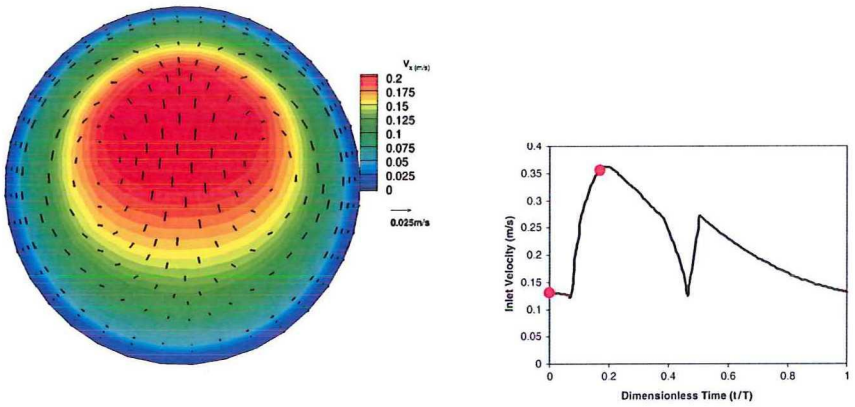

(a) Tangential velocity and secondary motion at t/T = 2.07

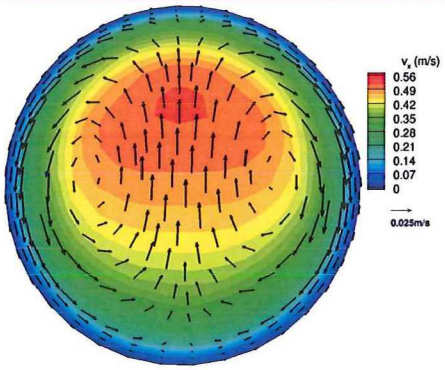

(b) Tangential velocity and secondary motion at t/T = 2.16

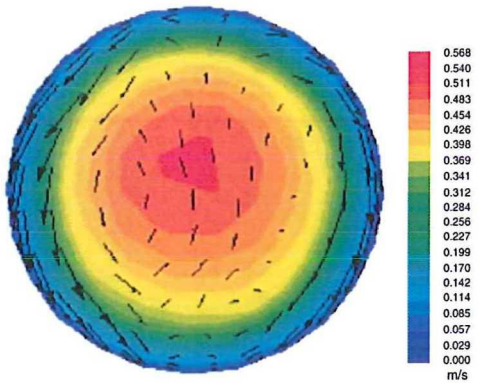

(c) Tangential velocity and secondary motions Jung et al. (2006) at t/T = 2.21

Figure 5.7: Velocity contours including the secondary motion for the lowest inlet velocity and the peak velocity.

viscosity. The velocity contours from Figure 5.7 indeed show more resemblance to the single-phase results than to the multiphase flow in Figure 5.7c. The mixture viscosity contours that are shown in Figure 5.8 are practically identical to the viscosity contours obtained from the non-Newtonian single-phase flow in Figure 5.4.

The RBC volume fraction (ε_{RBC}) is quite constant over time as one can see in Figure 5.9a, but there is some spatial dependence. The RBCs are transported to the inner curve due to the secondary flow induced by the centrifugal force (see Figure 5.7). This results in a stagnation point at the top and bottom of the measurement plane where a decreased or increased concentration of RBCs is observed respectively. At least one cardiac cycle is required for the secondary flow to develop and to obtain a heterogeneous RBC distribution. When the spatial distribution of ε_{RBC} is set it is retained by the continuously present secondary flow.

The influence of the deviation of ε_{RBC} from 0.45 on the viscosity is depicted in Figure 5.9b by plotting viscosity ratios as functions of the strain rate. The difference in viscosity from the single-phase flow (ε_{RBC} = 0.45) could be as large as 12 % at the inner curve and 8 % at the outer curve for very small strain rates. Therefore a viscosity increase of 5 to 10 % is expected at the inner curve when this graph is combined with the time sequence of the RBC strain rate in Figure 5.9c. A decline of only a few percent is expected at the outer curve.

The influence of the numerical scheme on the strain rate is visualized in Figure 5.9c where the strain rate is shown

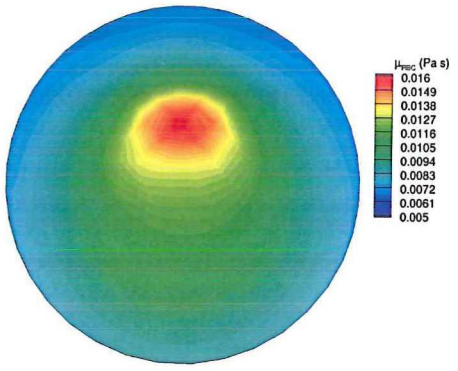

(a) RBC viscosity contours at $t/T = 2.07$

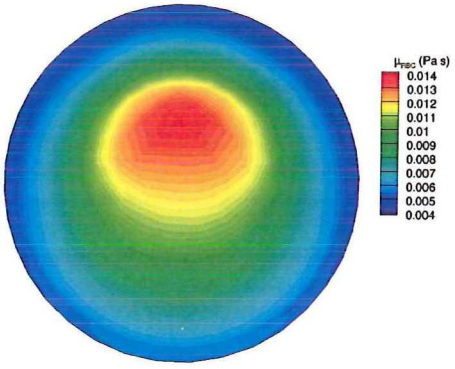

(b) RBC viscosity contours at $t/T = 2.16$

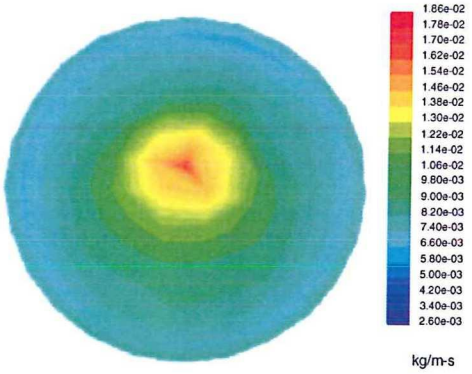

(c) RBC viscosity contours Jung et al. (2006) at $t/T = 3.01$

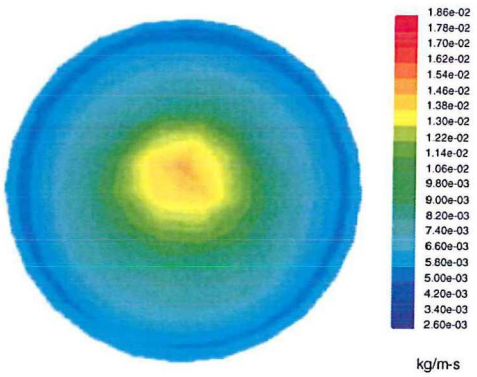

(d) RBC viscosity contours Jung et al. (2006) at $t/T = 2.21$

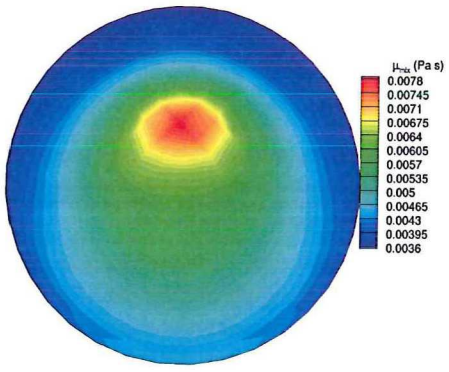

(e) Mixture viscosity contours at $t/T = 2.07$

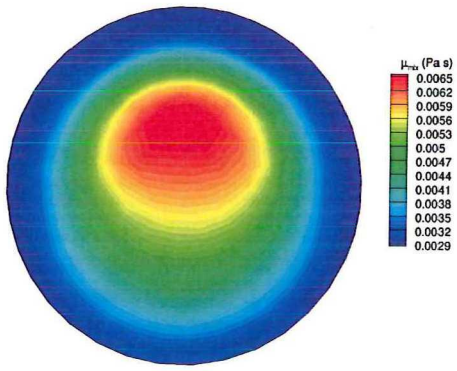

(f) Mixture viscosity contours at $t/T = 2.16$

Figure 5.8: RBC viscosity and mixture viscosity contours for the lowest inlet velocity and the peak velocity. The legend from Jung et al. (2006) applies to both (c) and (d). The mixture viscosity is volume fraction averaged.

for the first order upwind scheme and for the quick scheme. The largest difference is observed at the inner curve where the difference is as large as 20 % for over 10% of the cardiac cycle. The larger radius of curvature at the outer curve compared to the inner curve causes less dissimilarity for $\dot{\gamma}$.

The trends of the WSS time-sequences are the same as in Jung et al. (2006), namely that it is similar to the inlet velocity pulse. The WSS for phase n is calculated according to

$$\tau_n = \mu_n \dot{\gamma}_n \varepsilon_n \tag{5.4}$$

The mixture WSS is therefore the sum of the WSS due to plasma and RBC. For the inner curve this results in a reasonable agreement with Jung et al. (2006), whereas the RBC-WSS at the outer curve matches with the mixture WSS due to the larger velocity gradient.

Another comparison is made by plotting the viscosity time-sequence at the inner curve and the outer curve in Figure 5.11. The present RBC-viscosity at the inner curve and the volume fraction averaged mixture viscosity resemble with Jung et al. (2006). The mixture viscosity at the outer curve also resembles with the results of Jung et al. (2006) although the difference appears to be larger than at the inner curve due to the scaling. However, the mixture viscosity has the same order of magnitude and peaks are observed at the same locations.

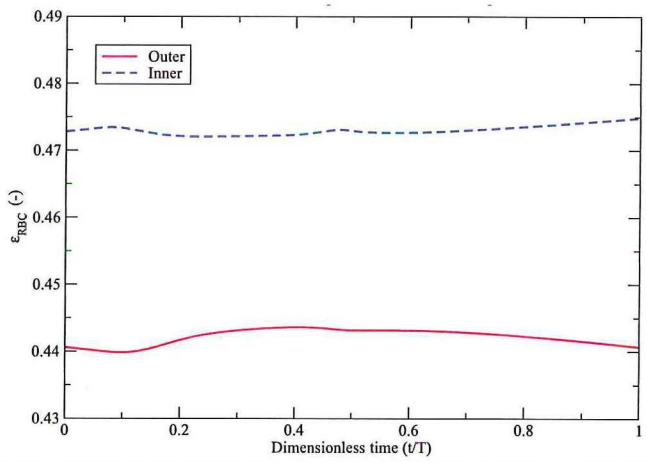

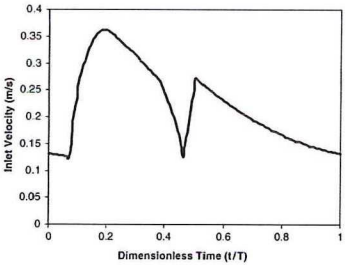

(a) RBC volume fraction

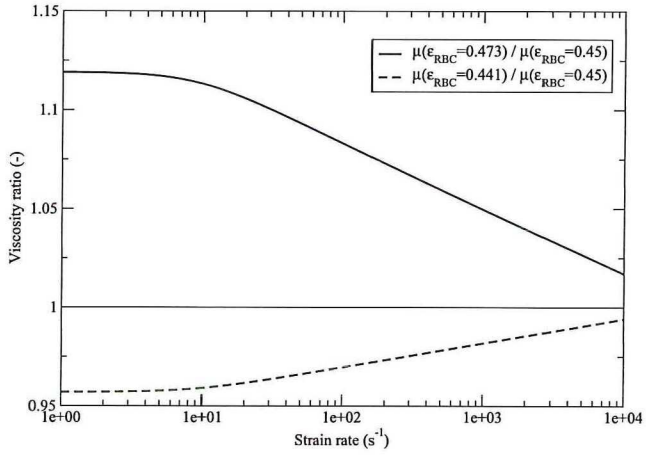

(b) Viscosity ratios

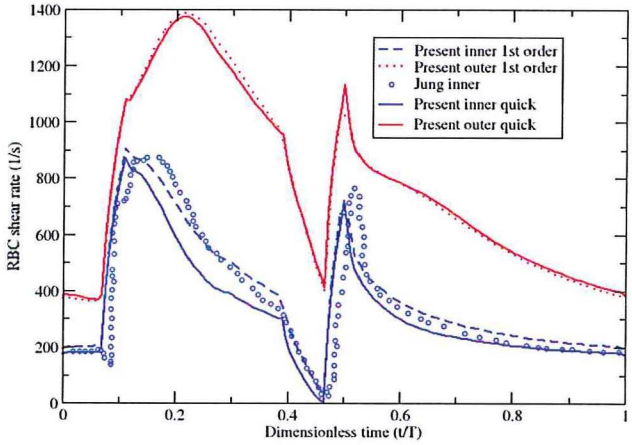

(c) Strain Rate, first order vs quick

Figure 5.9: Development in time for RBC volume fraction and Strain Rate for multiphase flow is displayed in figure (a) and (b). The ratios of the viscosity described by the Carreau-Yasuda model for the RBC volume fractions displayed in (a) over the mean RBC volume fraction of 45% is visualized in (c).

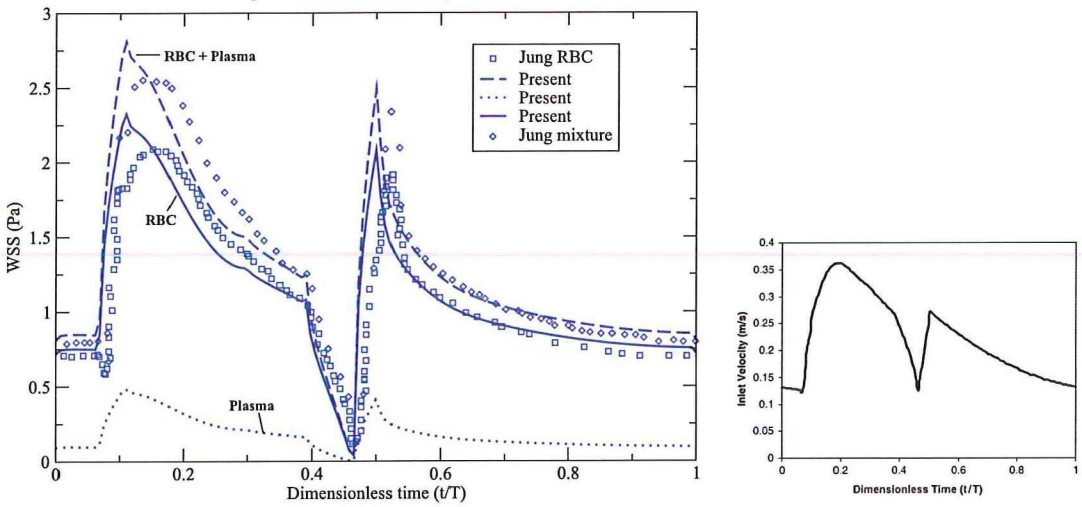

(a) WSS inner curve

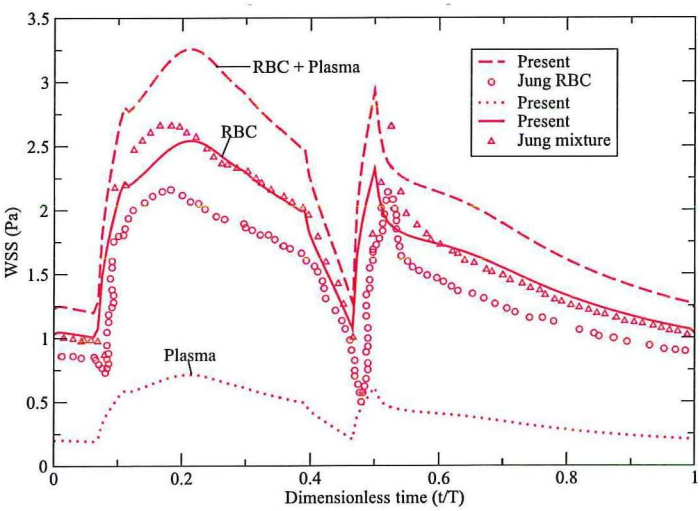

(b) WSS outer curve

Figure 5.10: WSS extracted at the inner and outer curve for multiphase flow.

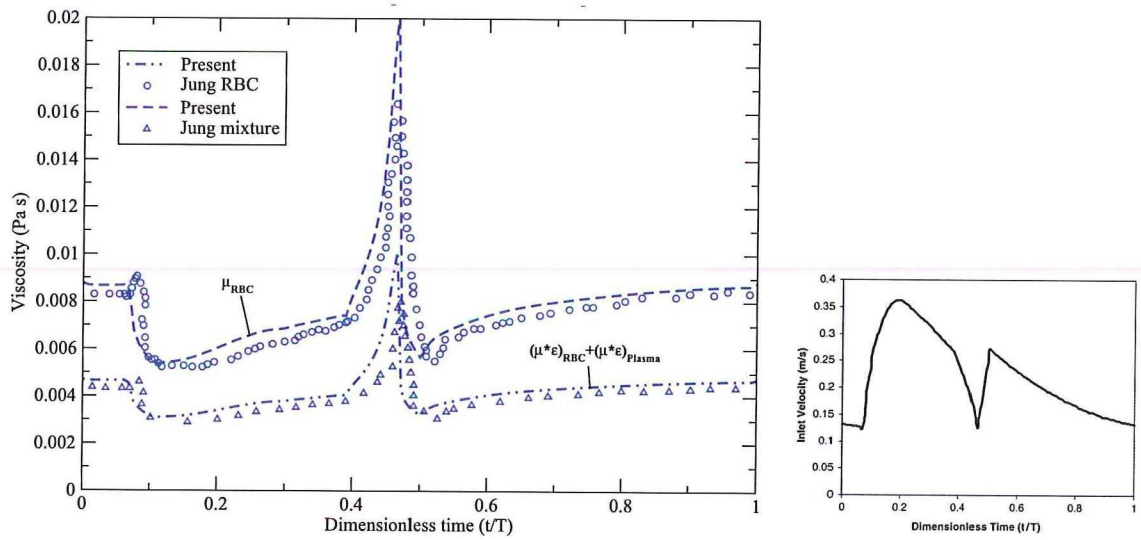

(a) Viscosity inner curve

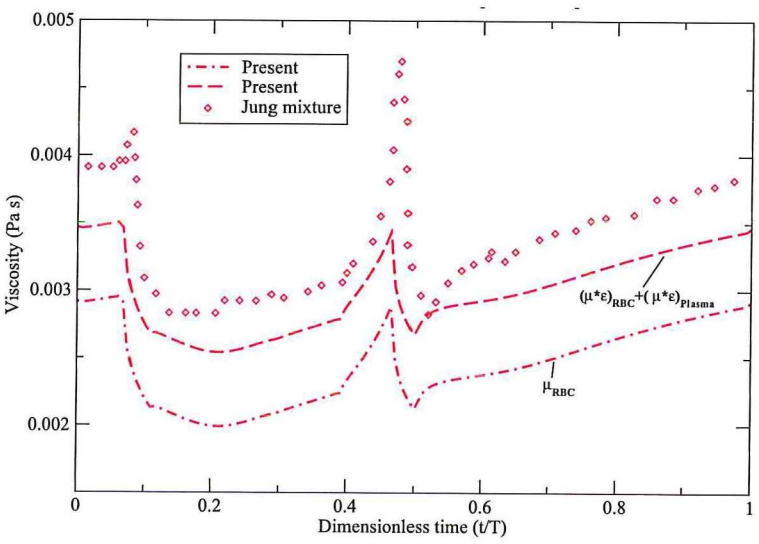

(b) Viscosity outer curve

Figure 5.11: Viscosity time sequences for multiphase flow for RBC and whole blood.

5.5 Comparison single-phase and multiphase flow

The results for the viscosity and the WSS are plotted for single-phase and multiphase flows in Figure 5.12. The multiphase flow has a larger viscosity at the inner curve and a slightly smaller viscosity at the outer curve, both due a variance of the RBC volume fraction compared to the fixed 0.45 for the single-phase flow.

For the WSS the difference between the non-Newtonian single-phase and multiphase simulations is observed to be negligible. Combining these results with the difference in viscosity indicates that the velocity gradient at the wall is slightly different at the inner curve. The time intervals at which a larger WSS is observed for the Newtonian flow coincides with the largest deviation of the non-Newtonian viscosity from 0.0037 Pa·s.

5.6 Conclusion 180° bended tube

The flow of blood modelled as a non-Newtonian fluid using the Carreau-Yasuda model induces a smaller WSS for high velocities than blood modelled as a Newtonian fluid. Changing the model from a single-phase to a non-Newtonian multiphase flow with RBCs suspended in plasma does not induce a significant change in the WSS. Therefore it is concluded that the non-Newtonian viscosity model is required for a blood flow through a bended tube with constant diameter described by $134 < Re < 382$, $31 < De < 75$ and $3.12 < Wo < 5.32$, but the multiphase approach is not necessary.

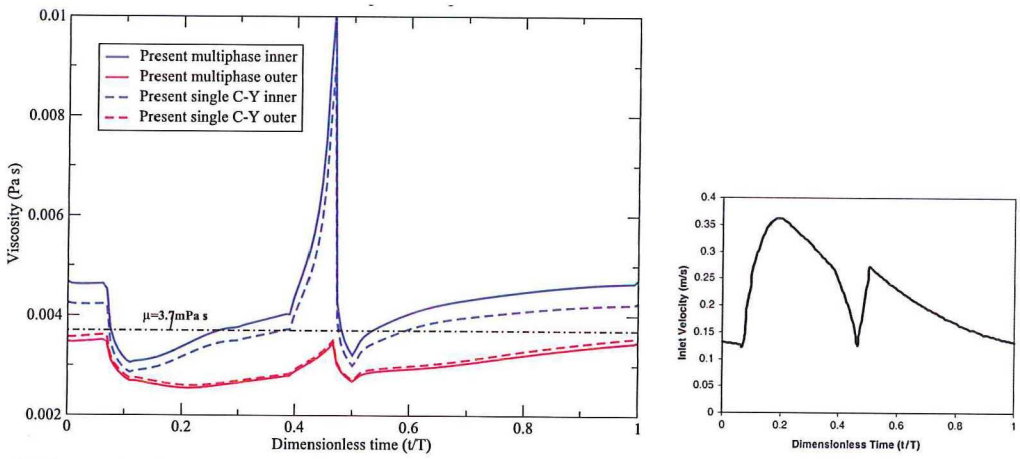

(a) Mixture viscosity of multiphase flow and viscosity of single-phase flow at both the inner curve and the outer curve

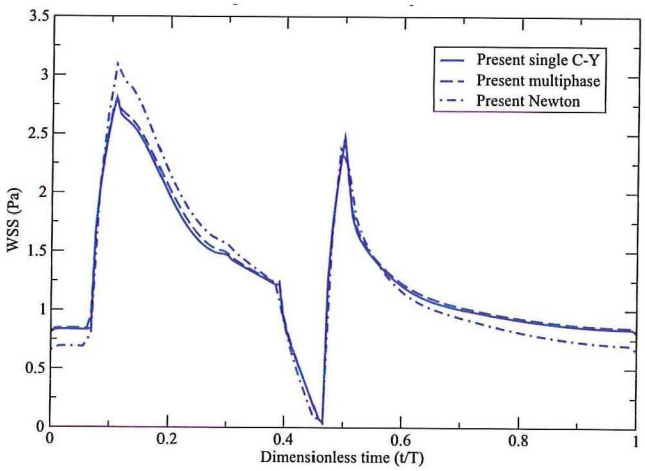

(b) WSS inner curve for multiphase and single-phase flows

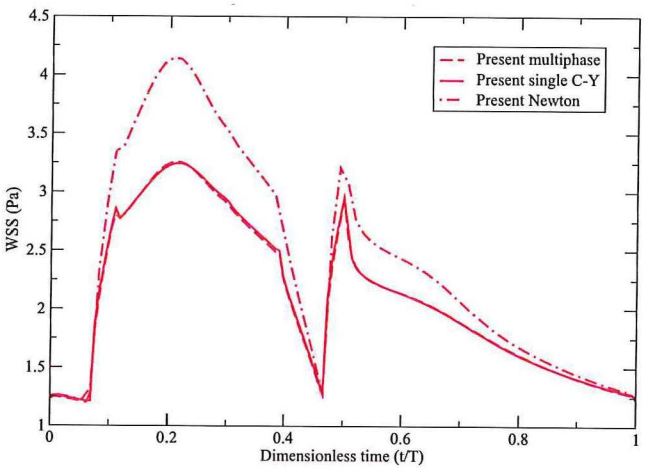

(c) WSS outer curve for multiphase and single-phase flows

Figure 5.12: Viscosity and WSS time-sequences for multiphase and single-phase flows compared. The values for the multiphase simulations are volume fraction averaged.

CHAPTER 6

Flow in a rapidly expanding tube

Predicting the beginning and development of atherosclerosis could be one of the applications of a CFD model of the vascular system. A simplified geometry of a diseased artery could be a suddenly expanding tube. Karino and Goldsmith (1977) performed experiments with 1 % hardened human RBCs in water in a suddenly expanding tube. The velocity patterns and the properties of the recirculation zones are examined and compared to computed 2D FD (Finite Difference) stream functions from Macagno and Hung (1967). Jung and Hassanein (2008) validated their two-phase CFD model of blood in Fluent 6.1 with these experiments and computed stream functions. Besides this very dilute flow Karino and Goldsmith (1977) carried out some qualitative studies with suspensions of 15 to 30 vol-% RBCs in platelet-poor plasma and with real blood containing 45 vol-% RBCs.

A schematic drawing of the setup, the computation geometry and two cross sections of the mesh are shown in Figure 6.1. The small tube is 750μm long and the broad tube 2200μm. The mesh is an unstructured hexahedral mesh containing 397 k cells and it is constructed using the Cooper scheme in Gambit.

The influence of Re and ε_{RBC} is examined by performing three simulations for each combination of Re and ε_{RBC} (hematocrit level, volume-% of RBCs) and the results are compared with the experiments and simulations mentioned above. Re is defined in the small tube close to the expansion according to

$$Re = \frac{\rho_{mix}\bar{u}D_1}{\bar{\mu}_{mix}} \tag{6.1}$$

In multiphase flows ρ_{mix} is the mixture density, $\bar{u}$ is the mean velocity, D_1 the diameter of the small tube and $\bar{\mu}_{mix}$ the volume fraction averaged mixture viscosity. In the single-phase models it holds that $\rho_{mix} = \rho$ and $\bar{\mu}_{mix} = \bar{\mu}$. At first blood is modelled as a single-phase Newtonian fluid. Then the agreement with the blood flow is improved by implementing a non-Newtonian single-phase fluid. In the most complicated simulations a two-phase fluid model with non-Newtonian RBCs suspended in Newtonian plasma is implemented. All external forces mentioned for the multiphase flow in Section 3.2 are included: drag force according to the Schiller-Naumann model, gravity in the -z direction, virtual mass force and lift force.

6.1 Hematrocit level 0.01

The first sequence of simulations represents 1 volume-% hardened RBCs with average diameter of 7.5μm in water. Pure water is used as the fluid in the Newtonian simulation. The settings for the computed flows with $Re = 12.2$ and $Re = 37.8$ (computed according to Equation 6.1) for $\varepsilon_{RBC} = 0.01$ are given in Table 6.1.

The velocity contours and stream traces for $Re = 12.2$ are displayed in Figure 6.2 and for $Re = 37.8$ in Figure 6.3. Three characteristic parameters L, Y_0 and Z_0 for the recirculation zones (See Figure 6.1a) are shown in Table 6.2. The recirculation length L is defined as the distance between the sudden expansion and the stagnation point at the wall at the end of the vortex. The largest recirculation zone is observed for pure water because of less viscous dissipation. The recirculation lengths observed in the Newtonian simulations are the largest, but these are still smaller than the experimental results (Karino and Goldsmith, 1977). This might be caused by a different length of the small tube and the inlet boundary condition. The length of the inlet is undefined in both Karino and Goldsmith (1977) and Jung and Hassanein (2008). In the present study a small tube of 0.75 mm is used and the flow is fully developed at the end of the small tube. A parabolic velocity profile with the same mass flux as applied by Karino

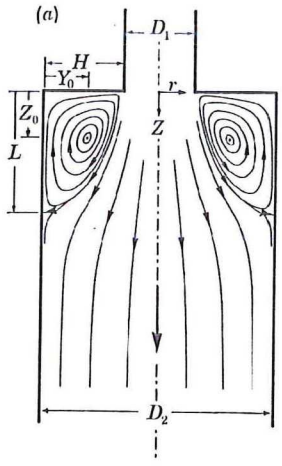

(a) Schematic drawing setup

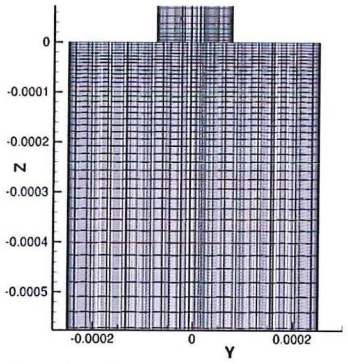

(b) Mesh at plane x=0 m. Y and Z are in meters.

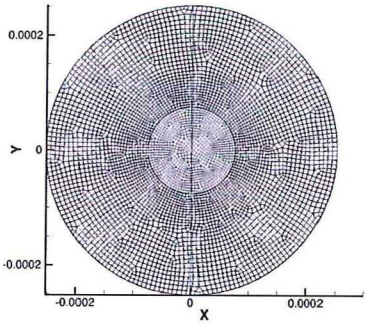

(c) Mesh at plane z=0 m, x and y are in meters.

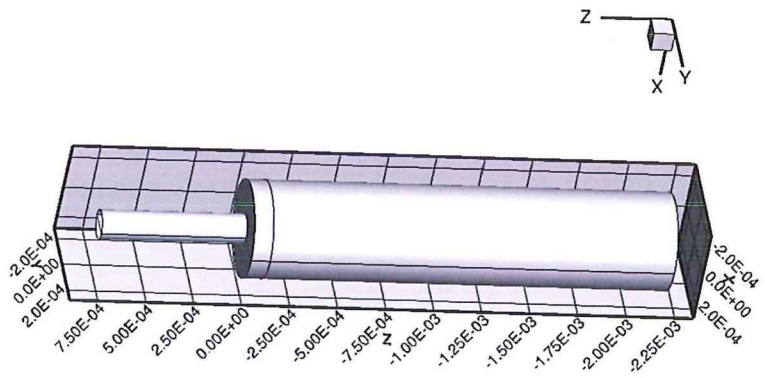

(d) Geometry, x, y and z are given in meters.

Figure 6.1: Schematic drawing of the suddenly expanding tube. The tubes diameters are $D_1 = 151\mu$m and $D_2 = 504\mu$m. $Z = 0$ m is defined at the expansion and $X = 0$ m and $Y = 0$ at the centre of the tube. Y_0 and Z_0 are the coordinates of the centre of the recirculation zone and L indicates the length of the recirculation. Finally H is the distance between the walls of the large and the small tube and r is the distance from the centre of the tubes.

and Goldsmith (1977) and Jung and Hassanein (2008) is used as boundary condition in the present study while a uniform velocity is used in their researches. Since the length of the small tube is unknown it is not clear whether the flows are fully developed at the end of the small tube in Karino and Goldsmith (1977) and Jung and Hassanein (2008). An undeveloped flow would result in a larger recirculation zone because the velocity near the wall of the small tube is larger. This implies that there is less kinetic energy at the centre of the tube and more at the edge that feeds the recirculation zone.

Before the difference in recirculation lengths between the three flow types is discussed in more depth there is focused on the viscosity distribution. In order to quantify the importance of using a non-Newtonian viscosity model, Johnston et al. (2004) introduced the local non-Newtonian importance factor I_l.

$$I_l = \frac{\mu}{\mu_N} \tag{6.2}$$

where μ_N is the constant viscosity used in the single-phase Newtonian simulation. Contour plots of I_l are used to compare the viscosity distributions in the non-Newtonian single-phase flow and the multiphase flow in Figure 6.4.

Table 6.1: Settings for the flows in a suddenly expanding tube for the case with the initial hematocrit $\varepsilon_{RBC} = 0.01$. The Carreau-Yasuda viscosity model is also used for the single-phase flow, fixing ε_{RBC} at 0.01.

Models	
Carreau-Yasuda viscosity model	$\mu_{mix} = \mu_{water} m\left(1 + (\lambda\dot{\gamma})^2\right)^{\frac{n-1}{2}}$ $n = 0.8092\varepsilon_{RBC}^3 - 0.8246\varepsilon_{RBC}^2 - 0.3503\varepsilon_{RBC} + 1$ $m = 122.28\varepsilon_{RBC}^3 - 51.213\varepsilon_{RBC}^2 + 16.305\varepsilon_{RBC} + 1$ $\mu_{water} = 0.001$ Pa·s $\lambda = 0.110$ s $\mu_{mix} = \varepsilon_{RBC}\mu_{RBC} + \varepsilon_{water}\mu_{water}$
Density	$\rho_{water} = 1000$ kg/m^3 $\rho_{RBC} = 1130$ kg/m^3 $\rho_{single-phase} = 1000$ kg/m^3
Particle diameter	$d_p = 7.5\mu$m
Boundary conditions	
Inlet volume fraction	$\varepsilon_{RBC} = 0.01$
Inlet velocity	parabolic profile with $\bar{u} = 0.0757$m/s ($Re = 12.2$) parabolic profile with $\bar{u} = 0.233$m/s ($Re = 37.8$)
Wall velocity	zero slip velocity for all phases
Zero gradient at outflow	
Initialization	
Volume fraction	$\varepsilon_{RBC} = 0.01$
Velocities	$\mathbf{u} = \mathbf{0}$ m/s

It can be seen from the Carreau-Yasuda viscosity model (Table 6.1) that the viscosity increases for low and very low strain rates. The velocity is small at the centre of the recirculation zone and close to the edge of the large tube. These locations indeed coincide with the regions of large I_l in the single-phase contour plots. In the multiphase flow it is observed that the RBCs are swung out of the vortex and there is a small accumulation in the centre of the stream and a larger accumulation at the wall. This is because the inertial forces in the z-direction are larger than in the other directions. Similar trends are observed for I_L and ε_{RBC} in Figure 6.4, because RBC is the non-Newtonian component in the two-phase flow. Flow regions with many RBCs therefore show strong non-Newtonian behaviour compared to RBC-depleted regions.

The larger viscosities of the non-Newtonian flows result in larger viscous dissipation than for pure water. This implies that more kinetic energy is present in the recirculation zone so it is at its largest for the Newtonian single-phase flow. Since the vortex is depleted of RBCs its viscosity is smaller for the multiphase flow than for the non-Newtonian single-phase flow. This explains why L is slightly larger for the multiphase flow. The difference is very small due to the small hematocrit of 1 %.

The z-velocity profile is extracted for all cases along the line PQ through the centre of the vortex which is described by $Z = Z_0$ and $X = 0$ m (see Figures 6.2a and 6.3a). These velocity profiles, the 2D FD streamfunctions, the experimental and the computational results are displayed in Figure 6.5. The present velocity profiles are more in conformity with the experimental results and the computed stream functions than with the CFD results of Jung and Hassanein (2008). This is best visible in the close-up for $Re = 37.8$ (Figure 6.5d). The Newtonian fluid matches best with the stream functions, probably because the influence of the RBCs on the fluid behaviour is overestimated in the Carreau-Yasuda model for such a small hematocrit since the model parameters are fit for $0.30 < \varepsilon_{RBC} < 0.70$.

Table 6.2: Properties of the recirculation zone for two *Re*.

Re	H	Variable	Multiphase Karino (1967) experiment	Multiphase Jung (2008) simulation	Multiphase Present	Single-phase Carreau-Yasuda	Single-phase Newton
12.2	0.01	L (μm)	230	220	203	196	222
		Z_0 (μm)			-78	-78	-86
		Y_0 (μm)			-160	-161	-159
37.8	0.01	L (μm)	715	620	581	577	656
		Z_0 (μm)			-192	-189	-209
		Y_0 (μm)			-149	-150	-149

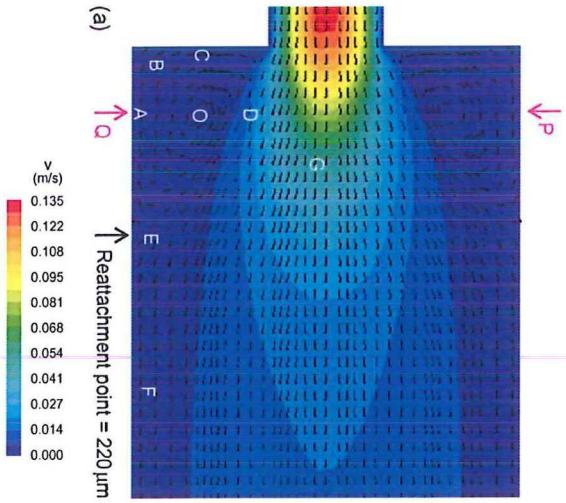

(a) Re = 12.2, multiphase Jung and Hassanein (2008)

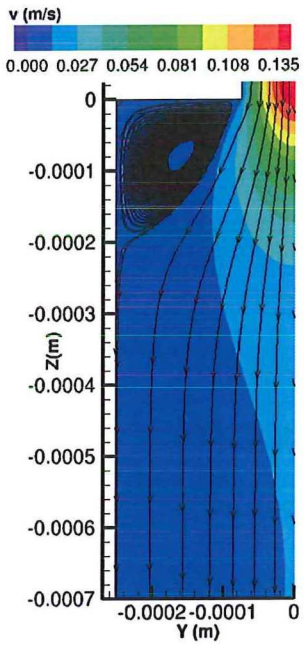

(b) Re = 12.2, multiphase present

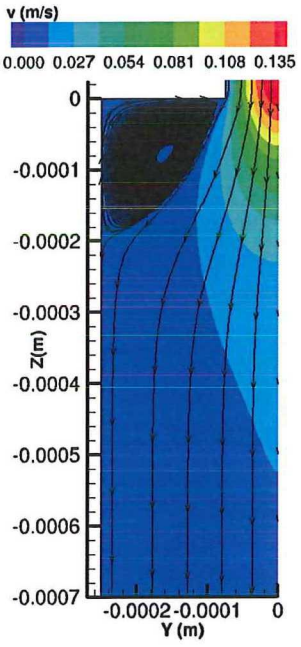

(c) Re = 12.2, Single-phase Carreau-Yasuda model

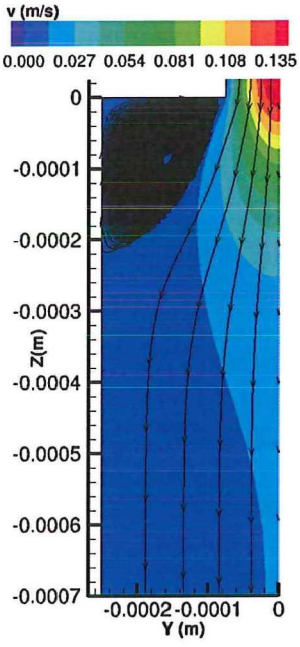

(d) Re = 12.2, Single-phase Newtonian model

Figure 6.2: Velocity magnitude contours and streamtraces for multiphase flows with a hematocrit of 1 % for Re 12.2 at plane X = 0m. The velocity profiles that are extracted along the line PQ through the vortex centre and are displayed in Figure 6.5.

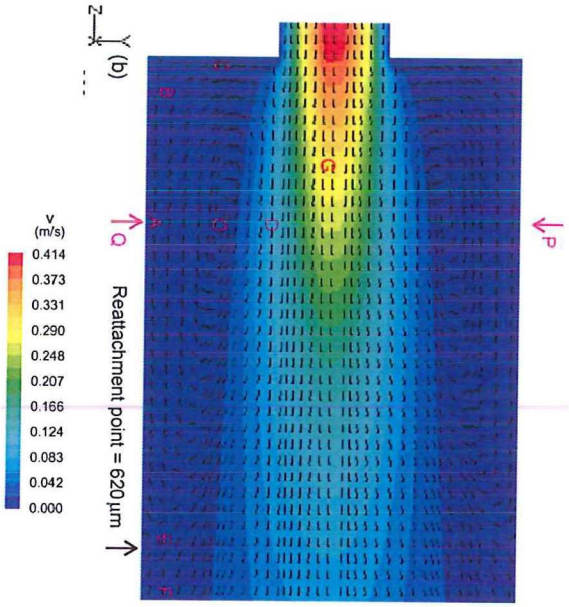

(a) Re = 37.8, multiphase Jung and Hassanein (2008)

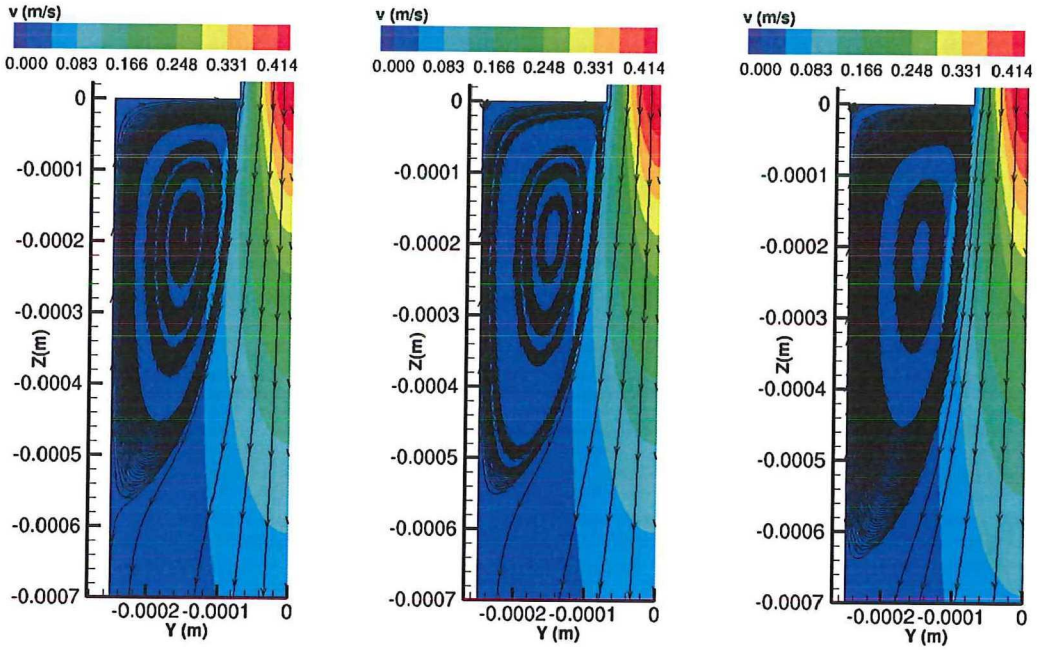

(b) Re = 37.8, multiphase present

(c) Re = 37.8, single-phase Carreau-Yasuda model

(d) Re = 37.8, single-phase, Newtonian model

Figure 6.3: Velocity magnitude contours and streamtraces for multiphase flows with a hematocrit of 1 % for Re 37.8 at plane X = 0m. The velocity profiles that are extracted along the line PQ through the vortex centre and are displayed in Figure 6.5.

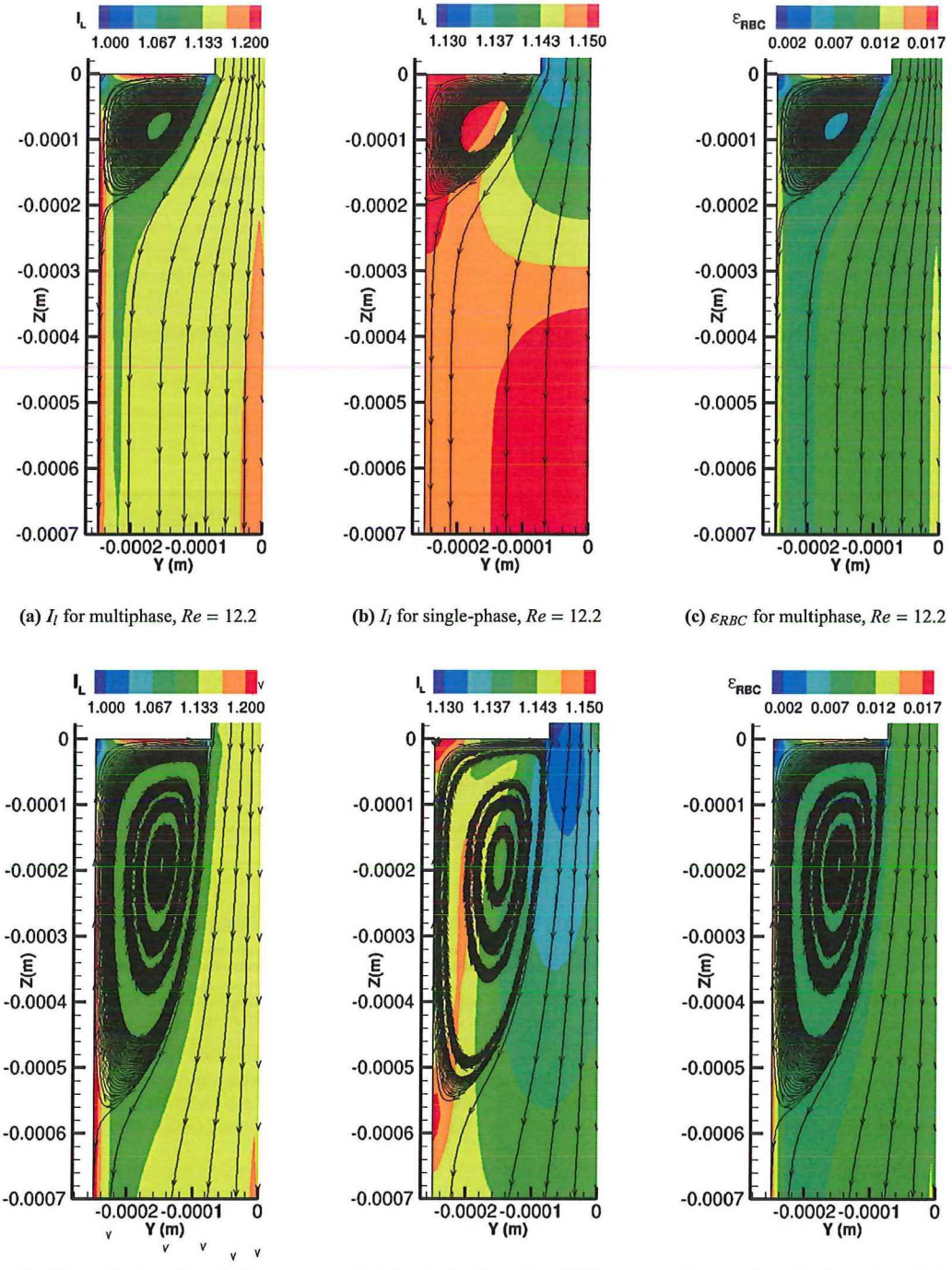

(a) I_l for multiphase, $Re = 12.2$ (b) I_l for single-phase, $Re = 12.2$ (c) ε_{RBC} for multiphase, $Re = 12.2$

(d) I_l for multiphase, $Re = 37.8$ (e) I_l for single-phase, $Re = 37.8$ (f) ε_{RBC} for multiphase, $Re = 37.8$

Figure 6.4: Contour plots of local non-Newtonian importance factor and the RBC volume fraction for two Re for single-phase and multiphase simulations with the same Carreau-Yasuda viscosity model. Initially $\varepsilon = 0.01$.

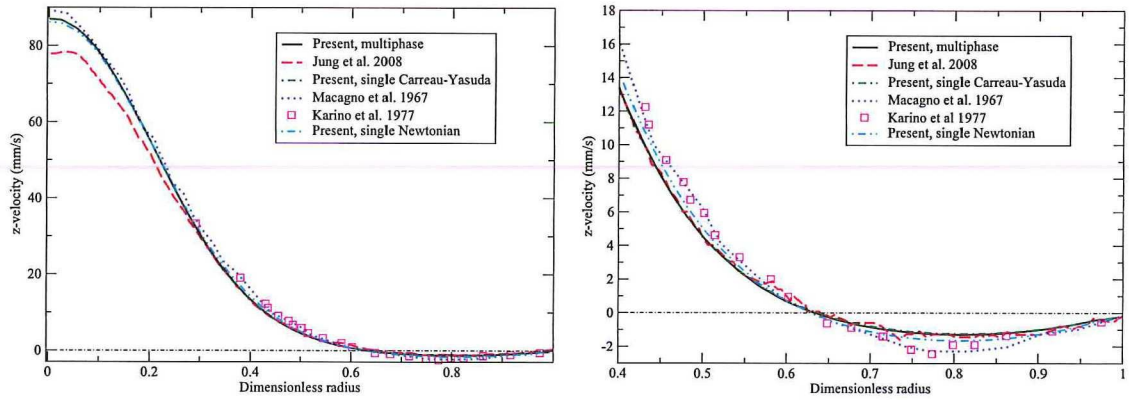

(a) Re 12.2

(b) Re 12.2 zoom in

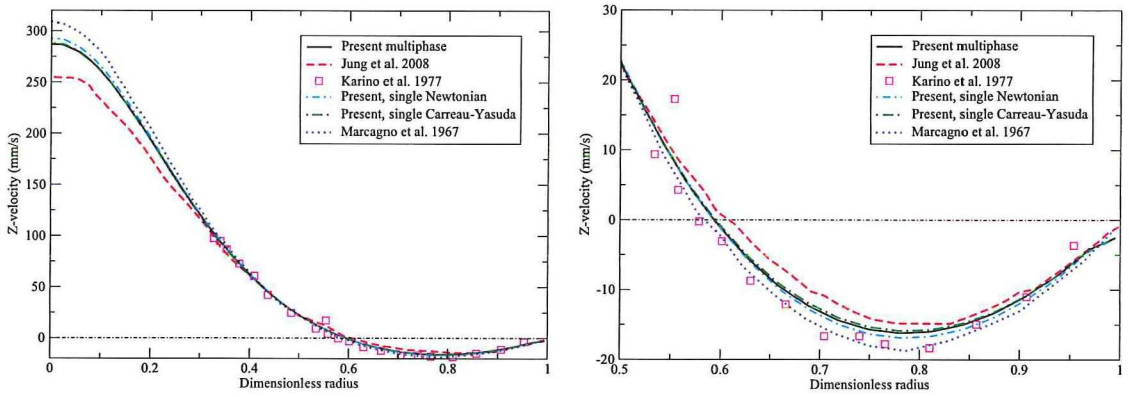

(c) Re 37.8

(d) Re 37.8 zoom in

Figure 6.5: Z-velocity extracted along the line x=0 m through the vortex centre for Re 12.2 and Re 37.8. The dimensionless radius is 0 at the centre of the tube and 1 at the wall. The right graphs are close ups of graphs in the left column. The present data are compared with 2D FD streamfunctions (Karino and Goldsmith, 1977), experiments (Macagno and Hung, 1967) and CFD results (Jung and Hassanein, 2008)

6.2 Hematocrit 0.45

The average human hematocrit is 0.45 so this value is selected for the second set of simulations. Karino and Goldsmith (1977) carried out some qualitative studies on the concentration of RBCs in the recirculation zone. For $Re < 10$ the vortex was depleted of RBCs within thirty seconds and for $Re > 10$ an equilibrium concentration was established within the vortex. Jung and Hassanein (2008) performed simulations for several Re and examined the Wall Shear Stress (WSS) and ε_{RBC} distributions. The material properties, flow properties, boundary conditions and initial conditions are written down in Table 6.3. $\bar{\mu}_{mix}$ is computed first and then Re is determined.

Table 6.3: Settings for the multiphase flow in a suddenly expanding tube for the case with the initial hematocrit $\varepsilon_{RBC} = 0.45$. The Carreau-Yasuda viscosity model that is used is described in Equation 2.8 and Table 6.1. $\bar{\mu}_{mix}$ and Re are computed near the end of the small tube close to the expansion. $\bar{u}$ is set and $\bar{\mu}_{mix}$ and Re are computed subsequent, where $\bar{\mu}_{mix}$ is the volume fraction averaged viscosity.

Material properties	
Density	$\rho_{water} = 1020$ kg/m^3 $\rho_{RBC} = 1100$ kg/m^3 $\rho_{single-phase} = 1056$ kg/m^3
Viscosity	$\mu_{plasma} = 0.002$ Pa·s $\mu_{Newt} = 0.0037$ Pa·s
Particle diameter	$d_p = 8.2\mu$m
Flow properties	
$\bar{u}$, $\bar{\mu}_{mix}$ and Re according to Eq 6.1	$\bar{u} = 0.11$ m/s $\bar{\mu}_{mix} = 0.00425$ Pa·s, $Re = 4.1$ $\bar{u} = 0.70$ m/s $\bar{\mu}_{mix} = 0.0027$ Pa·s, $Re = 41.2$
Boundary conditions	
Inlet volume fraction	$\varepsilon_{RBC} = 0.45$
Inlet velocity	parabolic profile
Wall velocity	zero slip velocity for all phases
Outflow	zero gradient
Initialization	
Volume fraction	$\varepsilon_{RBC} = 0.45$
Velocities	$\mathbf{u} = \mathbf{0}$ m/s

6.2.1 Results $Re = 4.1$

In Figure 6.6 the RBC volume fraction and the flow field for $Re = 4.1$ for single-phase and multiphase flows are shown at the plane $x = 0$ m. A similar flow field and recirculation zone is observed in the present stream traces and in the vector fields of Jung and Hassanein (2008). A larger region of small ε_{RBC} is found near the recirculation zone in the present study. This is in conformity with the experimental study of Karino and Goldsmith (1977) who observed that the recirculation zone is depleted for $Re < 10$. Just as for $\varepsilon = 0.01$ it is observed that the recirculation length is largest for the single-phase Newtonian flow.

ε_{RBC} and WSS at the expansion ($z = 0$ m) are shown in Figure 6.7. The area of the inner tube is empty because there is no wall neither WSS. A larger region with a very small ε_{RBC} is observed than in Jung and Hassanein (2008), just like in Figure 6.6b. Since the WSS is proportional to the viscosity it is also smaller in that region, as observed in Figure 6.7d. The WSS is discussed more extensively later on.

The non-Newtonian importance factor (Equation 6.2) is displayed for the single-phase C-Y model and the multiphase flow in Figure 6.8 at the plane $x = 0$ m. The difference between both viscosity distributions is the largest in the recirculation zone where ε deviates the most from 0.45. The large viscosity downstream at the flow centre is due to the small velocity gradient at the top of the parabolic-like profile. This coincides with a very low strain rate at which μ_{C-Y} is large (See Table 6.1 for the expression of μ_{C-Y})

A parameter of interest in vascular diseases is the WSS, which depends on the velocity gradient and the viscosity (see Equation 2.1). The WSS and the partial velocity derivative dv/dz are displayed in Figure 6.9. dv/dz is representative for $du_{\parallel}/dn$ at the line $x = 0$ m because $du/dz = 0$ because of symmetry.

The single-phase C-Y model results in a smaller WSS than the multiphase model. The overestimation of the RBC volume fraction with $\varepsilon_{RBC} = 0.45$ does not balance the smaller velocity gradient, so the WSS due to the multiphase flow is larger. The effect of the smaller viscosity of the Newtonian flow on the WSS is exceeded by the larger velocity gradient, which leads to the largest WSS for the Newtonian flow.

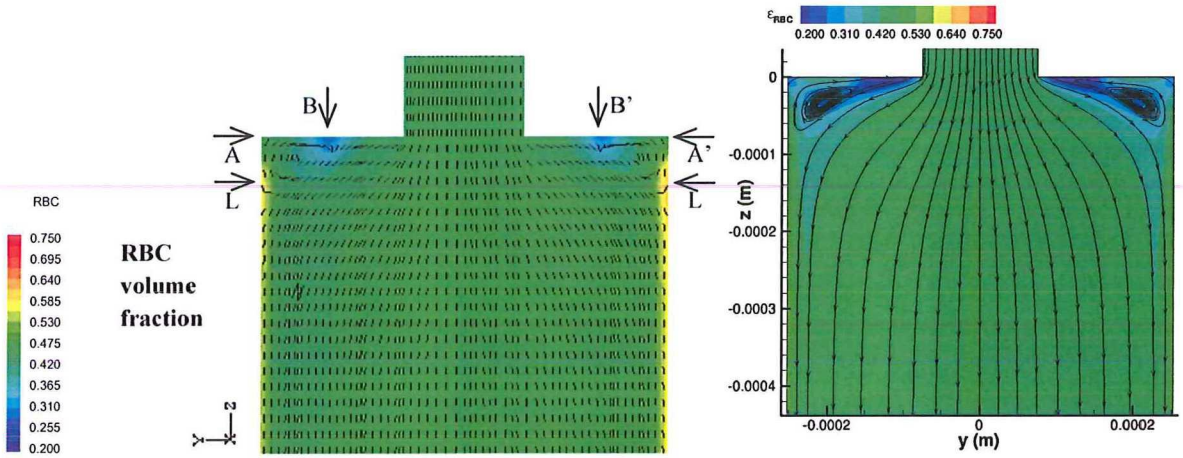

(a) RBC volume fraction multiphase Jung and Hassanein (2008)

(b) RBC volume fraction present multiphase

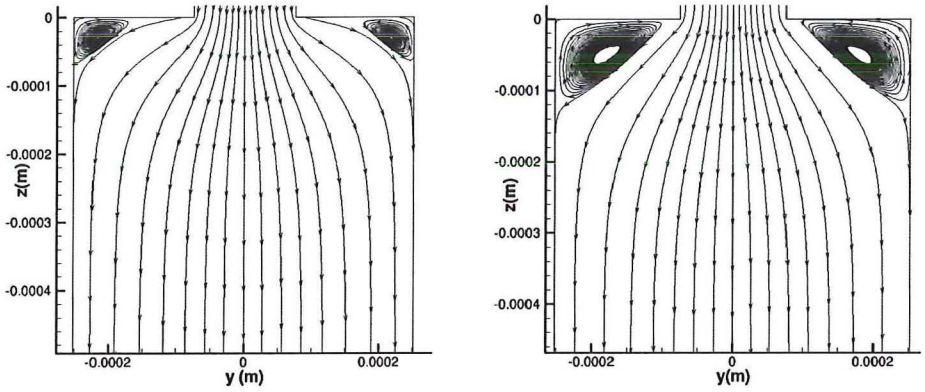

(c) Streamtraces present single-phase C-Y

(d) Streamtraces present single-phase $\mu = 0.0037$Pa·s

Figure 6.6: RBC volume fraction and stream traces in a suddenly expanding tube. The initial hematocrit is 45 % and $Re = 4.1$.

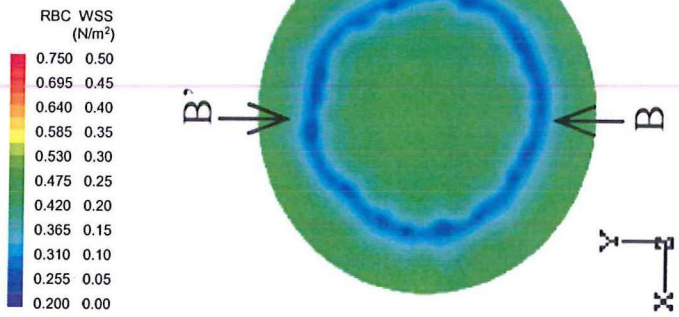

(a) Legends Jung

(b) RBC volume fraction and WSS at z=0 m from multiphase simulations Jung and Hassanein (2008)

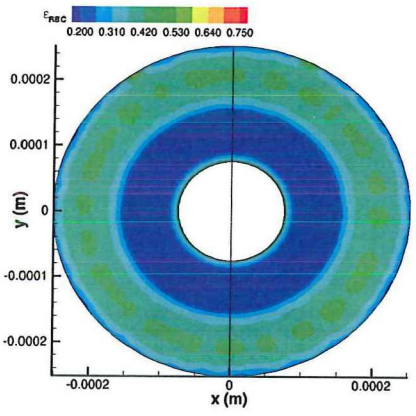

(c) RBC volume fraction at z=0 m m

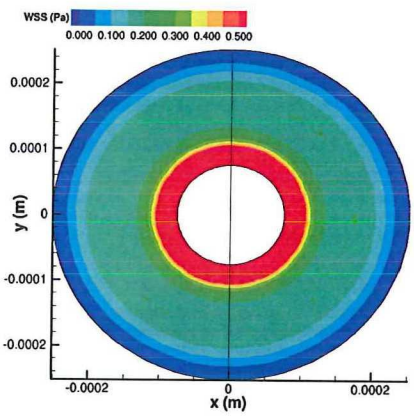

(d) WSS at z=0 m; Multiphase C-Y

Figure 6.7: RBC volume fraction and total WSS for multiphase flows in a suddenly expanding tube at z=0 m. The initial hematocrit is 45 % and Re=4.1. The crosssections shown in other figures are extracted at $x = 0$ m which is indicated by BB'.

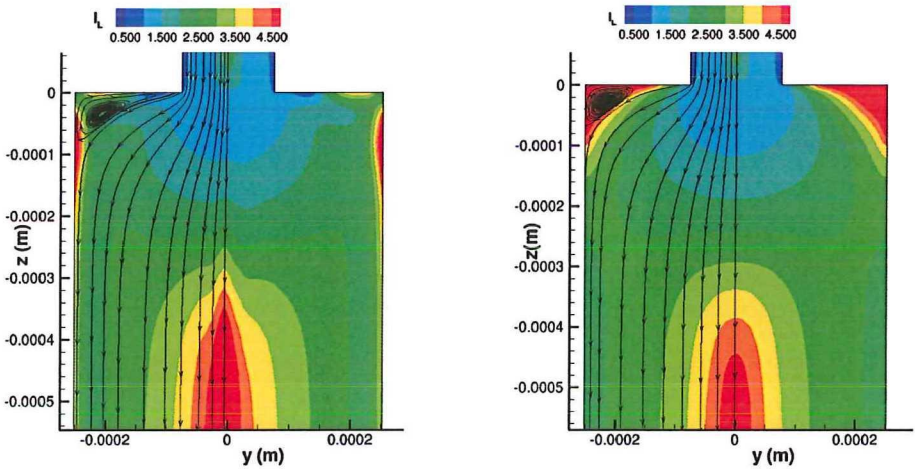

(a) Non-Newtonian importance factor multiphase flow, $Re = 4.1$

(b) Non-Newtonian importance factor single-phase C-Y, $Re = 4.1$

Figure 6.8: Contour plots for the non-Newtonian importance factor with $\mu_N = 0.0037$Pa·s for multiphase and single-phase flow. The initial hematocrit is 45 % and $Re = 4.1$.

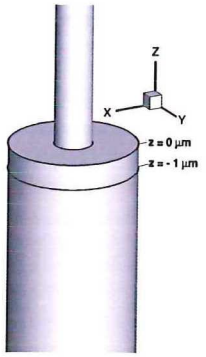

(a) Planes $z = 0\mu$m and $z = -1\mu$m, not to scale.

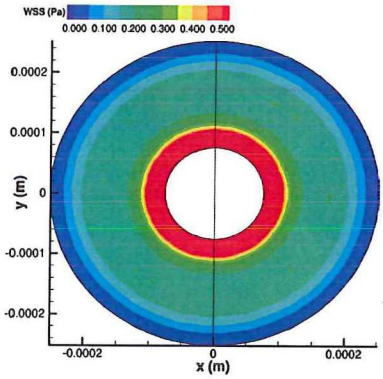

(b) WSS at z=0 m; Multiphase C-Y

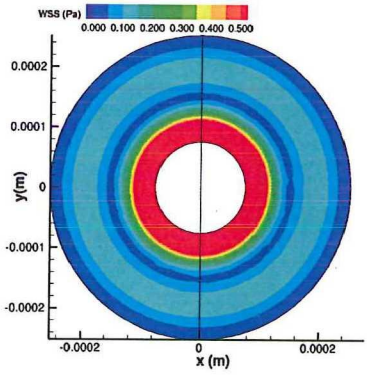

(c) WSS at z=0 m; Single-phase C-Y

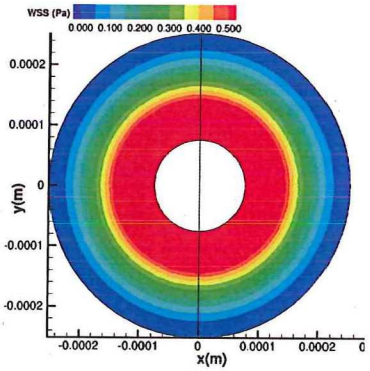

(d) WSS at z=0 m; Single-phase μ = 0.0037Pa·s

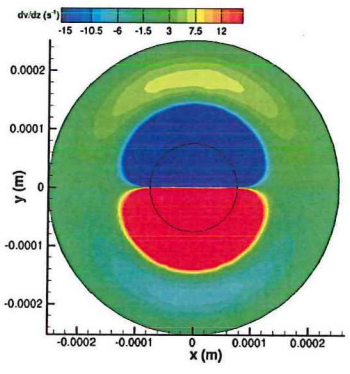

(e) dv/dz at $z = -1\mu$m; Multiphase

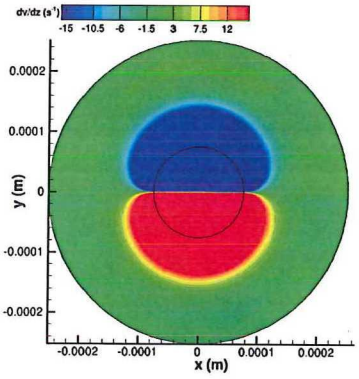

(f) dv/dz at $z = -1\mu$m; Single-phase C-Y

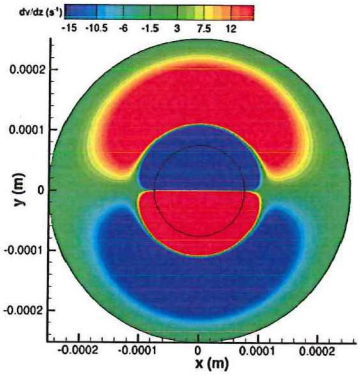

(g) dv/dz at $z = -1\mu$m; Single-phase μ = 0.0037Pa·s

Figure 6.9: Contour plots of the WSS and velocity gradient dv/dz for multiphase and single-phase flows with hematocrit 0.45 and $Re = 4.1$. $|dv/dz|$ equals the magnitude of the total velocity gradient normal to the wall at the line $x = 0$ m.

6.2.2 Results $Re = 41.2$

Karino and Goldsmith (1977) measured an equilibrium concentration in the recirculation zone in their qualitative study with whole blood for $Re > 10$. $\bar{u}$ is increased from 0.11 m/s to 0.7 m/s at the inlet which resulted in a reduced $\bar{\mu}_{mix}$ at the end of the small tube from 0.00425 Pa·s to 0.0027 Pa·s.Re at the end of the inlet tube is increased from 4.1 to 41.2. The reduced $\bar{\mu}_{mix}$ is in agreement with the Carreau-Yasuda viscosity model since a larger velocity results in larger strain rates which reduces the viscosity.

Contours of the z-velocity and streamtraces are shown in Figure 6.10, where z is defined positively in the upward direction. The z-velocity is largest for the single-phase Newtonian simulation due to less viscous dissipation. The non-Newtonian importance factor (Equation 6.2) with $\mu_N = 0.0037$Pa·s and the RBC volume fraction are shown in Figure 6.11 for the multiphase and the non-Newtonian single-phase simulations. I_L slightly differs in a few regions: in the upper corner of the outer tube, at the centre of the vortex, at the wall just downstream the vortex and at the centre of the downstream flow. The regions with $\varepsilon_{RBC} > 0.45$ indeed show a larger viscosity than predicted by the single-phase simulation and a smaller viscosity is shown for $\varepsilon_{RBC} < 0.45$. The smaller ε_{RBC} in the vortex centre for the multiphase simulation results in the slightly larger z-velocity observed in Figure 6.10.

A small secondary vortex appears at the corner of the expansion, which is also observed by Karino and Goldsmith (1977) for $Re > 10$. The length of this vortex L_s and the distance of the reattachment point from the expansion L are presented in Table 6.4 for the three different blood-flow models. The Newtonian simulation shows again the largest L and the single-phase non-Newtonian the shortest. The higher velocity of the primary vortex of the Newtonian fluid results in a larger inertial force on the secondary vortex in the upward direction, which leads to a smaller secondary vortex than in the multiphase simulation.

Jung and Hassanein (2008) observed a larger recirculation length of 785μm for a similar multiphase simulation. A constant inlet velocity of 0.7 m/s is used in their simulations as opposed to the parabolic profile that is applied in the present study, but $\bar{u}_{in}$ is the same. The length of the inlet tube is unknown so it is possible that the flow is not fully developed at the expansion. Two additional equations are implemented in Jung and Hassanein (2008) to account for the smaller driving force at low strain rates due to the RBC agglomeration (see Appendix C). These differences could lead to a larger L but the exact influence of these additional equations are unknown so this could be examined in future work for a fair comparing.

Table 6.4: Recirculation lengths of the primary vortex (L) and the secondary vortex (L_s) for $\varepsilon_{RBC} = 0.45$ and $Re = 41.2$ for the three different blood-flow models.

Present, $Re = 41.2$	Multiphase	Single-phase Carreau-Yasuda	Single-phase Newton
L (μm)	523	515	562
L_s (μm)	27	7.5	12

3D WSS profiles are visualized in Figure 6.12 and the WSS at the plane $z = 0$ m is similar for all three models. Two bands of low WSS, one at the wall of the outer tube at the expansion and one at the reattachment zone, are in accordance with Jung and Hassanein (2008). The bands of low WSS near the reattachment point are different for the three models where the Newtonian flow induces the largest band. The small velocity near the reattachment point results in a small strain rate and a large value of the Carreau-Yasuda viscosity, just as could be concluded from the non-Newtonian importance factor in Figure 6.11. $I_L \approx 3$ slightly downstream the reattachment point so the WSS for the non-Newtonian flows increases faster than for the Newtonian flow. The single-phase C-Y flow induces a smaller WSS at the reattachment point than the multiphase flow due to an accumulation of RBCs at the wall.

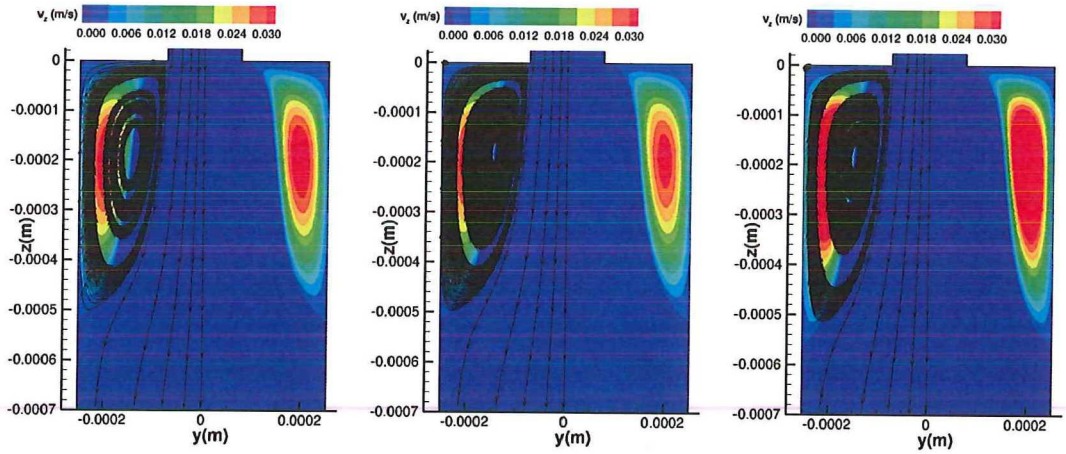

(a) Z-velocity multiphase flow (b) Z-velocity single-phase C-Y flow (c) Z-velocity single-phase Newtonian flow

Figure 6.10: Z-velocity and stream traces at the plane $x = 0$ m for $Re = 41.2$ and initial hematocrit 0.45. $\mu_N = 0.0037$Pa·s. The recirculation lengths are 523μm, 515μm and 562μm for the multiphase, single-phase C-Y and single-Phase N respectively.

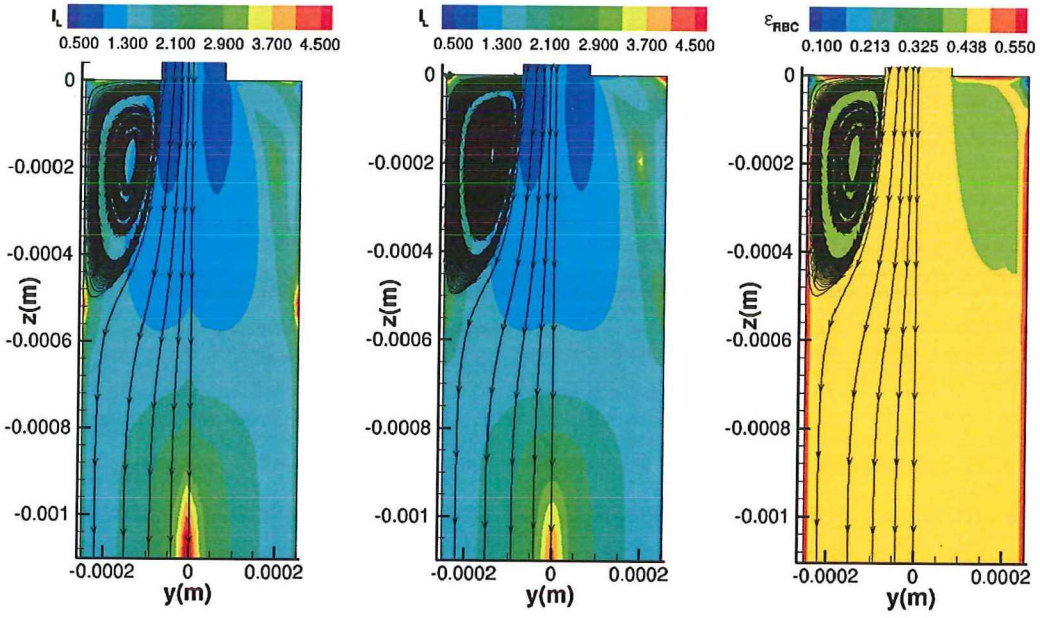

(a) Non-Newtonian importance factor multiphase flow (b) Non-Newtonian importance factor single-phase C-Y (c) Volume fraction RBCs multiphase flow

Figure 6.11: Non-Newtonian importance factor with $\mu_N = 0.0037$Pa·s. The initial hematocrit is 45 % and $Re = 41.2$.

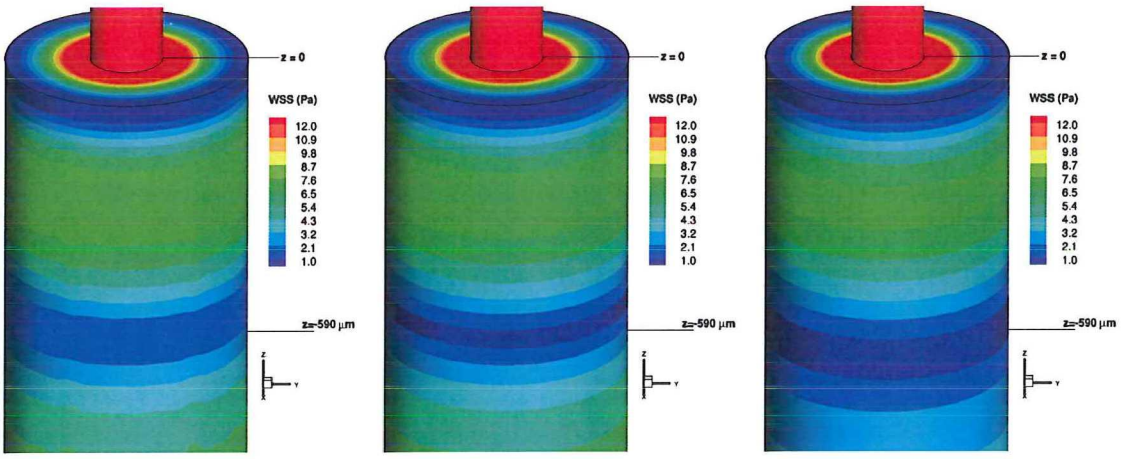

(a) WSS multiphase flow

(b) WSS single-phase flow C-Y

(c) WSS single-phase flow with μ = 0.0037Pa·s

Figure 6.12: Contour plots of the WSS for Re = 41.2. The WSS for the multiphase flow is computed by volume fraction averaging. The recirculation lengths are 523μm, 515μm and 562μm for the multiphase, single-phase C-Y and single-Phase N respectively.

6.3 Conclusion suddenly expanding tube from 151μm to 504μm diameter

The addition of 1 vol-% of hardened Red Blood Cells (RBCs) to pure water is observed to influence the recirculation length and the viscosity for Re = 12.2 and Re = 37.8. The longest recirculation length is observed for a single-phase Newtonian flow (μ =0.0037 Pa·s), while the recirculation lengths for the single-phase flow and the multiphase flow with the Carreau-Yasuda viscosity model were similar. The observed recirculation lengths are close to the experiments from Karino and Goldsmith (1977) and the simulations from Jung and Hassanein (2008). The maximum increment of the viscosity due to the C-Y model is about 20 % for the multiphase and 15 % for the single-phase simulations for both Re, which is quite high for only 1% RBCs.

Then the RBC volume fraction is increased to the realistic value of 0.45 and simulations are performed with Re = 4.1 and Re = 42.1. The same influence on the recirculation length is observed in that the Newtonian fluid results in the largest and the single-phase Carreau-Yasuda in the smallest length. The maximum viscosity that is observed is 4.5 times larger than the Newtonian viscosity. For the multiphase flow the recirculation zone contains less RBCs which leads to a smaller viscosity in the vortex than for the non-Newtonian single-phase simulations. An accumulation of RBCs is perceived at the wall next to and after the recirculation zone.

For Re = 4.1 there is a significant difference in WSS at the expansion (at z=0 m) between the three models, while this difference is not present for Re = 42.1. For this latter Re the main influence on the WSS is observed at the reattachment point.

The overall conclusion on a suddenly expanding tube of some hundreds of μm is that the prediction of the recirculation zone requires a single-phase non-Newtonian viscosity model. The differences between the single-phase and the multiphase non-Newtonian model are too small compared to the additional computational time that is required to resolve two phases.

CHAPTER 7

Meshing a real patient's carotid artery

The previous chapters provide the results of single-phase and multiphase Carreau-Yasuda viscosity models in idealized arteries. These results are compared to the results of a single-phase Newtonian flow. It is observed to be necessary to use a single-phase non-Newtonian approach when a recirculation zone or a 180° curvature is present. The coming chapters elaborate on blood flow through a bifurcating carotid artery from a real patient. In this chapter the process from the geometry file is traced from its creation to the completed computational grid. Chapter 8 presents the results of a single-phase Newtonian flow through this carotid artery for six different grid cell-types. Subsequently single-phase and multiphase flows with the Carreau-Yasuda viscosity model are computed and these results are presented in Chapter 9.

7.1 Preparation of the geometry

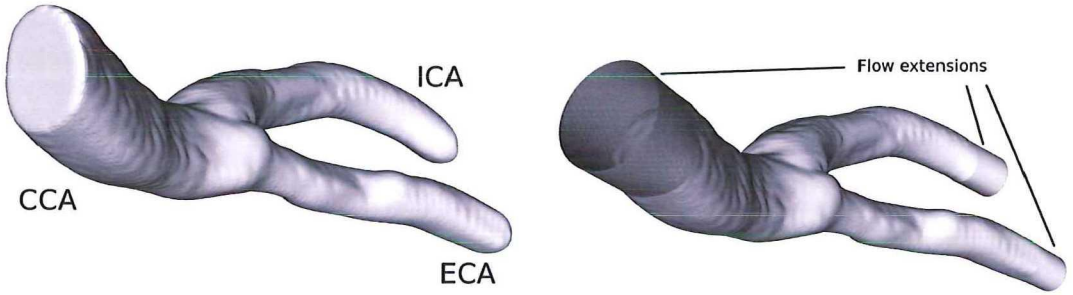

(a) Original Carotid Artery from CT scan

(b) Modified Carotid Artery with extensions at the inlet and outlets

Figure 7.1: Healthy Carotid Artery obtained from CT scan before and after preparing it for the CFD simulations by providing it with oval flow extensions at the inlet and outlets. The inlet blood vessel is the Central Carotid Artery (CCA) and the outlets are the Internal Carotid Artery (ICA) and the External Carotid Artery (ECA).

The geometry of the left carotid artery that is shown in Figure 7.1a is obtained by a CT (Computed Tomography) scan by Gijssen (2010) from the Erasmus Medical Center in Rotterdam. The inlet and outlets of the geometry are modified before the geometry is imported into one of the meshing-programs Gambit or Icem CFD. The original file contains rounded end-caps at the outlets and at the inlet which are clipped to allow for straightforward and reliable implementation of a parabolic velocity inlet profile. This clipping is performed by de Loor (2011) using the Vascular Modeling Toolkit (VMTK). Since the vascular system is a closed system, the flow has no development region. Therefore the second modification of the geometry is to extend the inlet and outlets to avoid entrance effects and exit effects. The elliptically shaped extensions are also created in the VMTK and the final geometry is presented in Figure 7.1b.

7.2 Meshing

The CFD method is based on dividing the geometry in small volumes and solving the conservation equations for each control volume or cell (see Chapter 4). There are three standard cell types - hexahedrals, tetrahedrals and

polyhedrals - and two meshing methods: structured and unstructured meshing. A structured mesh contains repeating patterns that are aligned with the main flow direction. An unstructured mesh is a collection of equally sized cells and no reoccurring pattern or preferred direction are observed. An additional meshing option is that boundary layers can be added to resolve the flow near the wall in more detail. These layers of smaller cells could consist of the same cell types as the main part of the mesh, but a boundary layer of hexagonal cells surrounding a polyhedral or tetrahedral mesh is also a frequently used meshing method. In the present project there is chosen to have one cell type per mesh to reduce numerical diffusion due to the transition between the boundary layer and the rest of the grid.

The CA is meshed with five different mesh types by de Loor (2011): hexagonal and tetrahedral meshes with and without a boundary layer and polyhedral meshes without a boundary layer. This set is complemented with polyhedral meshes with boundary layers in the present research. The six mesh types are shown in Figure 7.2. At least three meshes with different cell densities are created for each cell type. The meshes are systematically refined, that is that the same refinement factor is applied in each direction. The ratio of a characteristic cell size of two successive meshes is at least 1.3 as is required for the error analysis (see Section 4.2.1). An overview of the grid sizes is given in Table 7.1.

Each mesh type is created in a different meshing program. The tetrahedral meshes are created in Gambit which only prompts the number of cells at the edges of the inlet and the outlets. Then the inlet face and outlet faces are meshed with triangles having similar areas and subsequently the wall of the artery is meshed using similar homogeneous triangles. Finally the artery is meshed with tetrahedrals that all have approximately the same volume. The advantage of a tetrahedral grid is that its creation is automatically after you specify the cell size. However, the cell density is large due to the homogeneity since the minimum cell density is determined by the region with the largest gradient where the cells have to be small enough to resolve it. The tetrahedral grids with boundary layer are created using the 'size function' in Gambit which prompts the start-size of the cell, the growth rate and the number of layers. The rest of the meshing procedure is similar to that of the tetrahedral meshes without boundary layer.

One very dense tetrahedral mesh is created to serve as a reference solution. This mesh consists of 7.5 million cells and it does not contain a boundary layer.

The polyhedral grids are based on the tetrahedral grids. Fluent is used to convert tetrahedral grids - created in Gambit - to polyhedral grids by merging about five or six cells and removing the faces and nodes that are at the inside of the new cells. The resulting polyhedral grid consists of about five times fewer cells than the original tetrahedral grid and it contains the same regularities and irregularities. Due to the scope of his project de Loor (2011) did not convert tetrahedral grids that contain a boundary layer into polyhedral grids, so this is done in this project. Both tetrahedral and polyhedral meshes are unstructured meshes.

New structured hexahedral meshes are constructed in Icem CFD for the present research to obtain a wider range of cell densities than de Loor (2011) which is required for the error analysis (ASME, 2008). The meshing for the structured hexahedral grids starts with dividing the carotid artery into blocks which edges and faces are linked to the geometry. This blocking is also known as the topology and it determines the distribution of the cells over the geometry. The topology of the finest hexahedral mesh (1.2 million cells) is displayed in Figure 7.3. The blocking for hexahedral meshes with boundary layer has the same structure as in Figure 7.3, but an additional sequence block is created in the centre of the artery. The extra layer of blocks determines the space for the boundary layer. An amount of cells is assigned to each block, not to the geometry, depending on its volume. The cells are then arranged to represent the geometry by deforming and rearranging them, based on the linked edges, linked faces and the distance between the blocking and the geometry. Many blocks are required to mesh the bifurcating CA due to the curvature and the bifurcation.

The conclusion on meshing is twofold. The tetrahedral and polyhedral meshing procedure could be automated which is a great advantage since each patient's artery has to be meshed separately. However, properly designed hexahedral grids could have local refinements near the bifurcation and a smaller density in more straightforward

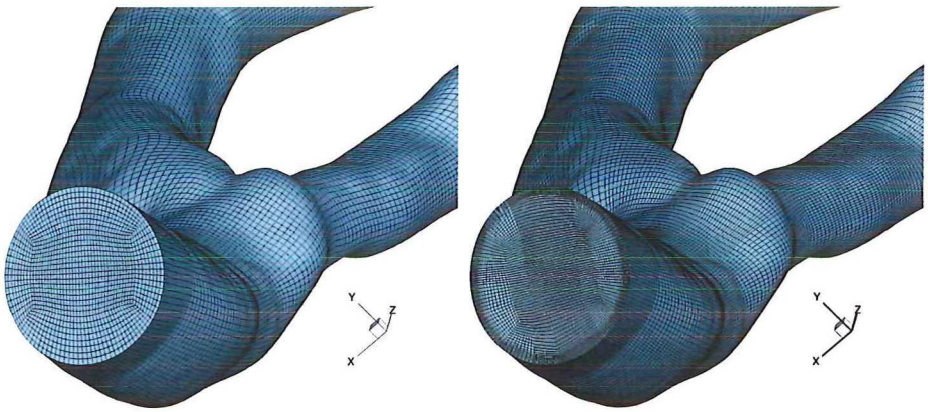

(a) Hexagonal mesh

(b) Hexagonal mesh bl

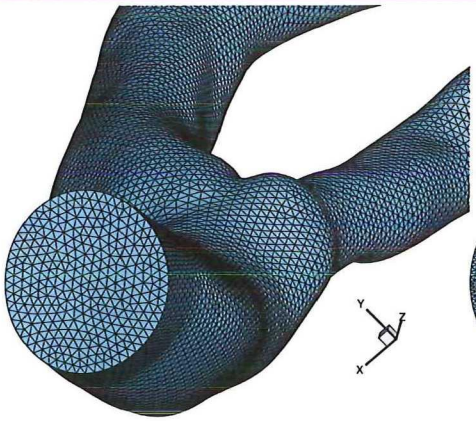

(c) Tetrahedral mesh

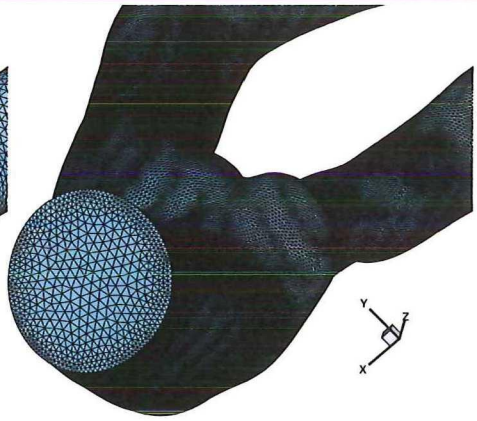

(d) Tetrahedral mesh bl

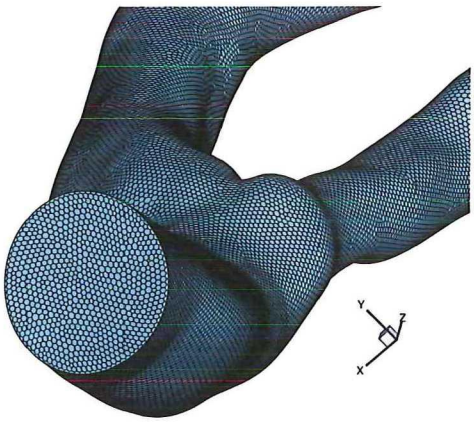

(e) Polyhedral mesh

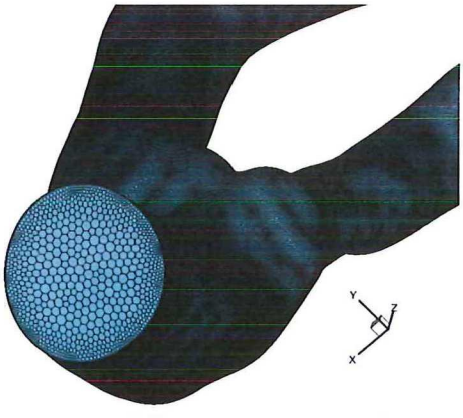

(f) Polyhedral mesh bl

Figure 7.2: Contours of the inlet of the six different mesh types.

regions due to the better control on the meshing procedure. This could lead to the smallest computational time for hexahedral cells.

Table 7.1: Overview of the meshes that are created for each mesh type. The solution obtained with the tetrahedral mesh with over seven million cells (printed in bold font) is taken as reference solution.

Mesh type	# cells	Mesh type	# cells
Hexagonal	259,072	Hexagonal b.l.	189,332
	559,530		497,340
	1,234,168		1,110,528
Tetrahedral	204,052	Tetrahedral b.l.	
	419,104		497,681
	821,771		1,678,386
	1,632,416		3,609,451
	7,569,213		
Polyhedral	156,717	Polyhedral b.l.	97,558
			317,630
	511,956		677,540
	1,338,638		1,273,135

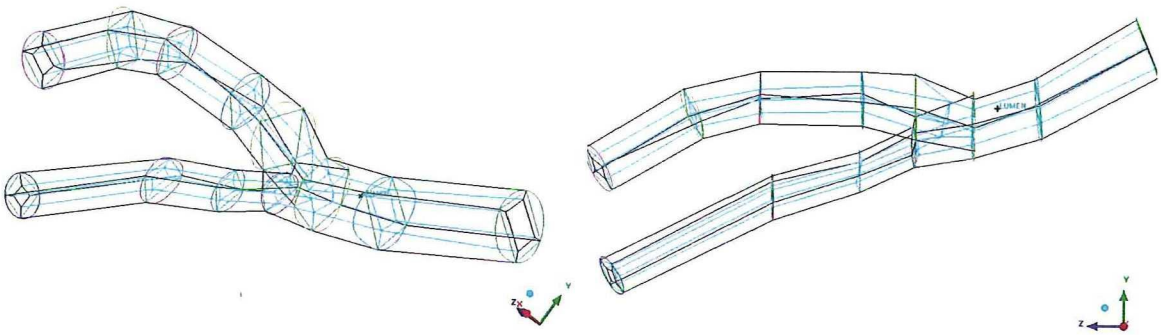

Figure 7.3: Blocking for hexahedral mesh with 1.2 million cells, seen from two different perspectives. The black lines represent the blocks at the outside of the geometry. The light blue lines are the edges connecting the inner blocks. The colored curves are part of the geometry used to fix the blocks to the vessel wall.

7.3 Mesh quality assessment

The quality of a mesh can be expressed in terms of skewness (SK) and aspect ratio (AR) (Spiegel et al., 2011). Skewness is the deviation of cell faces from its ideal shape and the definition varies per cell type. The definition for the Equisized Angle Skewness is similar for all meshes, but the equisize angle differs per mesh type (Fluent, 2002):

$$\mathrm{SK} = \max\left[\frac{\alpha_{max} - \alpha_{eq}}{180° - \alpha_{eq}}, \frac{\alpha_{eq} - \alpha_{min}}{\alpha_{eq}}\right] \tag{7.1}$$

α_{max} is the maximum angle between two edges and α_{min} the minimum angle. The equisize angle α_{eq} for hexahedral and tetrahedral meshes is given by:

$$\alpha_{eq,hex} = 90° \quad (7.2)$$

$$\alpha_{eq,tet} = 60° \quad (7.3)$$

The aspect ratio is a measure for the difference in edge length in a cell. The definitions for hexahedral and tetrahedral cells are:

$$\mathrm{AR}_{hex} = \frac{\max(e_1, e_2, e_3)}{\min(e_1, e_2, e_3)} \quad (7.4)$$

$$\mathrm{AR}_{tet} = \frac{1}{3}\frac{R}{r} \quad (7.5)$$

Here e_i is the average length of the edge in direction i which is illustrated for a 2D cell in Figure 7.4. $AR = 1$ describes an equilateral element. For tetrahedral elements it holds that r is the radius of a sphere that inscribes the cell and R is the radius of the sphere that circumscribes the cell. Fluent (2002) provides an indication that $SK < 0.5$ indicates that the mesh is well designed and that $SK < 0.75$ is still acceptable. The global values of these quality parameters are presented in Table 7.2 and 7.3 for the meshes without and with boundary layer respectively. This indicates that the mesh quality is fine regarding the SK. The AR is the largest for meshes that include a boundary layer since the boundary layer consists of more flattened cells.

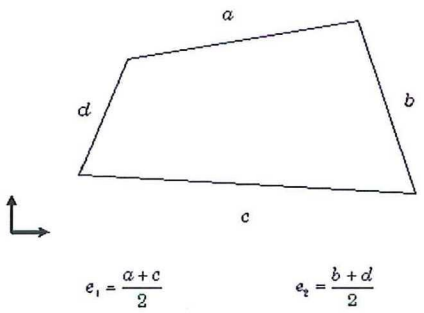

Figure 7.4: Illustration of the mean edge length used in the calculation of the aspect ratio. (Fluent, 2002)

Table 7.2: Aspect ratio and Skewness to address the quality of the grids. 85 % of the cells has a SK or AR below the upper boundaries that are provided. * The quality indicators provided for the polyhedral meshes are obtained from the original tetrahedral meshes.

Number of cells			AR (surface| mesh)						SK (surface| mesh)					
Tet.	Pol.	Hex.	Tet.		Pol.*		Hex.		Tet.		Pol.*		Hex.	
204,052	156,717	259,072	1.02	1.4	1.02	1.4	1.7	3.3	0.11	0.45	0.11	0.46	0.23	0.35
419,104	511,956	559,530	1.02	1.4	1.02	1.39	1.6	3.3	0.11	0.46	0.1	0.46	0.22	0.35
821,771	-	-	1.02	1.4	-	-	-	-	0.11	0.46	-	-	-	-
1,632,416	1,338,638	1,234,168	-	-	1.02	1.4	1.7	3.2			0.15	0.46	0.25	0.35
3,352,832	-	-	-	-			-			-	-	-	-	-
7,569,213	-	-	1.02	1.4	-	-	-	-	0.15	0.46	-	-	-	-

7.4 Computational time

The mesh type and mesh quality could provide an indication of the computational time that is required to obtain a convergent solution (see Section 4.1.5 for more on convergent solutions). The computations using hexahedral

Table 7.3: Aspect ratio and Skewness to address the quality of the grids with boundary layer. 85 % of the cells has a SK or AR below the upper boundaries of that are provided. *The numbers provided for the polyhedral meshes are obtained from the original tetrahedral meshes.

Number of cells			AR surface | mesh						SK surface| mesh					
Tet.	Pol.	Hex.	Tet.		Pol.*		Hex.		Tet.		Pol.*		Hex.	
-	97,558	189,332	-	-	1.03	1.41	4	10	-	-	0.15	0.47	0.2	0.4
497,681	317,630	497,340	1.03	1.41	1.03	1.42	4	10	0.15	0.47	0.15	0.48	0.2	0.35
-	677,540	-	-	-	1.03	1.45	-	-	-	-	0.15	0.48	-	-
1,678,386	1,273,135	1,110,528	1.03	1.42	1.03	1.5	4	9	0.15	0.48	0.13	0.47	0.2	0.35
3,609,451	-	-	1.03	1.45	-	-	-	-	0.15	0.48	-	-	-	-

meshes are expected to converge fast because the cells are aligned with the main flow direction and the orientations of the faces are regular. Tetrahedral cells can be skewed less so the density of a tetrahedral mesh with the same resolution near the wall as in a hexahedral mesh is larger. This makes that more computational time is expected. A smaller density than for the tetrahedral mesh is required for a polyhedral mesh to get the same accuracy at the wall. Each polyhedral cell at the boundary of the domain shares exactly one face with the boundary. This is contrary to tetrahedral cells that could share a node, an edge or a face with the boundary. This implies that more cells have to be taken into account to calculate the boundary for tetrahedral meshes. Secondly the cell centres of the polyhedral cells that form the boundary layer are located at a more regular distance from the wall than in the tetrahedral case. These advantages imply that a smaller cell density and less computational time is required to get an accurate solution using a polyhedral mesh compared to the usage of a tetrahedral mesh.

The WSS and the interaction between blood components and the blood vessel wall are some of the parameters of interest regarding vascular diseases. The properties near the blood vessel can be resolved more accurately by adding a boundary layer. The transition between the boundary layer and the rest of the mesh should be well designed, because a sudden transition in cell size between adjacent cells could induce numerical diffusion. A second remark on boundary layers is that it has a large cell density which increases the computational time. This could be compensated by a smaller cell density at the centre of the blood vessel. When a mesh with boundary layer is designed properly, it could have fewer cells than the appropriate mesh without boundary layer and yet the flow properties could be resolved better.

CHAPTER 8

Newtonian flow in a real patient's Carotid Artery

Two criteria for choosing the most suitable mesh for medical usage are discussed in Chapter 7.4: the feasibility to automate the meshing procedure and the computational time. However, the main criterion of the model is to obtain reliable information on the flow patterns and the WSS distribution. In this chapter the results of the grid dependence analysis of the CFD simulations of a single-phase steady state Newtonian flow through the carotid artery are presented. The mean and local wall shear stress (WSS) is compared for the six different mesh types presented in Chapter 7. The results obtained using meshes with different cell densities are compared and the influence of a boundary layer is also examined. The local discretization error is computed according to the uncertainty estimation method for CFD simulations from Section 4.2.2.

8.1 Numerical setup

The choice of the most suitable grid type is based on single-phase Newtonian blood-flow through a real patient's carotid artery. The average human blood viscosity of 0.0037 Pa·s and the mean blood density of 1057 kg m^{-3} are used as fluid properties. A parabolic inlet velocity profile with u_{max} = 0.338 m/s is implemented as inlet boundary condition inducing a laminar flow with Re = 295 at the inlet. This is the mean inlet velocity of the carotid artery in the cardiac cycle. There are two possibilities for the inflow direction: parallel to the flow extension or perpendicular to the inlet plane. Ideally this would be the same direction. This is not the case and a flow parallel to the geometry extension is implemented to avoid an inlet flow that is impinging at the blood vessel wall, what would lead to high WSS and velocity profiles that are not following the geometry smoothly. The flow that is parallel to the wall is the most realistic one since our vascular system is a closed system, so the blood follows the blood vessel wall, as for a healthy vascular system.

A static pressure is defined at the outlets so that 60% of the blood flows from the CCA into the ICA in correspondence with the measurements of Groen et al. (2010). The applied pressures are 13325.86 Pa at the ECA and 13332.2 Pa at the ICA and the zero-gradient boundary condition is applied for the velocity at the outlets. The backflow direction normal to the outlet plane is specified at both outlets. The blood vessel is modelled as a rigid wall with no-slip velocity.

8.2 Mesh analysis on cell type

8.2.1 Weighted-area-averaged WSS

The weighted-area-averaged WSS is compared for a global comparison of the results on the six mesh types. The WSS is extracted from the results obtained with the second order upwind scheme for the momentum equation (see Chapter 4). The WSS is extracted along 70 slices with constant z-coordinate and a finite thickness as shown in Figure 8.1. The area of the circumference of the slice is taken as the weighting factor to calculate the mean WSS to provide with one value per mesh. Tables 8.1 and 8.2 show the area weighted average WSS for grids without and with a boundary layer respectively. The last two columns of both tables show the difference with the tetrahedral result for meshes with a comparable number of control volumes. The solution on the finest tetrahedral mesh with

over 7 million cells is taken as reference solution and its area weighted average WSS is 1.6296 Pa.

The tables show that the area weighted WSS is close to the reference solution for all tetrahedral and polyhedral meshes. The solutions deviate with roughly 4.5% for hexahedral meshes without a boundary layer and almost 10% with boundary layer. The high skewness of the boundary layer and the complexity of meshing the bifurcation with a structured mesh probably induce this large error for the hexahedral meshes with boundary layer. The simulations using polyhedral meshes slightly underestimate the weighted-area-averaged WSS. This global parameter provides an indication on the difference in the results obtained with the six mesh types. Local WSS profiles are examined to have more detailed information.

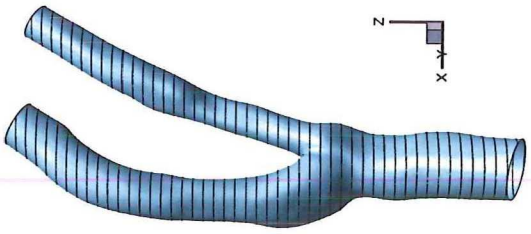

Figure 8.1: Example of slices with constant z-coordinate that are used to calculate the area-weighted-average WSS

Number of cells			Area-averaged WSS (Pa)			Difference in WSS (%)	
Tetrahedral	Polyhedral	Hexahedral	Tetrahedral	Polyhedral	Hexahedral	Tet. vs. Poly.	Tet. vs. Hex.
204,052	156,717	259,072	-	1.6187	1.5462	-	-
419,104	511,956	559,530	1.6260	1.6186	1.5488	0.46	4.98
821,771	-	-	1.6319	-	-	-	-
1,632,416	1,338,638	1,234,168	1.6179	1.6117	1.5504	0.38	4.35
3,352,832	-	-	1.6145	-	-	-	-
7,569,213	-	-	**1.6296**	-	-	-	-

Table 8.1: Area averaged WSS.

Number of cells			Area-averaged WSS (Pa)			Difference in WSS (%)	
Tetrahedral	Polyhedral	Hexahedral	Tetrahedral	Polyhedral	Hexahedral	Tet. vs. Poly.	Tet. vs. Hex.
-	97,558	189,332	-	1.6079	1.4706	-	-
497,681	317,630	497,340	1.6169	1.6010	1.4584	0.98	9.80
-	677,540	-	1.6260	1.6004		-	-
1,678,386	1,273,135	1,110,528	1.6311	1.5990	1.4696	1.97	9.91
3,609,451	-	-	1.6259	-	-	-	-

Table 8.2: Area averaged WSS of meshes with boundary layer.

8.2.2 Local WSS profiles

Three WSS profiles are extracted along the wall of the geometry for both the first order upwind scheme and the second order upwind scheme for the momentum equation. Each profile is extracted along a line at the wall of one

part of the artery: the Central carotid artery (CCA), the External carotid artery (ECA) or the internal carotid artery (ICA), displayed in Figure 8.2.

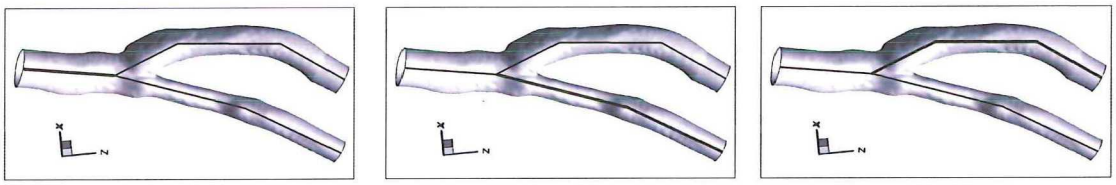

(a) CCA (b) ECA (c) ICA

Figure 8.2: Lines along which the local WSS profiles are extracted

Table 8.3: Mean value of the local WSS profile for various mesh types, mesh sizes and artery branches. The solution obtained with the tetrahedral mesh with over seven million cells (printed in bold font) is taken as reference solution.

Mesh type	Mesh size	CCA	ECA	ICA
Hexahedral	259,072	1.32	1.19	1.51
	559,530	1.32	1.19	1.52
	1,234,168	1.32	1.19	1.53
Hexahedral b.l.	189,332	1.30	1.14	1.41
	497,340	1.31	1.14	1.46
	1,110,528	1.32	1.14	1.46
Tetrahedral	419,104	1.41	1.27	1.61
	821,771	1.40	1.28	1.62
	1,632,416	1.41	1.26	1.60
	3,352,832	1.39	1.24	1.61
	7,569,213	**1.41**	**1.26**	**1.62**
Tetrahedral b.l.	497,681	1.45	1.30	1.62
	1,678,386	1.42	1.28	1.62
	3,609,451	1.42	1.28	1.62
Polyhedral	156,717	1.39	1.26	1.60
	511,956	1.38	1.25	1.61
	1,338,638	1.38	1.23	1.60
Polyhedral b.l.	97,558	1.37	1.31	1.60
	317,630	1.40	1.25	1.60
	677,540	1.38	1.26	1.60
	1,273,135	1.39	1.24	1.60

8.2.3 First and second order upwind scheme for momentum equation

In the computational methods (Section 4.1.1) is mentioned that a second order upwind scheme should give a more accurate result than a first order scheme. The WSS profiles for simulations using the first order upwind scheme are

shown in Figure 8.3 for the ECA. A difference in WSS between the coarse, middle and fine meshes of 5 – 10% is observed, whereas it is depicted in Figures 8.4 and 8.5 that this difference is at most 1% for the second order upwind scheme. The first order simulations approach the second order upwind simulations when the mesh is refined.

The difference between the first and second order upwind results is the largest for polyhedral meshes and smallest for hexahedral meshes. The close match for the hexahedral meshes is due to the alignment of the hexahedral cells with the main flow direction, as mentioned in Section 7.2. However, it can not be assumed that this numerical diffusion due to cell alignment is also present in more complex geometries. Therefore it is necessary for all mesh types to use the second order upwind scheme to ascertain the reliability of the results. The second order results are used in the coming sections for further mesh analysis and uncertainty analysis.

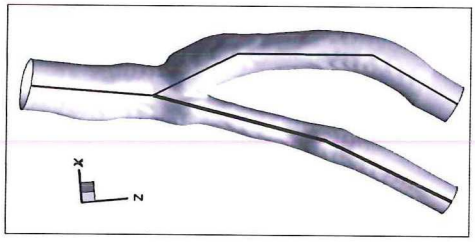

(a) ECA

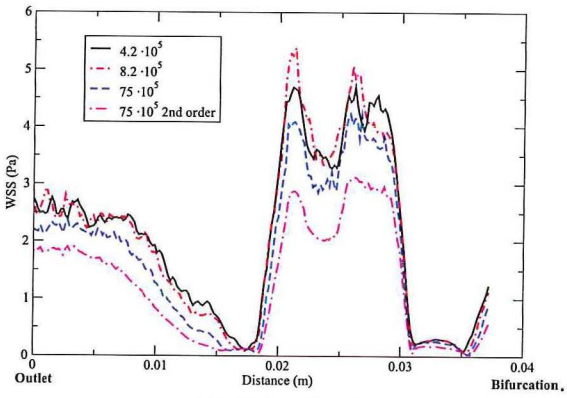

(b) Tetrahedral mesh

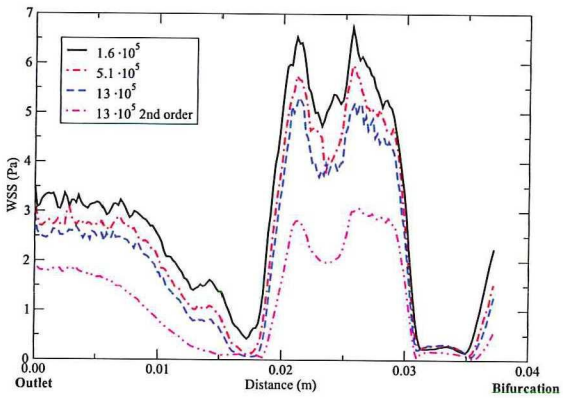

(c) Polyhedral mesh

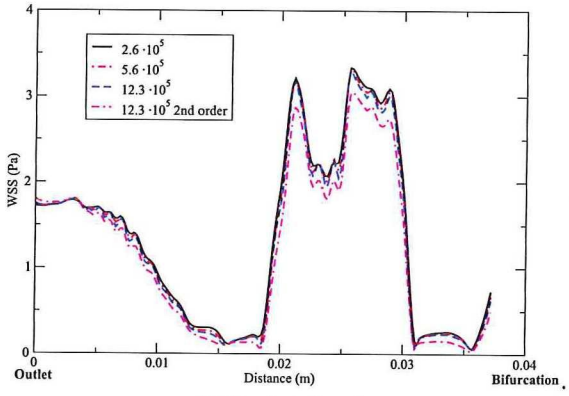

(d) Hexahedral mesh

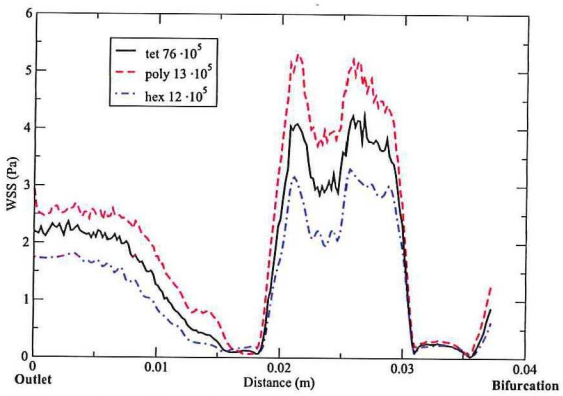

(e) Comparison of the WSS profile obtained using the first order upwind scheme at different mesh types.

Figure 8.3: Local Wall Shear Stress profiles extracted along the ECA obtained with first order upwind scheme for momentum for different mesh types.

8.2.4 Second order upwind scheme

Table 8.3 contains the average values of the local WSS profiles per branch, obtained with the second order upwind scheme. The reference solution (7 million tetrahedral cells) is approached best by tetrahedral meshes with a boundary layer and polyhedral meshes with and without a boundary layer. The average WSS obtained with the tetrahedral meshes with a boundary layer is slightly larger. The WSS profiles along the ICA are displayed in Figure 8.4 and Figure 8.5, where it is observed that the WSS profiles converge to one profile for larger cell density for each cell type. The solution from the finest tetrahedral mesh with over seven million cells is taken as a reference solution because of the high cell density. Looking at Figure 8.5 it is observed that the polyhedral and tetrahedral results are similar, while the computations on hexahedral meshes result in a lower WSS. The profiles from Figure 8.5 imply that eight hundred thousand tetrahedrals and just five hundred thousand polyhedral cells are required to provide sufficient accuracy.

The smaller cell density that is required for the polyhedral meshes to obtain a grid independent solution could be explained by looking at the boundaries of the geometry as described in Section 7.4. Polyhedral cells always share one face with the boundary, instead of a face, edge or just one node as is the case for tetrahedral cells. So a smaller amount of cells is taken into account in calculating the variables in each plane. When elucidating the structure of the boundary layer it is observed that the cell centres of the polyhedrals are distributed at a more regularly distance to the boundary plane. This results in a more regular WSS pattern and the pattern is resolved more accurately using polyhedrals when the same amount of cells is used as in the tetrahedral mesh.

8.2.5 Computational time

The number of iterations is chosen as the measure for the computational time. One could also compare the wall time needed to converge, but the number, age and speed of processors differed per simulation. The number of iterations that is required to obtain a convergent solution with the second order upwind scheme, starting from a converged first order upwind solution, is displayed in Table 8.4. For some simulations it was necessary to reduce the under-relaxation factor (URF, see Section 4.1.4) from 0.3 to 0.2 for the pressure and from 0.7 to 0.4 for the momentum equation. The URF determines the allowed change in solution between the former and the current iteration. Reasons for reducing the URF could be high skewness or a too large difference in volume of adjacent cells. The first simulation that is shown in Table 8.4 is computed with and without reduced URFs to see the influence of smaller URFs. The number of iterations is over eight times larger for the smallest hexahedral mesh with reduced URFs. This indicates that improvement of the hexahedral mesh quality could reduce the computational time.

It is predicted in Section 7.4 that the smallest computational time was required for the hexahedral meshes. The transitions between the blocks and the highly skewed cells, especially in the bifurcation, cause an increase in computational time of hexahedral meshes. The polyhedral meshes are preferred according to the number of iterations in Table 8.4, followed by the tetrahedral meshes.

The influence of the boundary layer on the number of iterations is very small. For hexahedral cells the computational time is observed to increase, probably due to the larger skewness. The computational time decreases for tetrahedral and polyhedral meshes when a boundary layer is included. The distribution of cells in meshes with a boundary layer complies better with the flow field since it contains large gradients at the wall and smaller gradients in the centre.

8.3 Solution extrapolation

An even more accurate WSS profile than the one obtained with the finest mesh can be constructed by extrapolating the solutions from the middle and the fine grids. Figure 8.4 and Figure 8.5 show the local WSS profiles along the

ICA for all mesh types. These solutions are extrapolated according to Equation 4.36 (equal to Equation 8.1).

$$\bar{f} = f_h + \frac{f_h - f_{rh}}{r^p - 1} \tag{8.1}$$

$\bar{f}$ is the extrapolation of a variable f, f_h is the solution of f on the finest mesh with characteristic cell size h and f_{rh} is the solution on the middle mesh, which is a factor r coarser. p is the formal order of accuracy, which is 2 because the second order upwind scheme is applied for the momentum equation.

The same trend is observed for the WSS profiles on the finest grids (Figure 8.5) and the extrapolated WSS profiles (Figure 8.6) both extracted along the ICA. The WSS profiles from the tetrahedral and polyhedral meshes are comparable and the hexahedral mesh results in smaller values. This is also observed for the WSS profiles from the ECA and the CCA.

8.4 Uncertainty quantification

The uncertainty analysis is performed founded on the local WSS profiles obtained with the second order upwind scheme. The applied method for quantifying the error on uniformly refined grids is discussed in Section 4.2.2. The uncertainty of the WSS results is calculated based on the Grid Convergence Index (GCI) and the observed order of accuracy ($\hat{p}$) Zou et al. (2010) (see Table 4.1). The uncertainty is computed from the WSS profiles from three meshes with different densities per cell type. It is shown for the ICA in Figure 8.7. A small uncertainty implies that the results from subsequent meshes agree well so that the solution is close to grid independence. A large uncertainty indicates a relatively large difference between the results obtained on subsequent meshes. It is clearly shown that the uncertainty reduces when the grid is refined, especially for the hexahedral and tetrahedral meshes.

The large peaks near the bifurcation occur due to the very small WSS at that location. The uncertainty is computed as a percentage of the WSS and a small deviation from a WSS close to zero could lead to a large uncertainty expressed in %. The mean uncertainty for each grid is summarized in Table 8.5 and it is computed by taking the mean value of the uncertainty profile per branch. Using hexahedral meshes results in the smallest discretization uncertainties followed by the polyhedrals. The use of tetrahedral meshes result in the largest uncertainty. So the smallest amount of cells is required for hexahedral meshes to obtain a grid-independent solution.

Although the hexahedral mesh is preferred based on the mesh independence, its WSS profile is different from that obtained with the other meshes and the reference solution. If the reference solution would have been chosen to use in the uncertainty calculation instead of the solutions obtained at the finest grid, the hexahedral cells would have had the largest uncertainty.

8.5 Recommendation on grid type

The results obtained with steady state single-phase Newtonian simulations are compared on WSS, computational time and discretization uncertainty for six mesh types. The results obtained with the second order upwind scheme for the momentum equation using polyhedral meshes correspond the best to the reference solution. Overall the smallest amount of polyhedral cells is required to obtain an accurate WSS profile. The polyhedral results are also acquired in the smallest computational time.

The uncertainty of WSS profiles from the polyhedral meshes is slightly larger than that obtained on the hexahedral meshes, but smaller than the results from the tetrahedrals (see Table 8.5). The computational time and results are scarcely influenced by the addition of a boundary layer that consists of smaller cells of the same type.

Combining these results with the knowledge that the mesh generating process is more complicated for the hexahedral meshes (Section 7.2) leads to a preference for the polyhedral meshes. The addition of a boundary layer is

also recommended because of future implementations of mass transport through the blood vessel wall and fluid structure interaction (FSI). Both mechanisms are expected to influence the WSS magnitude and the development of vascular diseases significantly. It is required to resolve the velocity and its derivative in the proximity of the wall with high accuracy when these mechanisms are added. Therefore a polyhedral mesh with a boundary layer is recommended.

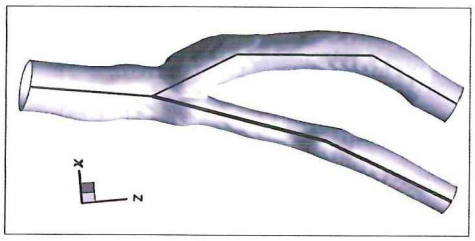

(a) ICA

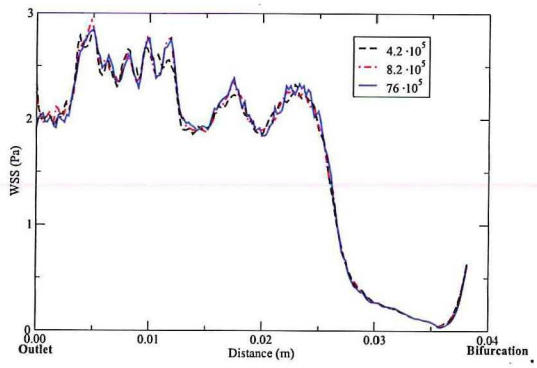

(b) Tetrahedral mesh

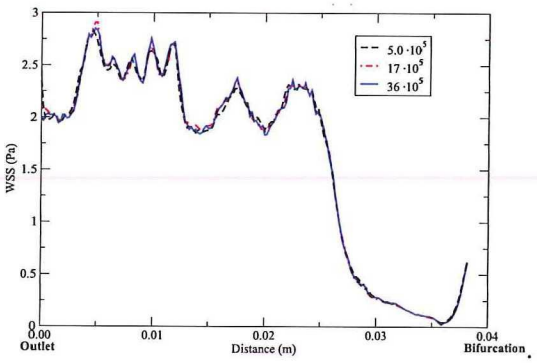

(c) Tetrahedral mesh with boundary layer

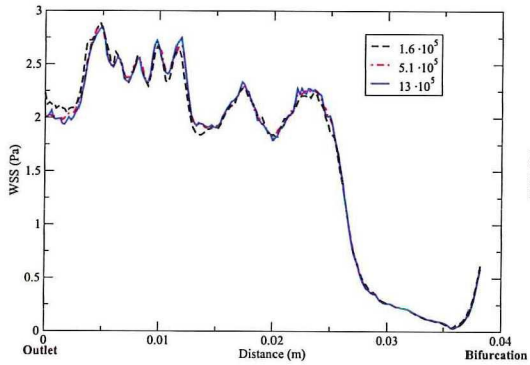

(d) Polyhedral mesh

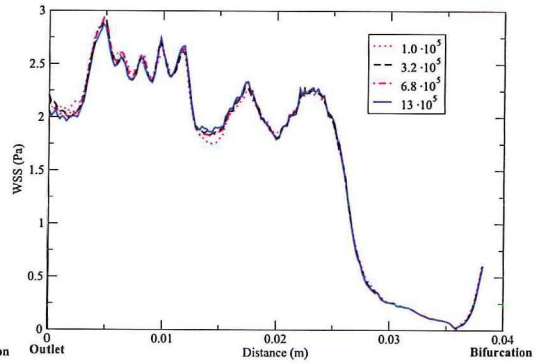

(e) Polyhedral mesh with boundary layer

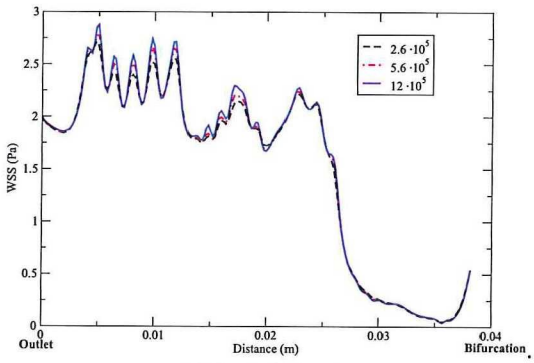

(f) Hexahedral mesh

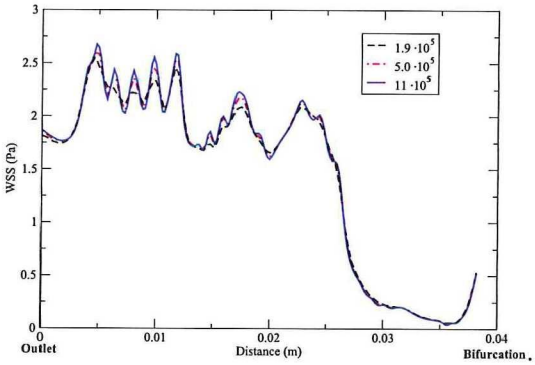

(g) Hexahedral mesh with boundary layer

Figure 8.4: Local Wall Shear Stress profiles extracted along the ICA obtained with second order upwind schemes for the momentum equation for different mesh types.

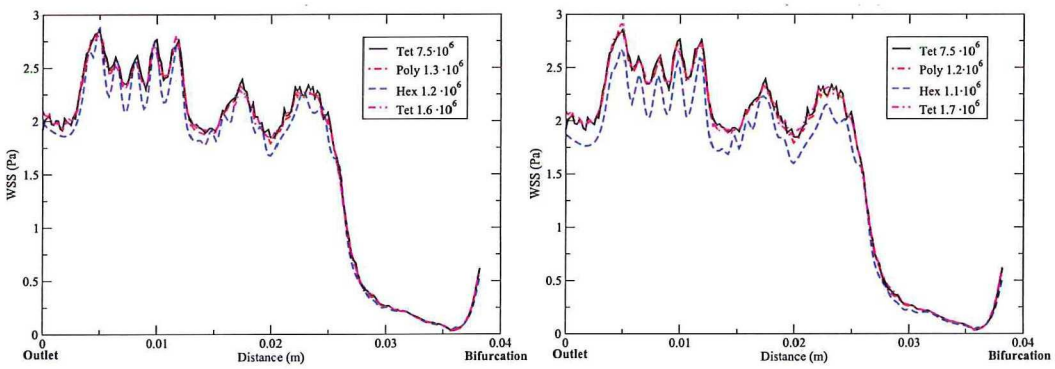

(a) Grid comparison second order **(b)** Grid comparison second order with boundary layer

Figure 8.5: Local Wall Shear Stress profiles, obtained with second order upwind scheme for the momentum equation, compared for grids with about 1 million cells. The reference solution from the tetrahedral grid containing 7.5 million cells is also plot in both graphs.

Table 8.4: Number of iterations required to converge using a second order upwind scheme for the momentum equation. The initial solution is a converged solution obtained with the first order upwind scheme for momentum equation. There are some exceptions in the numerical setup denoted by the union symbol ($^{\cup}$). The under-relaxation factors (Equation 4.21) for the pressure and the momentum equations are reduced in these cases.

Mesh type	Mesh size (CV's)	# iterations for 2nd order upwind to converge	Mesh type	Mesh size (CV's)	# iterations for 2nd order upwind to converge
Hexahedral	259,072	551 4534$^{\cup}$	Hexahedral b.l.	189,332	523
	559,530	6,449 $^{\cup}$		497,340	956 $^{\cup}$
	1,234,168	9,375 $^{\cup}$		1,110,528	9,957 $^{\cup}$
Tetrahedral	204,052	-	Tetrahedral b.l.		
	419,104	1,230		497,681	1,359
	821,771	1,588			
	1,632,416	1,954		1,678,386	1,797
	3,352,832	2,556		3,609,451	17,880 $^{\cup}$
	7,569,213	3,759			
Polyhedral	156,717	497	Polyhedral b.l.	97,558	424
				317,630	590
	511,956	829		677,540	684
	1,338,638	1,208		1,273,135	801

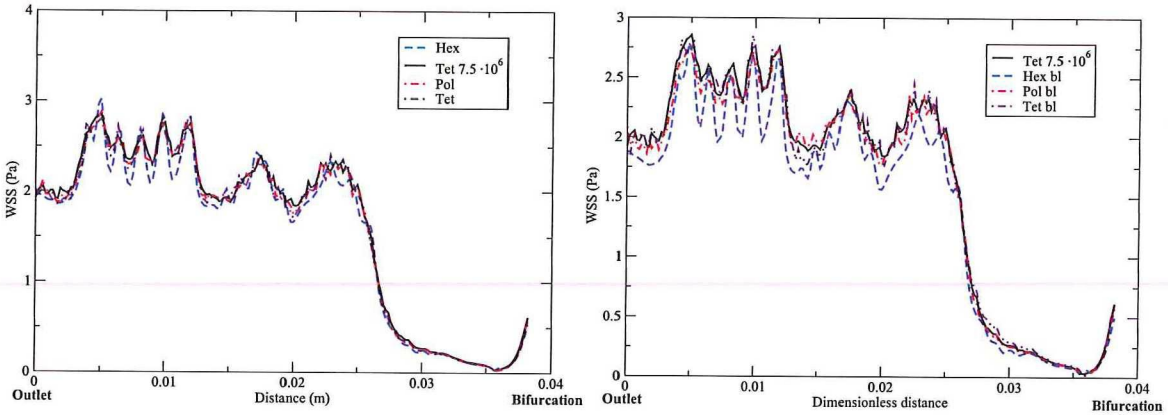

(a) Meshes without boundary layer

(b) Meshes with boundary layer

Figure 8.6: WSS profiles along the ICA extrapolated according to Roy (2010) (Equation 4.36).

Table 8.5: Mean uncertainty per branch per grid type for finest grid displayed in Figure 8.7. The uncertainty is computed according to Table 4.1 from the extracted WSS profiles. The mean uncertainty per branch is taken from the uncertainty profile and it is expressed in Pa.

	Hexahedral		Tetrahedral		Polyhedral	
		bl		bl		bl
ECA	0.021	0.027	0.068	0.059	0.043	0.041
ICA	0.039	0.041	0.070	0.045	0.051	0.042
CCA	0.038	0.045	0.046	0.064	0.039	0.053

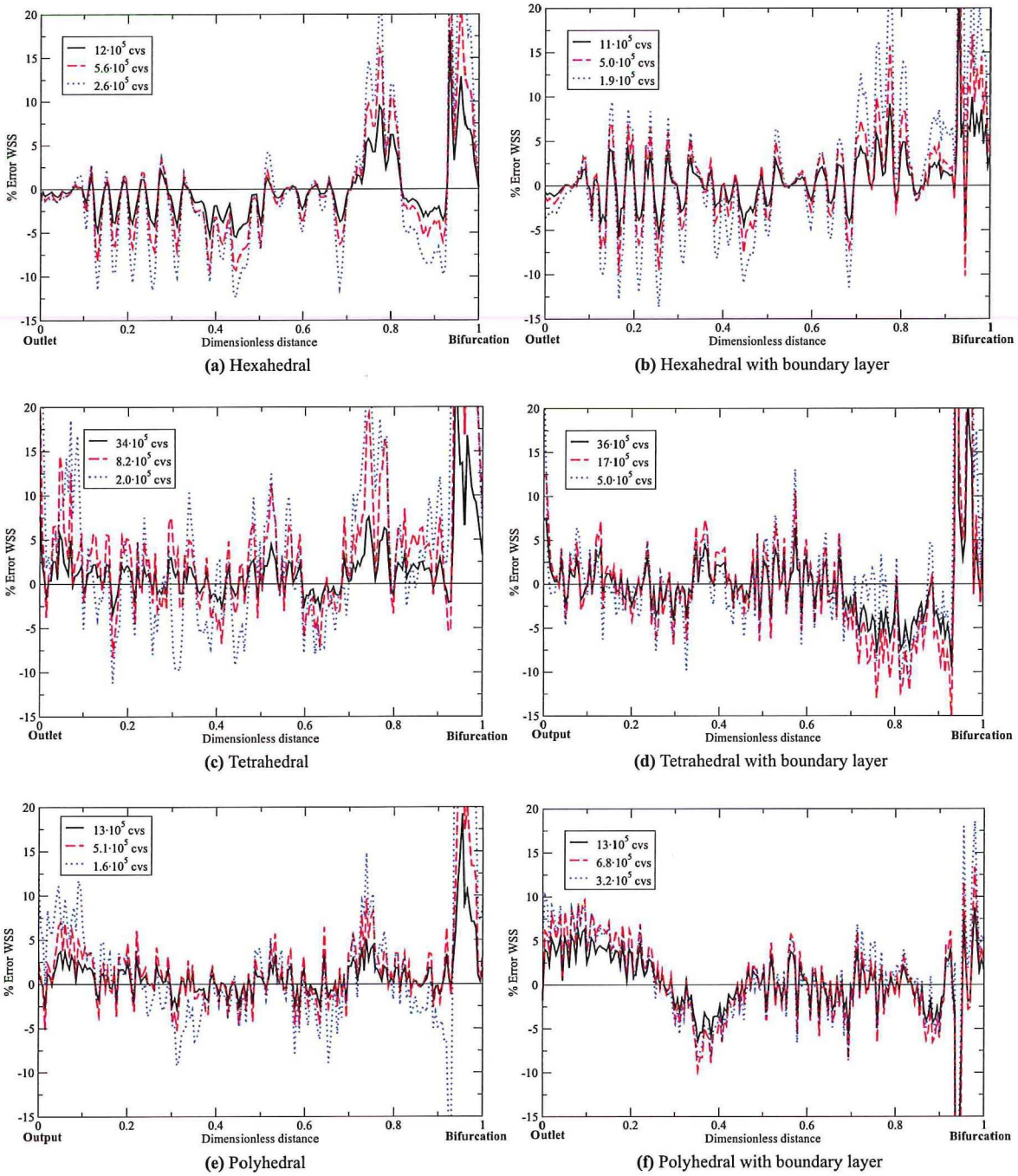

(a) Hexahedral

(b) Hexahedral with boundary layer

(c) Tetrahedral

(d) Tetrahedral with boundary layer

(e) Polyhedral

(f) Polyhedral with boundary layer

Figure 8.7: Uncertainty profiles of the WSS extracted along the ICA.

CHAPTER 9

Non-Newtonian single-phase and multiphase flows in healthy Carotid bifurcation

The results of CFD computations of single-phase Newtonian blood flows through the healthy Carotid Artery (CA) are presented in the previous chapter. The results of two non-Newtonian models are discussed in Chapters 5 and 6. Those are the single-phase and the two-phase flow with the Carreau-Yasuda model. These models are implemented in the healthy CA and the results are compared with the Newtonian flow results presented in Chapter 8. The computations are performed on polyhedral meshes with and without a boundary layer following the recommendation of the previous chapter. Both meshes consist of about 1.3 million cells. The computational effort and the results are compared for the three models of blood: single-phase with constant viscosity, single-phase with the Carreau-Yasuda viscosity model and multiphase with the same non-Newtonian viscosity model.

9.1 Numerical setup

The numerical setup for the Newtonian single-phase flow is described in Section 8.1 The settings of the non-Newtonian flows are based on these settings for a fair comparison. The flow properties and the boundary conditions for the non-Newtonian models are summarized in Table 9.1. All presented results are extracted from fully convergent simulations with the second order upwind scheme applied for the momentum equation.

9.2 Computational time

First of all the computational times for the multiphase simulations on both grid types are compared. The simulations are carried out on the same node at the same computational cluster in parallel mode using four CPUs. It took 1525 iterations in sixteen hours and a half on the polyhedral grid. At first 300 iterations were carried out using first order upwind scheme and then there is switched to the second order upwind scheme for the momentum equitation. The computational time on the polyhedral mesh with boundary layer is smaller, just as observed for the Newtonian single-phase flow (see Table 8.4). It took only 1001 iterations and nine hours and twenty minutes to obtain a convergent solution. The solutions are considered to be converged when the residual of the continuity equation is below 10^{-6} and the other residuals, those of the velocity components of both phases as well as the residuals of the volume fraction of RBC, are below 10^{-10}. The residuals have dropped eight to nine orders of magnitude compared to the second iteration and five to six orders compared to the second iteration with the second order upwind scheme. A drop of only two or three orders of magnitude is required. The stern demands for convergence are chosen to be certain to compare fully converged solutions for the single-phase and multiphase flows.

It is observed for the single-phase simulations that it takes about 69% more iterations for the Newtonian to even 90% more iterations for the Carreau-Yasuda model to get a convergent solution on the grid without a boundary layer. Therefore the polyhedral mesh with a boundary layer is preferred based on the computational time.

Table 9.1: Numerical setup for the non-Newtonian simulations of blood flow through a healthy carotid artery. The volume fraction of RBCs is fixed at 45% for the single-phase simulation. Re is calculated using the mean blood properties: μ = 0.0037Pa·s, ρ = 1057 kg/m^{3}and inlet diameter D = 6.1mm.

Models	
Carreau-Yasuda viscosity model	$\mu_{mix} = \mu_{plasma} m\left(1 + (\lambda\dot{\gamma})^2\right)^{\frac{n-1}{2}}$ $n = 0.8092\varepsilon_{RBC}^3 - 0.8246\varepsilon_{RBC}^2 - 0.3503\varepsilon_{RBC} + 1$ $m = 122.28\varepsilon_{RBC}^3 - 51.213\varepsilon_{RBC}^2 + 16.305\varepsilon_{RBC} + 1$ $\mu_{plasma} = 0.001$ Pa·s $\lambda = 0.110$ s $\mu_{mix} = \varepsilon_{RBC}\mu_{RBC} + \varepsilon_{plasma}\mu_{plasma}$
Density	$\rho_{plasma} = 1020$ kg/m^3 $\rho_{RBC} = 1100$ kg/m^3 $\rho_{single-phase} = 1057$ kg/m^3
Particle diamter	$d_p = 8.2\mu$m
Boundary conditions	
Inlet volume fraction	$\varepsilon_{RBC} = 0.45$
Inlet velocity	parabolic profile with $u_{max} = 0.338$m/s ($Re = 295$) parabolic profile with $u_{max} = 0.1127$m/s ($Re = 98$)
Wall velocity	zero slip velocity for all phases
Pressure outlet ECA	13325.86 Pa
Pressure outlet ICA	13332.2 Pa
Initialization	
Volume fraction	$\varepsilon_{RBC} = 0.45$
Velocities	$\mathbf{u} = \mathbf{0}$ m/s

9.3 Results

The velocity profiles and stream traces are shown for the three models on both meshes. The results are very similar for both meshes so the other parameters of interest are shown for the mesh with boundary layer since the shortest computational time is required to obtain a converged solution on that mesh.

9.3.1 General flow behaviour

The velocity magnitude and some stream traces are displayed in Figures 9.1 and 9.2 for Re = 295 which is the mean Re for the CA. The results for the two single-phase flows and the multiphase flow are compared for the polyhedral grid with and without a boundary layer (see Figures 7.2e and 7.2f). Some disturbances in the flow are observed at the bifurcation and near both exits. The disturbance at the exits is due to the large velocity in combination with the curvature of the artery. The flow patterns are similar for both meshes, which indicates that the solution is grid-independent for this amount of polyhedral control volumes.

In Figure 9.3 is zoomed in at the Internal Carotid Artery with boundary layer, shown at the left of figures 7.2e and 7.2f. The velocity magnitude is slightly larger for the Newtonian fluid, which is best visible in the upper five slices. This is due to the larger viscosity for the non-Newtonian flows near the peak of the parabolic-shaped velocity profile due to the small strain rate.

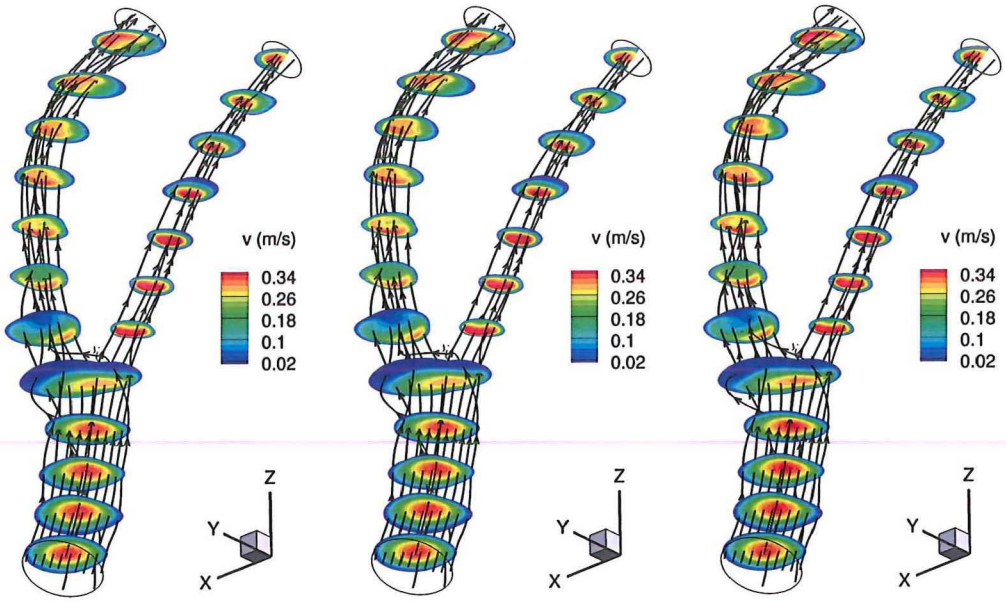

(a) Multiphase, no bl (b) Single-phase Carreau-Yasuda (c) Single-phase Newton

Figure 9.1: Velocity magnitude contours and stream traces through the healthy carotid artery without boundary layer for $Re = 295$. The velocity magnitude and stream traces of plasma are displayed for the multiphase simulation.

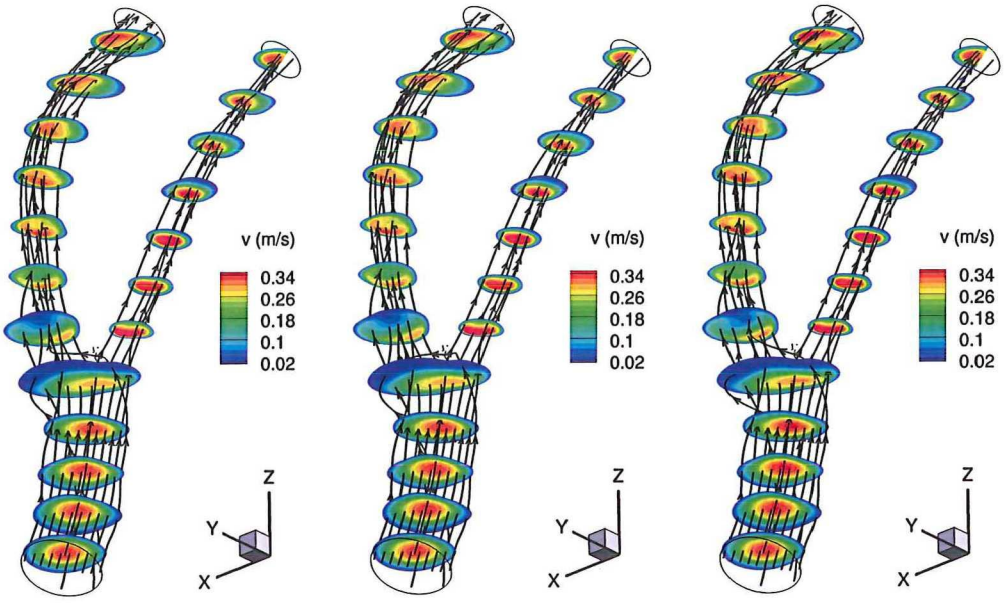

(a) Multiphase, incl bl (b) Single-phase Carreau-Yasuda (c) Single-phase Newton

Figure 9.2: Velocity magnitude contours and stream traces through the healthy carotid artery with boundary layer for $Re = 295$. The velocity magnitude and stream traces of plasma are displayed for the multiphase simulation.

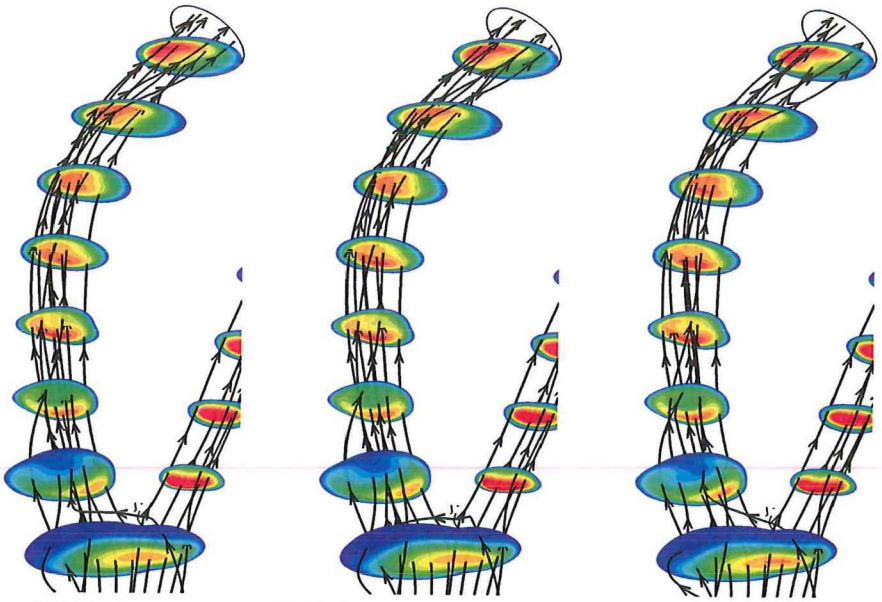

(a) Multiphase (b) Single-phase Carreau-Yasuda (c) Single-phase Newton

Figure 9.3: Close-up of the velocity magnitude contours and stream traces through the Internal Carotid Artery with boundary layer for $Re = 295$. The velocity magnitude and stream traces of plasma are displayed for the multiphase simulation.

9.3.2 Volume fraction, viscosity and Wall Shear Stress

The RBC volume fraction distribution at the wall is displayed in Figure 9.4a where it is visualized that the deviation in the RBC volume fraction from 0.45 is minor. The similar velocity profiles and this quite homogeneous distribution of ε_{RBC} leads to the expectation that the viscosity distributions are also comparable for the non-Newtonian simulations. Therefore the viscosity is extracted at the same slices as the velocity magnitude from Figures 7.2e and 7.2f and these contours are displayed in Figure 9.4. The mixture viscosity from the multiphase model is compared with the viscosity from the single-phase non-Newtonian simulation, both computed at the polyhedral grid with boundary layer. The viscosity profiles at these slices are exactly the same which indicates that the extra computational effort of the multiphase approach does not result in a better agreement with complex blood properties.

A parameter that is of particular interest is the Wall Shear Stress since it is known to affect the genesis of vascular diseases. Figure 9.5 shows that the Newtonian flow induces a slightly larger WSS at the right branch, but the rest of the WSS distribution is of close agreement for the three models.

The non-Newtonian viscosity averaged over the whole geometry is 0.0046 Pa·s which is 24% larger than the Newtonian viscosity. It is remarkable that the results in velocity profiles and WSS distribution are quite similar. The similarity in WSS profiles could be explained to the observation that the viscosity near the wall is close to 0.0037 Pa·s. The larger viscosity in the flow centre results in a slightly flattened velocity profile which is mentioned in the discussion on the general flow patterns (Section 9.3.1) by pointing out the smaller maximum velocity.

9.3.3 Smaller Reynolds number

A larger difference between the Newtonian and non-Newtonian models is expected for a smaller Re because the Carreau-Yasuda model is a shear-thinning model with a strongly increased viscosity for small strain rates. The smallest inlet velocity in the Carotid Artery derived from the mean human heart-pulse constructed by Holdsworth

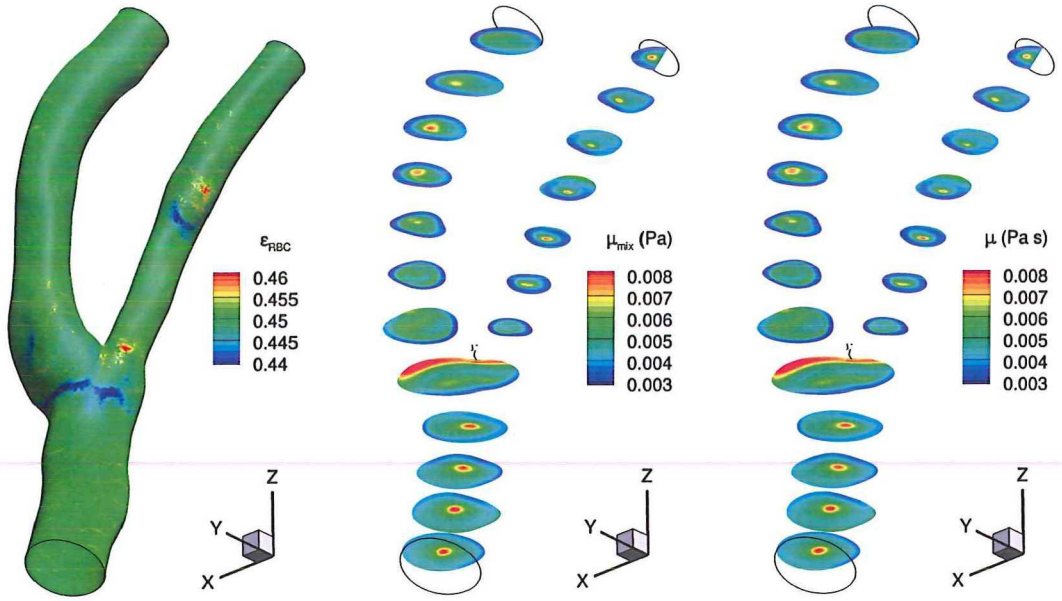

(a) RBC volume fraction **(b)** Multiphase **(c)** Single-phase Carreau-Yasuda

Figure 9.4: The volume fraction averaged mixture viscosity is displayed for the multiphase simulation (a). Viscosity contours are shown at slices in the healthy carotid artery with boundary layer for $Re = 295$ ((b) and (c)).

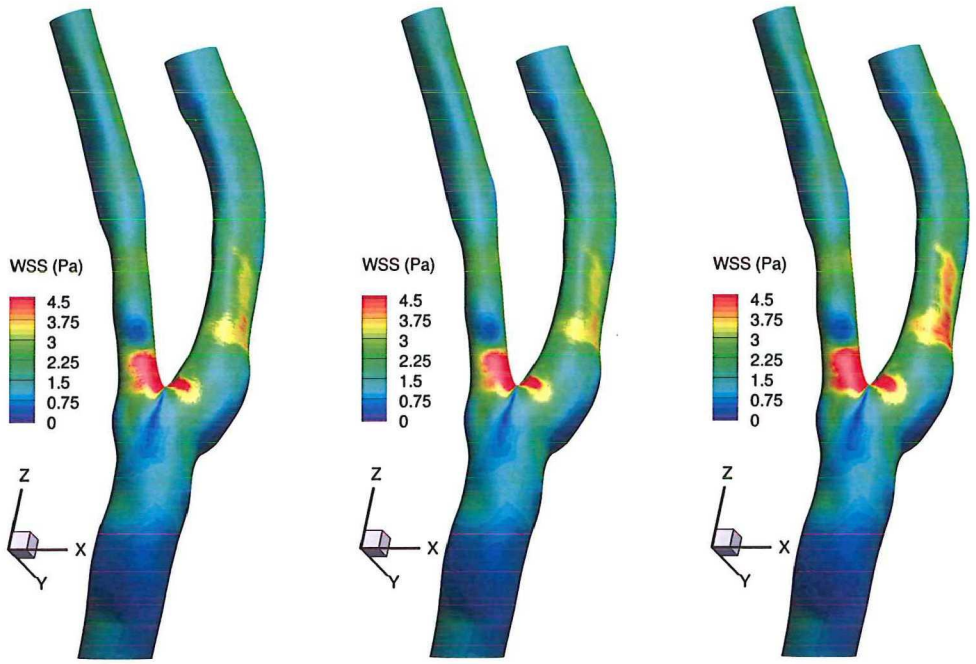

(a) Multiphase **(b)** Single-phase Carreau-Yasuda **(c)** Single-phase Newton

Figure 9.5: Wall Shear Stress contours at the blood vessel wall for a blood flow through the healthy carotid artery. The CA is meshed with polyhedrals including a polyhedral boundary layer and $Re = 295$ at the inlet. The WSS is volume fraction averaged for the multiphase simulation.

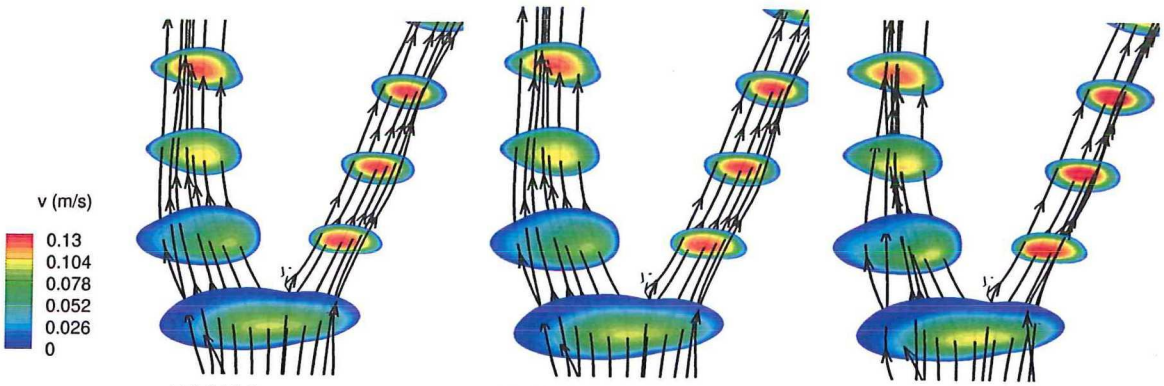

(a) Multiphase (b) Single-phase Carreau-Yasuda (c) Single-phase Newton

Figure 9.6: Velocity magnitude contours and stream traces through the healthy carotid artery for $Re = 98$, meshed with polyhedrals including a boundary layer. The velocity magnitude and stream traces of Plasma are displayed for the multiphase simulation.

et al. (1999) results in $Re = 98$. Holdsworth et al. (1999) carried out Doppler ultrasound velocity measurements on the left and right carotid artery and an average heart-pulse is computed from 3570 cardiac cycles from seventeen volunteers.

More flattened velocity profiles could be observed in for $re = 98$ (Figure 9.6) than for $Re = 295$ (Figure 9.3) due to the larger mean viscosity of 0.0059 Pa·s. This is most clearly observed in the first slide above the bifurcation in both branches. The maximum velocity is larger for the Newtonian flow in the right branch. The left branch shows more oval shaped velocity contours for the non-Newtonian simulations compared to a moon-like shape observed in the Newtonian result. The similarity in WSS profile (which is not shown in this report) is comparable to that obtained for $Re = 295$. Since $Re = 98$ is only three times smaller than 295 it is not surprising that the effect of the non-Newtonian models has only slightly increased.

9.4 Discussion and conclusion

Steady state blood flow through a healthy human carotid artery could be modelled by a Newtonian or non-Newtonian single-phase fluid using the Carreau-Yasuda viscosity model. The third model is a two-phase model with the Carreau-Yasuda applied to one phase: the red blood cells. The difference between the multiphase and single-phase Carreau-Yasuda results is minor so it is advised to save the computational costs required to model a multiphase flow. A single-phase Newtonian simulation provides sufficient information when the general flow pattern and the peaks in WSS values are the parameters of interest. Regarding the uncertainties due to the assumptions that are made by using a steady state model with rigid walls leads to the conclusion that the extra computational effort of a non-Newtonian model does not lead to significant improvement in accuracy.

Johnston et al. (2004) came to the same conclusion when comparing blood flow through five right coronary arteries. Blood was modelled as a single-phase non-Newtonian fluid using five different viscosity models. Their coronary arteries exhibit diameters of about 5 mm, contain more bends then the bifurcation discussed in this chapter but no bifurcation. The inlet centreline velocity is varied between 0.02 m/s and 1 m/s. For the intermediate flow rates with centreline velocity between 0.1 and 0.2 m/s it is concluded that the results from the five models are practically undistinguishable. This flow rate regime coincides with the flow settings in the present research in which a similar conclusion is drawn.

The local non-Newtonian importance factor I_l (see Equation 6.2) at the wall is observed to reach from 1 to 1.8 for a simulation of single-phase blood with the General Power Law as viscosity model and u_{in} = 0.05 m/s (Johnston et al., 2004) . This is in the same order as the maximum value of I_l = 2.2 obtained in the present study for the healthy carotid artery for Re = 295.

50% to 70% more computational time is required to acquire a convergent multiphase solution on the polyhedral mesh without a boundary layer than on the polyhedral mesh with a boundary layer. This leads to an addition to the advice given in Section 8.5. In that section it is denoted that polyhedral meshes are preferred but the boundary layer is just advised regarding the possibility of future implementation of mass transport through the arterial wall and fluid structure interaction. The large difference in computational time that is encountered for multiphase flows adds a strong argument for indeed including the boundary layer.

CHAPTER 10

Non-Newtonian single-phase and multiphase flow in diseased Carotid bifurcation

Different models for human blood are examined in order to be able to predict the development of vascular diseases and the impact of medical treatment. It is concluded in the previous chapter that the multiphase approach is not required for accurately modelling blood flow in a healthy carotid artery. Therefore simulations are performed in a diseased carotid artery using the same settings as for the healthy carotid artery, except for the boundary condition at the inlet and the mesh type. The tetrahedral mesh with boundary layer created by Righolt (2010) is used (see Figure 10.1a). The same parabolic profile that is used for the flow described by $Re = 98$ in the healthy CA with $u_{max} = 0.1127$ m/s is used as inlet boundary condition. Its direction is normal to the inlet plane instead of parallel to the blood vessel. The Reynolds number based on the mean blood viscosity of 0.0037 Pa·s and the inlet equivalent diameter of the inlet of 7.45 mm is 120.

10.1 Results

At first the general flow behaviour through the diseased artery is discussed. Then a closer look is taken at the vorticity, the viscosity and the Wall Shear Stress (WSS) obtained with the three flow models.

10.1.1 General flow behaviour

The flow behaviour is analyzed using stream traces and z-velocity contours at evenly distributed planes as shown in Figure 10.1b for the multiphase flow. Some swirls are observed just after the bifurcation and after the narrowing, but there is no back-flow observed. Only the flow pattern of the multiphase flow is presented because the flow behaviour of the three models is almost identical, just like the simulations of the flow through the healthy carotid artery.

The likely difference between the multiphase flow and the single-phase non-Newtonian flow is assessed by looking at the RBC volume fraction at the wall of the artery in Figure 10.1c. Some red regions are visible with a slightly increased ε_{RBC} but the narrowing of the artery induces too little recirculation for this Re to require the usage of the multiphase approach.

10.1.2 Vorticity, viscosity and WSS

The vorticity of a fluid is a measure for the rotations that is present in the flow. Vorticity is defined as:

$$\omega = \nabla \times \mathbf{u} \tag{10.1}$$

A close-up of the upper part of the carotid artery is used to display the vorticity magnitude and stream traces for all three models in Figure 10.2 and no difference is observed. This indicates that the presence of RBCs barely influences the flow pattern in this geometry for $Re = 120$.

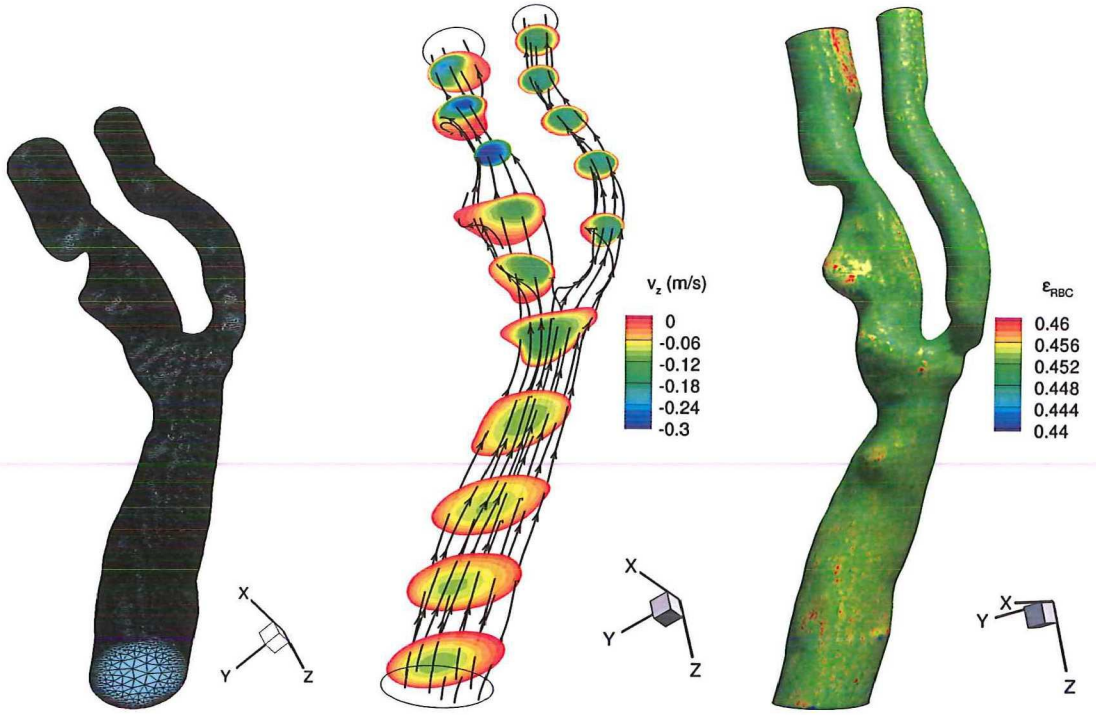

(a) Tetrahedral mesh, 1.13 million cells **(b)** Multiphase z-velocity contours **(c)** Multiphase RBC volume fraction

Figure 10.1: Streamtraces and z-velocity contours for multiphase flow through a diseased carotid artery. The volume fraction of RBCs at the wall is also shown.

The viscosity contours from Figure 10.3 reveal that the viscosity is basically equal for the non-Newtonian flow as is expected from the minor deviations in ε_{RBC} from 0.45 in shown in Figure 10.3a. On the contrary, some difference is observed in the WSS contours between the three simulations in the WSS contours (see Figure 10.4), especially at the smallest part of the left branch. The largest WSS is shown for the Newtonian flow due to the larger viscosity at the wall. The WSS due to the multiphase blood flow is slightly larger than for the single-phase non-Newtonian flow while the RBCs are distributed evenly at the smallest part of the artery due to the large velocity.

10.2 Transient flow

In the introduction of this chapter it is mentioned that the geometry and mesh of the diseased Carotid Artery are received from Righolt (2010). He used transient parabolic inlet profile as inlet boundary condition where the peak velocity of the parabola is scaled with the heart-pulse obtained by Holdsworth et al. (1999). The blood is modelled as a single-phase flow with the viscosity modelled according to the Generalized Power Law (Section 2.2.1). Reversed flows are observed at certain times in the cardiac cycle, mainly at times of flow deceleration and minimum velocity like the flow pattern at $t/T = 0.45$ displayed in Figure 10.5.

In the multiphase simulations in the suddenly expanding tube in the present study (see Chapter 6) it is shown that the multiphase approach leads to significant improvement of the agreement with real blood behaviour when flow recirculation is present. This is due to the reduction of the RBC volume fraction in the recirculation zone. Combining those results with the observed swirling flow in Figure 10.5 leads to the expectation that the multiphase approach is required if the research topic is the transient flow behaviour.

Johnston et al. (2006) compared the transient flow through four coronary arteries of a Newtonian flow with a non-Newtonian flow using the Generalized Power Law (GPL) for the viscosity. The non-Newtonian model is found

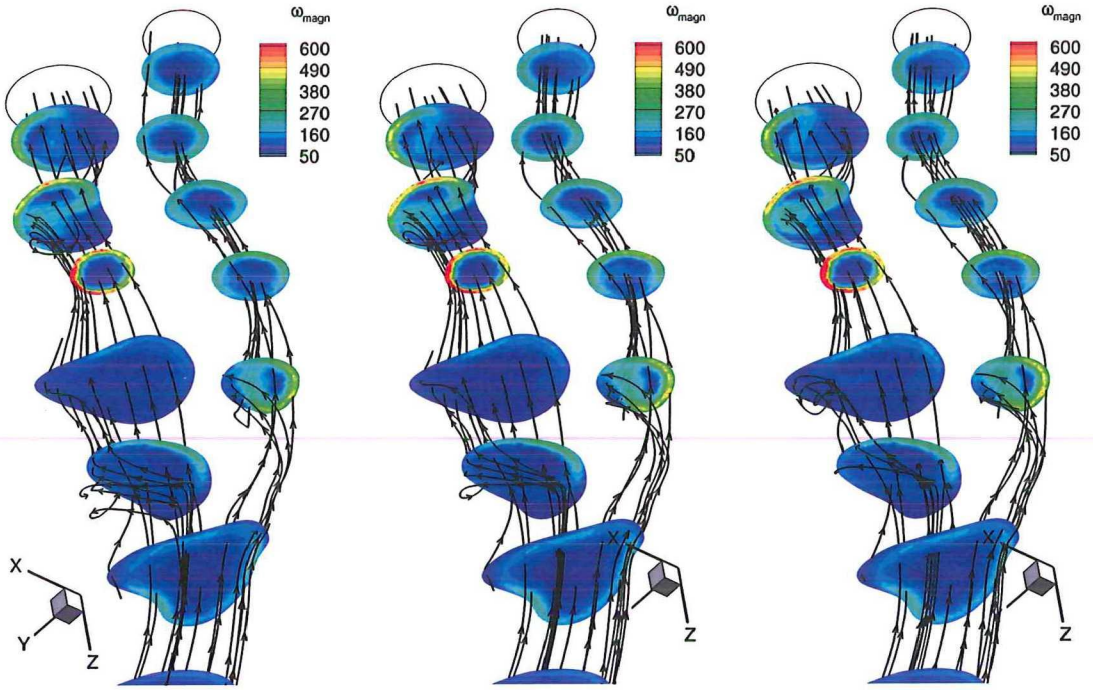

(a) Multiphase **(b)** Single-phase Carreau-Yasuda **(c)** Single-phase Newton

Figure 10.2: Vorticity in the diseased carotid artery.

to give significantly different results for the WSS for approximately 30 % of the cardiac cycle where the velocity is the smallest. The WSS is very small (smaller than 0.5 *Pa*) for these small velocities so it is doubtful whether a large difference on this scale really is significant. The results hold for a heart rate for a resting person and the significance of the non-Newtonian model will reduce for larger heart rates.

Local non-Newtonian importance factors larger than three are observed at the wall during 20% of the cardiac cycle, mainly for decelerating and reverse flows. This is larger than the values that are observed in the current diseased artery for $Re = 120$. However, I_l varies between 1 and 1.4 for inlet velocities of circa 0.10 m/s which flow regime is more similar to the flow regime in the diseased artery.

The inlet velocity profile of the coronary artery is quite different from that of the carotid artery. The coronary artery encounters backflow for roughly 10 % of the cardiac cycle while the flow through the carotid artery retains an inlet velocity of at leas 0.11 m/s. Therefore the discrepancy between the results using the GPL or the Newtonian viscosity model is expected to be even smaller in the carotid artery.

When the mixing of blood is the topic of interest or individual particles have to be traced, it is recommended to rather use the non-Newtonian model (Johnston et al., 2006). It is observed that a difference in flow patterns between the two viscosity models that do not greatly affect the WSS but could result in a different particle distribution. This observation resembles with the present study.

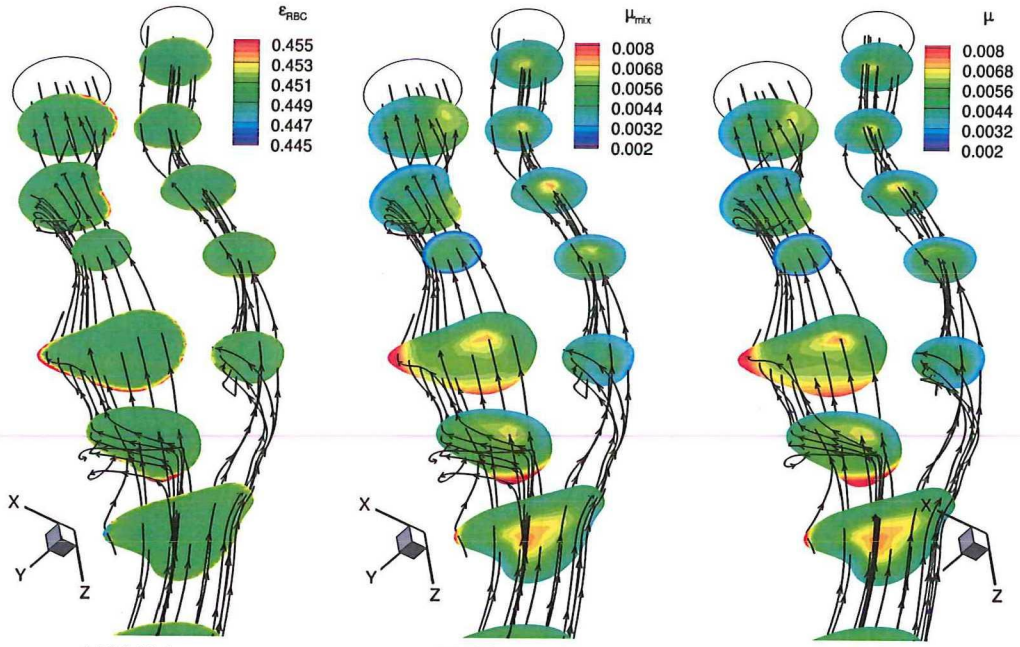

(a) Multiphase ε_{RBC} (b) Multiphase μ_{mix} (c) Single-phase Carreau-Yasuda

Figure 10.3: Streamtraces and viscosity contours for blood flow through a diseased carotid artery, compared to the RBC volume fraction. The mixture viscosity is volume fraction averaged.

10.3 Conclusion

The Carotid Artery is one of the major arteries of the human vascular system so the Reynolds number of its blood flow is larger than 80 during the whole cardiac cycle. Therefore the flow is quite smooth with small swirls but without recirculating flow that could cause a heterogeneous RBC distribution. The flow patterns and WSS profiles are very similar for the single-phase Newtonian flow, the single-phase Carreau-Yasuda flow and the multiphase flow. For blood flows that are described by such large *Re* it is recommended to use the single-phase Newtonian model since the blood rheology is well described by a constant viscosity in these arteries, even when the artery is heavily diseased.

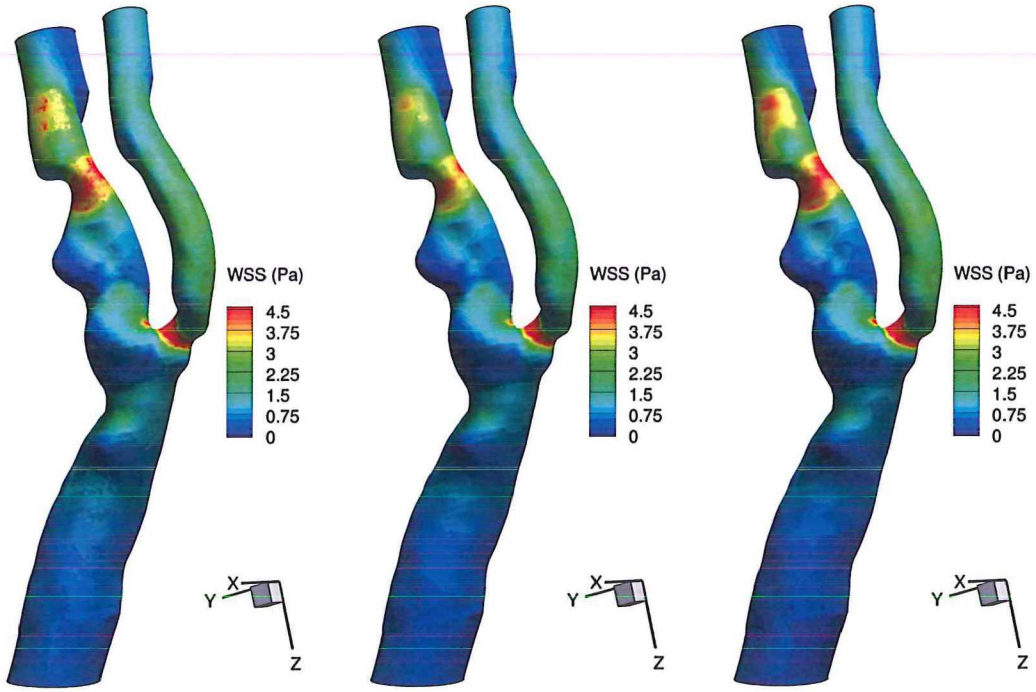

(a) Multiphase **(b)** Singl-phase Carreau-Yasuda **(c)** Singl-phase Newton

Figure 10.4: WSS at the vessel of the diseased carotid artery

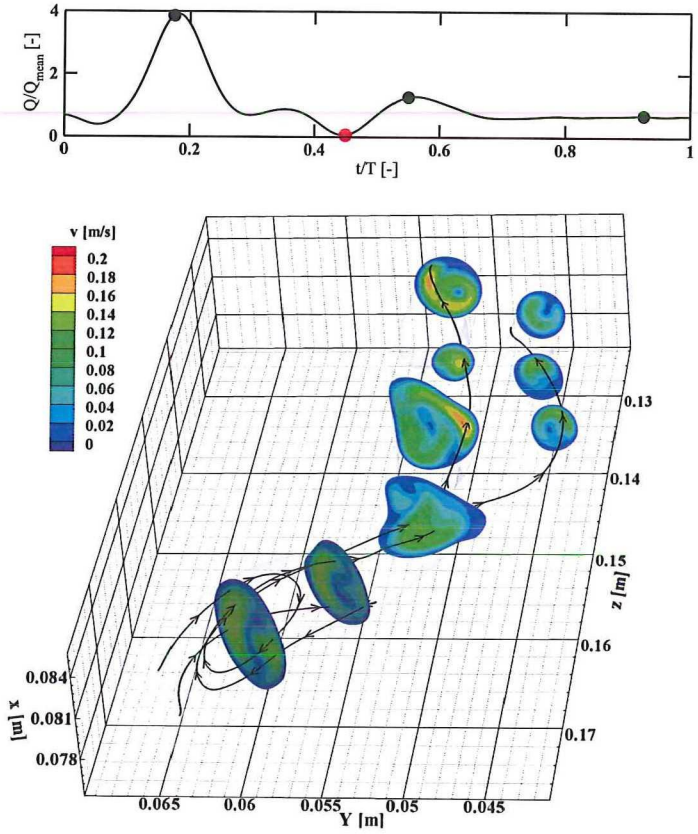

Figure 10.5: Flow pattern for a transient single-phase GPL flow for the smallest inlet velocity at $t/T = 0.45$ (Righolt, 2010).

CHAPTER 11

Conclusions

This study is part of a research project to develop a CFD model that could be used as a medical instrument to predict the development of cardiovascular diseases and the impact of new treatments. It has two focus areas in the development of a model of blood flow through the human carotid artery (CA). Six mesh topologies of a healthy CA are examined on meshing procedure, computational time and numerical uncertainty. Secondly the importance of applying the shear-thinning Carreau-Yasuda viscosity model in a single-phase and a multiphase flow is investigated on agreement with blood behaviour. Single-phase and multiphase flows through simplified and real three-dimensional human arteries are simulated using the CFD package Ansys Fluent.

11.1 Selection of numerical mesh topology for the CA

A healthy CA is meshed with six mesh types consisting of one of the following cell types: hexahedrals, tetrahedrals and polyhedrals which are merged tetrahedrals. A mesh with and without a boundary layer is created for these three cell types. The boundary layer consists of smaller cells of the same cell types as the main part of the mesh. The polyhedral mesh with boundary layer outperforms the other meshes on computational time required to obtain a fully converged steady state solution. The meshing procedure for polyhedral meshes could be automated well as opposed to the hexahedral meshing procedure. Automatic mesh generation is a large advantage since each patient's vascular system is unique and should be meshed from scratch.

The discretization error is slightly smaller for hexahedral meshes but sufficient accuracy is obtained with polyhedral meshes. This discretization error is comparable for both polyhedral mesh types, but the computational time is decreased significantly when the boundary layer is included. Implementing mass transport of lipids through the vessel wall and fluid-structure interaction would improve the resemblance with the human body. These mechanisms require very accurately resolved flow properties at the wall, which also argues in favour of implementing a boundary layer.

11.2 180 ° bended tube

A simplification of the right coronary artery is a 180° bended tube with a diameter of 4.37 mm and a radius of curvature of 41.515 mm (Jung et al., 2006). The non-Newtonian Carreau-Yasuda viscosity model results in a 30% smaller WSS at the outside bend during 25% of the cardiac cycle than for the Newtonian flow. The extension to a multiphase fluid model of Red Blood Cells (RBCs) suspended in Newtonian plasma gives similar results to the non-Newtonian single-phase model. The two-phase approach does not improve the resemblance with the blood rheology. Therefore it is concluded that blood flow with $134 < Re < 382$ through a bended tube with a constant diameter should be modelled as a non-Newtonian single-phase fluid.

11.3 Rapidly expanding tube

A diseased artery with a severe obstruction could be approximated by a suddenly expanding tube which represents the obstruction and its downstream region. Recirculation zones are observed in steady state simulations just behind the expansion. The multiphase results show the best agreement with the experiments from Karino and Goldsmith (1977) and the computations from Jung and Hassanein (2008). It is concluded that the multiphase non-Newtonian model should be used for blood flows where recirculation is present.

11.4 Healthy carotid artery

The carotid artery is a main artery of the vascular system and the blood flow through this artery is characterized by $Re > 98$ and $\overline{Re}$ equals 295. It is observed in the steady state simulations for both Re that the difference between the flow pattern and WSS, obtained with the three models, is very small. Modelling a Newtonian single-phase flow provides sufficient accuracy when only a steady state simulation of a healthy main artery is required.

11.5 Diseased carotid artery

A more realistic case for the medical usage of CFD modelling is a severely diseased carotid artery with several obstructions. A few secondary motions are observed in the steady state simulations with $Re = 120$. This is the smallest Re for this artery and no backflow is observed. All three blood models are implemented. The vorticity causes a small difference in WSS between the Newtonian flow and the non-Newtonian flows. The multiphase approach does not lead to different results than the non-Newtonian single-phase model. So the conclusion for the healthy carotid artery is preserved for the heavily diseased carotid artery.

Righolt (2010) observed some reverse flows in a transient Newtonian flow through the same diseased artery. When those observations are combined with the conclusions drawn in the present research, it is expected that the multi-phase non-Newtonian model is required when a transient flow through a diseased carotid artery has to be modelled for medical purpose.

CHAPTER 12

Recommendations

12.1 Blood model

The main properties of plasma and RBCs are implemented in the current multiphase Carreau-Yasuda model, like RBC agglomeration at low strain rates and the drag force as interaction force. An addition to the viscosity model is known that accounts for the rigid structures that are formed by the RBCs at very low strain rate ($\dot{\gamma} < 6$) which leads to an even larger viscosity (Jung and Hassanein, 2008). Secondly they propose to encounter for the increased drag that is experienced by RBC agglomerations by implementing the shape factor into the Schiller-Naumann drag model for $\dot{\gamma} < 300$. Both model extensions are entered in Appendix C.

As RBCs have a donut-like shape they tend to align with the flow. This could be implemented by adding a similar shape factor for larger strain rates. It might be possible to examine the amount of alignment with the flow and the cross-sectional area in experiments. Another method to model this alignment is to change the drag model in which could also be accounted for the flexibility of the RBCs by modelling these as liquid droplets instead of solid spheres. The analysis of Yilmaz et al. (2011) on the influence of five drag models on the flow parameters in the right CA could be used as a starting point, although reference experiments are required.

It has been proved that the Carreau-Yasuda viscosity model describes the blood viscosity well for the presented fitting parameters. This model depends on the RBC volume fraction and the strain rate. A better fit might be obtained if the influence of the amount of white blood cells or blood clotting enzymes is also caught in the fitting parameters.
Another approach of designing a viscosity model could be to look at the biological properties at cell level and create a bottom-up viscosity model. This requires a thorough study of the chemical and biological processes at micrometer scale in combination with a study of the ratios of the involved forces to be able to appoint the main forces.

One last general remark on the presented models is that the gravity and the lift force were not taken into account in the carotid arteries. It is not clear from literature whether or not the lift force should be included since its effect is observed to be significant in some simulations and negligible in others. The significance of gravity strongly depends on the orientation and the geometry of the artery. It is observed to influence the RBC distribution and the secondary motions in the 180° bended tube, which were less pronounced when the gravity was not activated in the CFD model.

12.2 Transient flow

It is concluded in this research that the multiphase approach is required for flows where recirculation is present. Recirculation could be induced by deceleration of the inlet velocity, which leads to the recommendation to perform a transient simulation with a realistic heart-pulse as inlet velocity of a diseased artery. The time-averaged flow properties will provide more realistic information than a steady state simulation using the mean values for all variables.

Since the arterial geometry and the exact heart-pulse are patient-specific it would result in the most realistic results. The heart-pulse of the patient could be measured and the direction and the shape of the inlet velocity profile should

be calibrated to the upstream arteries. Due to the larger computational costs of a transient simulation compared to a steady state simulation, one has to consider which simulation is suitable to obtain the required results.

12.3 Blood-vessel interaction

The interaction between the blood and the vessel is modelled as a no-slip velocity at the wall and the vessel is assumed to be rigid. These assumptions are required to be able to focus on the blood models, but more realistic boundary conditions are known from biological and chemical research. A mechanism that influences the interaction between the blood and the vessel is the electrical field that is present to regulate the mass transport through the vessel wall. This influences the distribution and the residence time of the RBCs.

The elastic vessel walls are stretched and contracted due to the pressure waves caused by the heart. The quantity of the vessel motions depends on the size of the vessel and its proximity to the heart. These motions should be taking into account via fluid structure interaction (FSI) when the research topic is a part of the vascular system near the heart. FSI is expected to influence the flow patterns, the RBC distribution and the particle-wall interaction and it is the current research topic of a colleague MSc student.

A third improvement regarding the vessel model is the implementation of mass transport through the vessel. The transport of Low-Density Lipoprotein (LDL), the protein that could induce blocking of the blood vessel, is examined by de Loor (2011) whose work is extended by another MSc student. The properties of the layers of the vessel are to be understood and the most important of these properties are selected to implement into a mass transport model. Different properties of those layers could provide more information on the interaction of RBCs and plasma with the wall, which will improve the model without modelling all tissue layers of the vessel.

12.4 Meshing

The type of boundary layers that is used in this study is not very common in literature. A more regular approach is to use a hexahedral boundary layer with a tetrahedral or polyhedral core. The advantage of this hybrid mesh is the regular direction of the faces of the hexahedrals while the small computational time for tetrahedrals and polyhedrals is preserved. Secondly, fewer cells are required in the boundary layer since the base could be larger than for tetrahedrals as long as the height (perpendicular to the wall) is small. It is concluded from the hexahedral meshing procedure of the bifurcating carotid arteries that one has to be aware of the difficulty to avoid highly skewed cells at the bifurcation. Therefore the boundary layer and the transition to the other cell type should be checked very thoroughly in the bifurcation.

When a final mesh type is chosen, a mesh independence analysis should be performed to quantify the smallest amount of cells that is required to obtain a mesh-independent solution. The advice could be different for healthy and diseased arteries since the obstruction could require a larger cell density to resolve all secondary flows.

Bibliography

Ansys, I. (2011*a*), 'Fluent 14.0 theory guide'.

Ansys, I. (2011*b*), 'Fluent 14.0 users guide'.

ASME (2008), 'Procedure for estimation and reporting of uncertainty due to discretization in cfd applications', *Journal of Fluids Engineering* **130**(7), 078001.

Ballyk, P., Steinman, D. and Ethier, C. (1994), 'Simulation of non-newtonian blood flow in an end-to-side anastomosis', *Rheology* **31**(5), 565–586.

Bird, R., Armstrong, R. and Hassager, O. (1987), *Dynamics of Polymer Liquids*, second edn, Wiley, New York.

de Loor, A. (2011), Towards numerical modelling of low-density lipoprotein transport through the multi-layered arterial wall, Master's thesis, Delft University of Technology, Delft.

Eça, L. and Hoekstra, M. (2009), 'Evaluation of numerical error estimation based on grid refinement studies with the method of the manufactured solutions', *Computers and Fluids* **38**(8), 1580 – 1591.

Fluent, I. (2002), 'Gambit 2.4.6 users guide'.

Gijsen, F., Allanic, E., van de Vosse, F. and Janssen, J. (1999), 'The influence of the non-newtonian properties of blood on the flow in large arteries: unsteady flow in a 90 degrees curved tube.', *Journal of Biomechanics* **32(7)**, 705–713.

Gijssen, F. (2010), 'Patient-specific carotid bifurcation. erasmus medical center'.

Groen, H. C., Simons, L., van den Bouwhuijsen, Q. J., Bosboom, E. M. H., Gijsen, F. J., van der Giessen, A. G., van de Vosse, F. N., Hofman, A., van der Steen, A. F., Witteman, J. C., van der Lugt, A. and Wentzel, J. J. (2010), 'Mri-based quantification of outflow boundary conditions for computational fluid dynamics of stenosed human carotid arteries', *Journal of Biomechanics* **43**(12), 2332 – 2338.

Holdsworth, D. W., Norley, C. J. D., Frayne, R., Steinman, D. A. and Rutt, B. K. (1999), 'Characterization of common carotid artery blood-flow waveforms in normal human subjects', *Physiological Measurement* **20**, 219–240.

Johnston, B. M., Johnston, P. R., Corney, S. and Kilpatrick, D. (2004), 'Non-newtonian blood flow in human right coronary arteries: steady state simulations', *Journal of Biomechanics* **37**(5), 709 – 720.

Johnston, B. M., Johnston, P. R., Corney, S. and Kilpatrick, D. (2006), 'Non-newtonian blood flow in human right coronary arteries: Transient simulations', *Journal of Biomechanics* **39**(6), 1116 – 1128.

Jung, J. and Hassanein, A. (2008), 'Three-phase cfd analytical modeling of blood flow', *Medical Engineering and Physics* **30**(1), 91–103.

Jung, J., Lyczkowiski, R., Panchal, C. and Hassanein, A. (2006), 'Multiphase hemodynamic simulation of pulsatile flow in a coronary artery', *Journal of Biomechanics* **39**, 2064–2073.

Karino, T. and Goldsmith, H. L. (1977), 'Flow behaviour of blood cells and rigid spheres in an annular vortex.', *Philosophical transactions of the Royal Society of London.Series B: Biological sciences* **279**(967), 413–445.

Kim, Y., P.J., V. and Lee, J. (2008), 'Multiphase non-newtonian effects on pulsatile hemodynamics in a coronary artery', *International journal for numerical methods in fluids* **58**, 803–825.

Liu, B. and Dalin, T. (2011), 'Influence of non-newtonian properties of blood on the wall shear stress in human atherosclerotic right coronary arteries', *MCB Molecular and Cellular Biomechanics* **8**(1), 73–90.

Liu, Y., Pekkan, K., Jones, S. C. and Yoganatha, A. P. (2004), 'The effects of different mesh generation methods on computational fluid dynamic analysis and power loss assessment in total cavopulmonary connection', *Journal of Biomechanical Engineering* **126**, 594–603.

Longest, P. W. and Vinchurkar, S. (2007), 'Effects of mesh style and grid convergence on particle deposition in bifurcating airway models with comparisons to experimental data', *Medical Engineering and Physics* **29**(3), 350 – 366.

Macagno, E. and Hung, T.-K. (1967), 'Computational and experimental study of a captive annular eddy', *Journal of Fluid Mechanics* **28**(1), 43–64.

Quemada, D. (1978*a*), 'Rheology of concentrated disperse systems ii. a model for non-newtonian shear viscosity in steady flows', *Rheologica Acta* **17**(6), 632–642.

Quemada, D. (1978*b*), 'Rheology of concentrated disperse systems iii. general features of the proposed non-newtonian model. comparison with experimental data', *Rheologica Acta* **17**(6), 643–653.

Righolt, B. (2010), Numerical simulations of magnetic drug targeting in realistic arterial bifurcations, Master's thesis, Delft University of Technology, Delft.

Roache, P. J. (1994), 'Perspective: A method for uniform reporting of grid refinement studies', *Journal of Fluids Engineering* **116**, 405–413.

Roache, P. J. (1998), *Verification and Validation in Computational Science and Engineering*, Hermosa Publishers, New Mexico.

Roy, C. J. (2010), 'Review of discretization error estimators in scientific computing', *AIAA Paper-2010-0126* (48th AIAA Aerospace Sciences Meeting, January 4-7, Orlando, FL).

Schiller, L. and Naumann, Z. (1935), 'A drag coefficient correlation', *Z. Ver. Deutsch. Ing.* **77**, 318.

Soulis, J. V., Giannoglou, G. D., Chatzizisis, Y. S., Seralidou, K. V., Parcharidis, G. E. and Louridas, G. E. (2008), 'Non-newtonian models for molecular viscosity and wall shear stress in a 3d reconstructed human left coronary artery', *Medical Engineering and Physics* **30**(1), 9 – 19.

Spiegel, M., Redel, T., Zhang, Y., Struffert, T., Hornegger, J., Grossman, R. G., Doerfler, A. and Karmonik, C. (2011), 'Tetrahedral vs. polyhedral mesh size evaluation on flow velocity and wall shear stress for cerebral hemodynamic simulation', *Computer Methods in Biomechanics and Biomedical Engineering* **14**, 9–22.

Wojnarowski, J. (2001), Numerical study of bileaf heart valves performance., *in* 'International Scientific Practical Conference: Efficiency of Engineering Education in XX Century', Donetsk Ukraine.

Yilmaz, F. and Gundogdu, Y. (2008), 'A critical review on blood flow in large arteries; relevance to blood rheology, viscosity models, and physiologic conditions', *Rheology Journal* **20**(4), 197–211.

Yilmaz, F., Kutlar, A. and Gundogdu, M. (2011), 'Analysis of drag effects on pulsatile blood flow in a right coronary artery by using eulerian multiphase model', *Korea-Australia Rheology Journal* **23**, 89–103.

Zou, L., Larsson, L. and Orych, M. (2010), 'Verification and validation of cfd predictions for a manoeuvring tanker', *Journal of Hydrodynamics* **22(5)**, 438–445.

Acknowledgments

It has been a pleasure to do my MSc project at the section of Transport Phenomena under the supervision of Saša Kenjereš. His never declining enthusiasm encouraged me to keep thinking out of the box and to continuously look for new challenges. He was always available and for questions and discussions. My predecessors Bernhard and Alexander helped me to have a smooth start with meshing and using Fluent. Later on Farzad, Bernhard, Koen and their colleague PhDs helped me by discussing the problems I encountered with simulating, visualizing or Linux. I would also like to thank the students and PhDs who were also supervised by Saša for the discussions and questions during our progress meetings.
The daily coffee-breaks in the sun at the Leeghwaterstraat or next to the fishbowl in the Waterzaal really helped to reset my mind to be able to focus again afterward. Total nonsense and really interesting discussions alternated quickly during these breaks thanks to all students and PhDs.
I am very grateful for the loving support of my boyfriend Gerrit who helped with triggering questions and continuous support in the hard times of my project.
Last but not least I want to thank my parents and my sisters, for all their support.

Heleen Doolaard
Februari 2013

Appendix A

Derivation observed order

Mesh refinement is a well known method to quantify the accuracy of a CFD simulation. The prediction of the exact solution based on mesh refinement should contain an error or uncertainty band that contains the exact solution for 90% sure. Giving this uncertainty band is not straightforward, especially when there are no experimental results to compare to. Roache (1998) developed a method to calculate an error band for the solution acquired at the finest mesh. For this error band the observed order has to be calculated first. The observed order is the order of the discretization scheme that can be derived from the results of simulations using two or three systematically refined meshes, where systematic refinement means that a uniform refinement factor is used for the whole grid.
Our starting point for deriving an implicit equation for the observed order of accuracy is Equations 4.32 and 4.33:

$$f_h = \tilde{f} + g_p h^p + g_{p+1} h^{p+1} + g_{p+2} h^{p+2} + \cdots \quad (A.1)$$
$$f_{rh} = \tilde{f} + g_p (rh)^p + g_{p+1} (rh)^{p+1} + g_{p+2} (rh)^{p+2} + \cdots \quad (A.2)$$

f_h and f_{rh} are the values of variable f on the fine mesh with average spacing h and a coarser mesh with average spacing $r \cdot h$ where r is defined as $\frac{h_{coarse}}{h_{fine}}$. Assume there are three meshes, mesh 1, 2 and 3 which are fine, middle and coarse respectively. The refinement factors that are used to obtain mesh 3 from mesh 2 and mesh 1 from mesh 2 are r_{23} and r_{12}. Substituting these variables into Equations A.1 and A.2 gives

$$f_1 = \tilde{f} + g_p h^p + g_{p+1} h^{p+1} + g_{p+2} h^{p+2} + \cdots \quad (A.3)$$
$$f_2 = \tilde{f} + g_p (r_{12} h)^p + g_{p+1} (r_{12} h)^{p+1} + g_{p+2} (r_{12} h)^{p+2} + \cdots \quad (A.4)$$
$$f_3 = \tilde{f} + g_p (r_{12} r_{23} h)^p + g_{p+1} (r_{12} r_{23} h)^{p+1} + g_{p+2} (r_{12} r_{23} h)^{p+2} + \cdots \quad (A.5)$$

Neglecting the terms of order h^{p+1} and higher results in

$$f_1 = \tilde{f} + g_p h^p \quad (A.6)$$
$$f_2 = \tilde{f} + g_p (r_{12} h)^p \quad (A.7)$$
$$f_3 = \tilde{f} + g_p (r_{12} r_{23} h)^p \quad (A.8)$$

Next we subtract f_2 from f_3 and f_1 from f_2 and take the quotient of these equations. Then we rearrange the equation and obtain a recursive expression for the observed order $\hat{p}$.

$$f_3 - f_2 = g_p (r_{12} h)^{\hat{p}} \left(r_{23}^{\hat{p}} - 1 \right) \quad (A.9)$$
$$f_2 - f_1 = g_p h^{\hat{p}} \left(r_{12}^{\hat{p}} - 1 \right) \quad (A.10)$$
$$\frac{f_3 - f_2}{f_2 - f_1} = \frac{r_{12}^{\hat{p}} \left(r_{23}^{\hat{p}} - 1 \right)}{r_{12}^{\hat{p}} - 1} \quad (A.11)$$
$$\left(r_{12}^{\hat{p}} - 1 \right) \frac{f_3 - f_2}{f_2 - f_1} = (r_{12} r_{23})^{\hat{p}} - r_{12}^{\hat{p}} \quad (A.12)$$
$$(r_{12} r_{23})^{\hat{p}} = \left(r_{12}^{\hat{p}} - 1 \right) \frac{f_3 - f_2}{f_2 - f_1} + r_{12}^{\hat{p}} \quad (A.13)$$
$$\hat{p} = \frac{\ln \left[\left(r_{12}^{\hat{p}^k} - 1 \right) \left(\frac{f_3 - f_2}{f_2 - f_1} \right) + r_{12}^{\hat{p}^k} \right]}{\ln (r_{12} r_{23})} \quad (A.14)$$

Equation A.14 equals Equation 4.41.

Appendix B

User defined functions

B.1 Carreau-Yasuda viscosity

```
/************************************************************/
/*                                                          */
/* User-Defined Function for spcifying blood viscosity      */
/*  for multiphase flow                                     */
/*                                                          */
/* Fluent 14                                                */
/*                                                          */
/* Author: Heleen Doolaard                                  */
/*   Date: August 2012                                      */
/*                                                          */
/* This function sets the property of (laminar) viscosity of */
/* two-phase Eulerian-Eulerian flow, using the model        */
/* developed by Carreau and Yasuda (see Jung 2006,          */
/* Journ of Biomech 39, 2064-2073)                          */
/*                                                          */
/************************************************************/


#include "udf.h"
DEFINE_PROPERTY(granular_viscosity_rbc, cell, thread_rbc)
{
int phase_domain_index, ID=2;
Thread *mixthread;
Thread *subthread;
Domain *mixture_domain;
mixture_domain = Get_Domain(1);
mixthread = Lookup_Thread(mixture_domain,ID);

/* predefine variables */
real muplasma=0.006, murbc=0.01, mumix=0.0037, eps_rbc=0.45, lambda=0.110,  m=9.106, n=0.749,
    sr=500;
Domain *plasma_domain;
Domain *rbc_domain;

/* get domain numbers of plasma and rbc */
plasma_domain = Get_Domain(2);
rbc_domain = Get_Domain(3);

/* loop over all threads */
sub_thread_loop(subthread, mixthread, phase_domain_index)
{
/* viscosity in plasma thread is muplasma */
        if ( subthread == Lookup_Thread(plasma_domain,ID) )
                {
                muplasma = C_MU_L(cell, subthread);
                }
        else if ( subthread == Lookup_Thread(rbc_domain,ID) )
                {
                sr = C_STRAIN_RATE_MAG(cell,subthread); /* shear rate from rbc, could be the
                    wrong one */
                eps_rbc = C_VOF(cell, subthread);
                }
```

```
}
n = 0.8092*pow(eps_rbc,3.) - 0.8246*pow(eps_rbc,2.) - 0.3503*eps_rbc + 1.;
m = 122.28*pow(eps_rbc,3.) - 51.213*pow(eps_rbc,2.) + 16.305*eps_rbc + 1.;
mumix = m* pow( (1.+ pow((lambda*sr),2.) ),((n-1.)/2.) );
murbc = (mumix*muplasma-(1.-eps_rbc)*muplasma)/eps_rbc;

/*if (cell %50000==0)
{
Message("muplasma = %f\n", muplasma);
Message("strainrate = %f\n",sr);
Message("vof = %f\n",eps_rbc);
Message("n = %f\n",n);
Message("m = %f\n",m);
Message("mumix %f\n",mumix);
Message("murbc %f\n",murbc);
Message(" %f\n",);
}*/

return murbc;

}
```

B.2 Transient inlet velocity

```
/************************************************************/
/*                                                          */
/* Fluent 14                                                */
/*                                                          */
/* Author: Heleen Doolaard                                  */
/*   Date: August 2012                                      */
/*                                                          */
/* This function prescribes an oscillating uniform velocity */
/* at the u-shaped pipe inlet by defining the inlet velocity */
/* magnitude based on the fit of the velocity profile of    */
/* Jung et al, Journal of biomechanics, 2006, 39:2064-2073  */
/* Multiphase hemodynamic simulation of pulsatile flow in a */
/* coronary artery                                          */
/*                                                          */
/************************************************************/


#include "udf.h"

/* jung_inlet_fluent.txt contains the fitting of the velocity magnitude of Jung's paper,
    fitted
in parts by polynomials
column 1: starting time normalized by blood cycle period ; column 2: normalized ending time;
    column 3: coeff in front of t^3; column 4: coeff in front of t^2;
column 5: coeff in front of t; column 6: scalar.
Each row contains 7 elements that represent the 7 parts of the curve */

DEFINE_PROFILE(inlet_velocity_transient, thread, position)
{
/*      FILE *ftp; */

        face_t f;
        float time, t;
        t = RP_Get_Real("flow-time");
        /* real t=CURRENT_TIME; */
        real mult;              /* Multiplier for the transient part */
        real p=0.73;    /* Period of the blood cycle [s] */
        /*real v_mean=RP_Get_Real("inletvmean");*/      /* Mean velocity [m/s] */
        /*real radius=0.002185;  Radius of the inlet cylinder [m] */
        real x0[ND_ND]; /* Position of the center of the inlet [m] */
        x0[0]=0.041515;
        x0[1]=-0.02;
```

```
        x0[2]=0.;
        real xf[ND_ND]; /*rr[ND_ND];      Position of the face center [m] and relative to inlet
             center [m] */

        begin_f_loop(f, thread)
        {
        F_CENTROID(xf, f, thread);

/*periodicity for 15 cardiac cycles */
t1me = 1.0*t;
if (t1me >= p) /*2nd cardiac cycle */
{t1me = t1me - p;}
if (t1me >= p)  /*3rd cardiac cycle */
{t1me = t1me -p;}
if (t1me >= p)  /*4th cardiac cycle */
{t1me = t1me -p;}
if (t1me >= p)  /*5th cardiac cycle */
{t1me = t1me -p;}
if (t1me >= p)
{t1me = t1me -p;}
if (t1me >= p)
{t1me = t1me -p;}
if (t1me >= p)
{t1me = t1me -p;}
if (t1me >= p)
{t1me = t1me -p;}
if (t1me >= p)
{t1me = t1me -p;}
if (t1me >= p)
{t1me = t1me -p;}
if (t1me >= p)
{t1me = t1me -p;}
if (t1me >= p)
{t1me = t1me -p;}
if (t1me >= p)
{t1me = t1me -p;}
if (t1me >= p)
{t1me = t1me -p;} /*15th cardiac cycle */

        /* Determine time dependent part. */
        if (t1me < (6.7000000e-02*p) )
                {
                mult = 0*pow((t1me/p),3.)+0*pow((t1me/p),2.)-7.6340357e-02*(t1me/p)+1.3128147e
                    -01;
                }
        else
        {
                if ( (t1me>= (6.7000000e-02*p)) && (t1me < (1.0800000e-01*p )) )
                {
                mult = 0*pow((t1me/p),3.)+0*pow((t1me/p),2.)+3.8004205e+00*(t1me/p)-1.3391589e
                    -01;
                }
                else
                {
                        if ( (t1me>=(1.0800000e-01*p)) && (t1me < (2.9800000e-01*p)) )
                        {
                        mult = 4.0935257e+01*pow((t1me/p),3.)-3.1848449e+01*pow((t1me/p),2.)
                            +7.6989005e+00*(t1me/p)-2.3405134e-01;
                        }
                        else
                        {
                                if ( (t1me>=(2.9800000e-01*p)) && (t1me < (3.9000000e-01*p)) )
                                {
                                mult = 0*pow((t1me/p),3.)+0*pow((t1me/p),2.)-5.8224594e-01*(
                                    t1me/p)+4.8892945e-01;
                                }
                                else
```

```
                                {
                                        if( (t1me>=(3.9000000e-01*p)) && (t1me < (4.6600000e
                                            -01*p)) )
                                        {
                                        mult = 0*pow((t1me/p),3.)+0*pow((t1me/p),2.)-1.7000532
                                            e+00*(t1me/p)+9.2599204e-01;
                                        }
                                        else
                                        {
                                                if ( (t1me>=(4.6600000e-01*p)) &&(t1me <
                                                    (5.0200000e-01*p)) )
                                                {
                                                mult = 0*pow((t1me/p),3.)+0*pow((t1me/p),2.)
                                                    +3.7897451e+00*(t1me/p)-1.6329280e+00;
                                                }
                                                else
                                                {
                                                mult = 0*pow((t1me/p),3.)+3.6454919e-01*pow((
                                                    t1me/p),2.)-8.2778142e-01*(t1me/p)
                                                    +5.9524173e-01;
                                                }

                                        }

                                }

                        }

                }

        }

        F_PROFILE(f, thread, position) = mult ;
    /* 20 sept: add print output */
/*        if ( (f %1==0) && (f<11) )
        {Message("input face %d = %f \n",f,mult); }
        if (f == 10)
        {Message("time = %f \n",t1me);}       */
        }
        end_f_loop(f, thread)
        }
```

B.3 Density

```
/*****************************************************************/
/*                                                               */
/* User-Defined Function for spcifying rbc density as            */
/*  function of volume fraction                                  */
/*                                                               */
/* Fluent 14                                                     */
/*                                                               */
/* Author: Heleen Doolaard                                       */
/*   Date: August 2012                                           */
/*                                                               */
/* This function sets the property of (laminar) viscosity of     */
/* two-phase Eulerian-Eulerian flow, using the model             */
/* developed by Carreau and Yasuda (see Jung 2006,               */
/* Journ of Biomech 39, 2064-2073)                               */
/*                                                               */
/*****************************************************************/


#include "udf.h"
DEFINE_PROPERTY(density_rbc,cell,thread)
{
int phase_domain_index, ID=2;
```

```
Thread *mixthread;
Thread *subthread;
Domain *mixture_domain;
mixture_domain = Get_Domain(1);
mixthread = Lookup_Thread(mixture_domain,ID);

/* predefine variables */
real rhoplasma=10., rhorbc=10., vof=0.45, rhomix=1080;
Domain *plasma_domain;
Domain *rbc_domain;

/* get domain numbers of plasma and rbc */
plasma_domain = Get_Domain(2);
rbc_domain = Get_Domain(3);

/* loop over all threads */
sub_thread_loop(subthread, mixthread, phase_domain_index)
{
/* density in plasma thread is rhoplasma */
        if ( subthread == Lookup_Thread(plasma_domain,ID) )
                {
                rhoplasma = C_R(cell, subthread);
                }
/* volume fraction in rbc thread is retreived */
        else if ( subthread == Lookup_Thread(rbc_domain,ID) )
                {
                vof = C_VOF(cell, subthread);
                }
/* rho_mixture = volume fraction_rbc * rho_rbc + volume fraction_plasma * rho_plasma */
rhorbc = (rhomix-(rhoplasma*(1-vof)))/(vof+1e-4); /* avoids error for vof=0 */

}
return rhorbc;
}
```